



**UNIVERSITÀ DEGLI STUDI DI TRIESTE**

**CNR-INFM LABORATORIO NAZIONALE TASC**

Posto di dottorato attivato grazie al contributo di: Bracco Imaging

**XIX CICLO DEL  
DOTTORATO DI RICERCA IN  
NANOTECNOLOGIE**

**OPTICAL TWEEZERS FOR THE STUDY OF  
MICROBUBBLE DYNAMICS IN ULTRASOUND**

Settore disciplinare: FIS/07

DOTTORANDA  
Valeria Garbin

COORDINATORE DEL COLLEGIO DEI DOCENTI  
Chiar.mo Prof. Fernando Tommasini  
Università degli Studi di Trieste

RELATORE  
Chiar.mo Prof. Enzo Di Fabrizio  
Università 'Magna Græcia' di Catanzaro

CORRELATORE  
Dr. Dan Cojoc  
CNR-INFM Laboratorio Nazionale TASC

CORRELATORE  
Dr. Michel Versluis  
University of Twente



# Abstract

Optical tweezers enable for non-destructive, contact-free manipulation of ultrasound contrast agent (UCA) microbubbles, which are used in medical imaging for enhancing the echogenicity of the blood pool and to quantify organ perfusion.

Understanding the dynamics of ultrasound-driven contrast agent microbubbles from a fundamental physical standpoint is a first step for exploiting their acoustical properties and to develop new diagnostic and therapeutic applications. However, experiments on bubble dynamics presently suffer from a lack of control on bubble position, because of buoyancy, microstreaming and bubble clustering. In this respect, optical tweezers can be used to study UCA microbubbles under controlled and repeatable conditions, by positioning them away from interfaces and from neighboring bubbles. In addition, an ultra-high speed imaging system is required to record the dynamics of UCA microbubbles in ultrasound, as their oscillations occur on the nanoseconds timescale.

In this thesis, optical tweezers and an ultra-high speed camera are integrated into an experimental setup to control the boundary conditions and record the oscillations of the microbubbles. Optical tweezers are commonly obtained by focusing a laser beam through a microscope objective, as the high intensity gradient in the focal region causes dielectric microparticles to be attracted in the focus. In the special case of microbubbles, which exhibit a lower refractive index than the surrounding liquid, the opposite situation arises: they are pushed away from the region of maximum intensity. Nevertheless, microbubbles can be trapped in the dark core of a donut-shaped trap, which can be obtained e.g. by focusing a Laguerre-Gaussian beam. In our setup, a Gaussian beam is converted to a Laguerre-Gaussian mode by using diffractive optical elements implemented on a spatial light modulator. This allows to trap and manipulate single or multiple microbubbles, and to control the distance from interfaces as well as the bubble-to-bubble distance. The “Brandaris 128” ultra-high speed camera is used, in combination with the optical tweezers, to recorded the bubble oscillations at a frame rate of 15 million frames per second.

The influence of a rigid wall on the resonance frequency and oscillation amplitude was experimentally investigated. An experimental phospholipid-coated agent (BR-14, Bracco Research S.A., Geneva, Switzerland) was used throughout the experiments. A resonance frequency curve was recorded for the same bubble positioned at the wall and at controlled distance from the wall. The experiments show a drop in the resonance frequency for the bubble close to the

wall, as expected from the theoretical models. These results are highly relevant for molecular imaging applications, where the response of targeted microbubbles needs to be discriminated from that of freely flowing ones. We also quantify the bubble-to-bubble interaction, in two ways: first, we compare the change of the radial oscillations of one bubble with and without a neighboring bubble. Second, we resolve the change in distance between two bubbles during ultrasonic insonation. This results from an acoustical, generally attractive, interaction force between the bubbles, termed secondary Bjerknes force. To understand this rich two-bubble dynamics, we couple a recent single-bubble model, accounting for both gas and monolayer properties with a model quantifying the mutual interaction of bubbles in their translation and oscillations.

Experiments where optical tweezers are used as a force sensor to measure the binding force in an antigen-antibody complex at the single molecule level are also presented. In the future, the possibility of combining optical micromanipulation with the force-sensing capabilities of optical tweezers will open the way to a new class of experiments which will give us a deeper insight into fundamental bubble phenomena and find direct application to new ultrasound-assisted targeting strategies.

# Contents

<b>Abstract</b>	<b>iii</b>
<b>1 Introduction</b>	<b>1</b>
Bibliography . . . . .	4
<b>2 Optical tweezers</b>	<b>7</b>
2.1 Optical tweezers . . . . .	8
2.1.1 Introduction . . . . .	8
2.1.2 The mechanism of optical trapping . . . . .	9
2.1.3 Multiple tweezers . . . . .	9
2.1.4 Manipulation with singular beams . . . . .	10
2.1.5 Optical tweezers as a force transducer . . . . .	12
2.2 Radiation trapping forces . . . . .	12
2.2.1 Introduction . . . . .	12
2.2.2 Radiation forces on spherical particles in arbitrary fields . .	13
2.2.3 Ray-optics approximation . . . . .	14
2.2.4 Point-dipole approximation . . . . .	16
2.2.5 Additional forces in optical tweezers . . . . .	16
Bibliography . . . . .	18
<b>3 Laser Beam Shaping for Optical Tweezers</b>	<b>23</b>
3.1 Introduction . . . . .	24
3.1.1 Implementation of diffractive optical elements for optical tweezers . . . . .	25
3.2 Computer-generated diffractive optical elements . . . . .	26
3.2.1 Phase retrieval using iterative algorithms (PRIA) . . . . .	27
3.2.2 Spherical waves propagation and superposition . . . . .	28
3.3 Laguerre-Gaussian beams for optical tweezers . . . . .	29
3.3.1 Introduction . . . . .	29
3.3.2 Properties of Laguerre-Gaussian beams . . . . .	30
3.3.3 Laguerre-Gaussian beam converters . . . . .	32
3.3.4 Multiple helical beams . . . . .	34
3.3.5 3D position of a vortex trap . . . . .	37
3.4 Conclusions . . . . .	39
Bibliography . . . . .	39

<b>4</b>	<b>Low-index particles trapping using Laguerre-Gaussian beams</b>	<b>41</b>
4.1	Introduction . . . . .	42
4.1.1	Optical trapping of low-index particles . . . . .	42
4.1.2	Optical trapping of UCA microbubbles . . . . .	43
4.2	Materials and Methods . . . . .	43
4.2.1	Optical setup . . . . .	43
4.2.2	Sample preparation . . . . .	45
4.2.3	Forces balance on UCA microbubbles . . . . .	45
4.3	Results . . . . .	46
4.3.1	Three-dimensional trapping . . . . .	46
4.3.2	Multi-trapping of microbubbles . . . . .	47
4.4	Conclusions . . . . .	51
	Bibliography . . . . .	51
<b>5</b>	<b>Micromanipulation and imaging of UCA microbubbles</b>	<b>53</b>
5.1	Introduction . . . . .	54
5.2	Methods and apparatus . . . . .	55
5.2.1	Optical tweezers setup . . . . .	55
5.2.2	The “Brandaris 128” camera . . . . .	55
5.2.3	Ultrasound setup . . . . .	57
5.2.4	Combined optical trapping and ultra-high speed imaging . . . . .	58
5.3	Results . . . . .	61
5.3.1	Recordings of freely oscillating microbubbles . . . . .	61
5.3.2	Influence of the laser trap on bubble dynamics . . . . .	61
5.4	Conclusions . . . . .	62
	Bibliography . . . . .	65
<b>6</b>	<b>Bubble-wall and bubble-bubble interactions</b>	<b>67</b>
6.1	Introduction . . . . .	68
6.1.1	UCA microbubbles . . . . .	68
6.1.2	Interaction of UCA microbubbles with ultrasound . . . . .	69
6.1.3	Experimental characterization of UCA microbubble dynamics . . . . .	69
6.2	Theory . . . . .	70
6.2.1	Radial dynamics of a free gas bubble . . . . .	70
6.2.2	Sound radiation . . . . .	71
6.2.3	The microbubble as a forced linear oscillator . . . . .	71
6.2.4	Resonance frequency . . . . .	72
6.2.5	Dynamics of a bubble near a rigid wall . . . . .	72
6.2.6	Acoustic radiation pressure . . . . .	74
6.2.7	Dynamics of a bubble pair . . . . .	74
6.2.8	Dynamics of a coated bubble . . . . .	75
6.3	Experimental results . . . . .	77
6.3.1	Amplitude of oscillations near a boundary . . . . .	77
6.3.2	Resonance frequency shift . . . . .	81
6.3.3	Secondary Bjerknes force . . . . .	84

---

6.4	Conclusions . . . . .	86
	Bibliography . . . . .	87
<b>7</b>	<b>Force spectroscopy of antigen-antibody complexes</b>	<b>91</b>
7.1	Introduction . . . . .	92
	7.1.1 Characterization of individual intermolecular bonds . . . . .	92
	7.1.2 Rupture force probability distribution . . . . .	92
7.2	Methods . . . . .	93
	7.2.1 Optical-trap force sensor . . . . .	93
	7.2.2 Force measurements . . . . .	94
	7.2.3 Position calibration . . . . .	95
	7.2.4 Stiffness calibration . . . . .	95
7.3	Materials and apparatus . . . . .	96
	7.3.1 Fluorescein-anti fluorescein assay . . . . .	96
	7.3.2 Optical setup . . . . .	99
7.4	Results and data analysis . . . . .	101
7.5	Conclusions . . . . .	103
	Bibliography . . . . .	103
<b>8</b>	<b>Conclusions</b>	<b>105</b>
<b>A</b>	<b>Interaction of the electromagnetic field with objects</b>	<b>109</b>
	Bibliography . . . . .	112
	<b>List of Figures</b>	<b>113</b>
	<b>List of Tables</b>	<b>115</b>
	<b>Abbreviations</b>	<b>116</b>
	<b>Publications and Communications</b>	<b>118</b>





# Chapter 1

## Introduction

Since their advent in 1986 [1], optical tweezers have found many useful and intriguing applications, ranging from physics to biology. Nowadays, several optical tweezers-based techniques have been developed to perform experiments on micro- and nano-scale systems with well-controlled experimental conditions. In particular, the ability to exert piconewton forces on micron-sized particles is now routinely applied to fields as diverse as the physics of colloids [2], the study of biomolecular complexes at the single-molecule level [3] or the measurement of cellular mechanical properties.

It was already recognized in the early studies of Ashkin that optical trapping of low-refractive index particles would present a separate challenge, as they are repelled from a conventional optical trap, consisting of a tightly focused laser beam with a Gaussian intensity profile. Three-dimensional optical trapping of low-index particles in the dark core of a focused optical vortex beam was first demonstrated in 1996 by Gahagan *et al.* [4]. This finding had not been fully exploited until recently, by applying it to the study of a low-index particles system.

In the past three years several groups demonstrated trapping of ultrasound contrast agent (UCA) microbubbles [5, 6, 7]. These are micron-sized gas bubbles, and therefore low-index particles, which are commonly used to enhance the contrast in ultrasound medical imaging. Their acoustical response signature in ultrasound allows discriminating the blood pool from the surrounding tissues, with important applications to diagnostic imaging. A problem common to all experiments on UCA microbubbles has been the lack of control on the position and distance from interfaces and neighboring bubbles, due to buoyancy, flow, bubble clustering and sticking. Optical tweezers provided an elegant solution for studying UCA microbubble behavior in ultrasound with controlled boundary conditions. Micromanipulation and positioning of UCAs were successfully applied to the study of cell sonoporation induced by violently collapsing microbubbles [8] and of boundary-dependent bubble response to ultrasound [9].

Many aspects of the dynamics of microbubbles in ultrasound remain elusive, as non-linear oscillations, complex surface modes, cavitation phenomena and mutual interactions between bubbles occur [10]. Microbubble dynamics in ultrasound under microscopic flow conditions is a field of active research, not only

for to the potential applications of microbubbles in ultrasound diagnostic imaging but also from a fundamental physical standpoint. A quantitative study of the forces acting on these bubbles is hampered by buoyancy and by the difficulty of controlling the position of bubbles and repeating experiments on the same bubble. The use of optical tweezers in this research area opens the way to a new class of experiments, where the position and boundary conditions of individual microbubbles can be precisely controlled and their dynamics can be studied under prescribed, repeatable experimental conditions. A deeper understanding of bubble phenomena may eventually find direct applications in diagnostic ultrasound, allowing to further develop bubble technology on one hand, and to improve the imaging protocols on the other hand.

In recent years, targeted molecular imaging with ultrasound proved indeed to be a promising technique for diagnosis, and it is now rapidly developing [11]. Molecular imaging with ultrasound contrast agent microbubbles can be achieved by incorporating targeting ligands onto the bubble coating. Targeting of suitable markers expressed by cells on their membrane can provide disease-specific imaging and thus meaningful information for clinical decision making. Microbubbles can also be used as therapeutic agents for treating thrombosis and vascular plaques, and for drug and gene delivery. Combining the therapeutic capability of UCA microbubbles with the targeting offers the potential to integrate targeted therapy and diagnostic imaging in the same preparation. For molecular imaging applica-

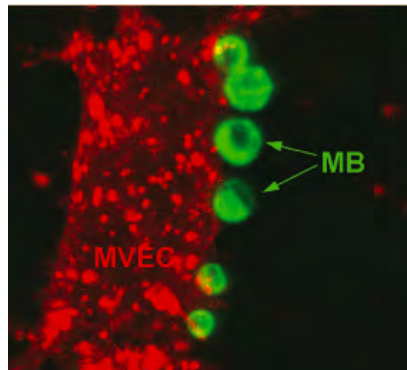


**Figure 1.1** Confocal microscopy of fluorescently labeled VCAM-1-targeted microbubbles (green) and TNF- $\alpha$ -activated labeled (red) microvascular endothelial cells. From Lankford *et al.* [12].

tions in ultrasound, it will be crucial to develop methods for selectively detecting adherent UCA microbubbles that have bound to specific molecular targets, from freely flowing ones, based on a change in their acoustic response. Considerable differences in the amplitude of oscillations, which were recently reported [13, 12], may result in a powerful technique for acoustically discriminating between bound and free bubbles. A comparison of the bubble response is therefore required for functionalized bubbles when they are adherent to their target, relative to when they are freely flowing. The use of optical tweezers for the study of microbubble

dynamics under controlled experimental conditions therefore offers also exciting possibilities for developing targeting strategies.

## Goal of this study

The goal of this investigation is to apply the optical trapping technique to the study of microbubble dynamics in ultrasound with well-controlled, repeatable experimental conditions, namely the position relative to a rigid wall and to neighboring bubbles. This involved first of all developing an optical tweezers setup for low-index particles trapping and micromanipulation. Next, the optical tweezers setup was combined to an ultra-high speed camera for time-resolved optical recordings of UCA microbubble dynamics in ultrasound. The first experiments showing how the very same bubble responds to ultrasound with different boundary conditions are then performed.

## Overview of the thesis

- **Chapter 2: Optical tweezers** reviews the historical development, the applications and the theoretical description of optical tweezers. The specific features of optical confinement of microbubbles, which are low-refractive index particles, are introduced.
- **Chapter 3: Laser beam shaping for optical tweezers** presents laser beam shaping by means of diffractive optical elements, which are used in this work for generating Laguerre-Gaussian beams for trapping low-index particles. Generation of arbitrary configurations of traps for low-index particles is demonstrated.
- **Chapter 4: Low-index particles trapping using Laguerre-Gaussian beams** presents the experimental results concerning micromanipulation of microbubbles. 3D trapping and control over the distance from interfaces is demonstrated, for individual and multiple microbubbles. The flexibility of our approach, where diffractive optical elements are implemented on a spatial light modulator, is highlighted.
- **Chapter 5: Combined optical micromanipulation and ultra-high speed imaging of UCA microbubbles** describes the development of a setup for studying microbubble dynamics with controlled boundaries. The optical tweezers setup is used in combination with the ultra-high speed camera “Brandaris 128”, at the University of Twente (The Netherlands), for time-resolved characterization of microbubble dynamics in ultrasound.
- **Chapter 6: 3D optical manipulation of microbubbles: bubble-wall and bubble-bubble interaction** shows the first results of the study of microbubbles with the setup combining optical tweezers and ultra-high speed imaging. Well-controlled boundary conditions for the microbubbles

can be set, enabling for the investigation of boundary-dependent signatures in the bubble response, which are crucial for molecular imaging applications. Quantification of acoustical and hydrodynamical forces on the microscale is also an exciting application of the technique.

- **Chapter 7: Force spectroscopy of antigen-antibody complexes** reports on the use of optical tweezers as a force sensor, in single molecule experiments for the characterization of antigen/antibody interactions. Experiments performed during a research stay at the Biological Engineering Division of MIT are presented.
- **Chapter 8: Conclusions** presents the conclusions and outlines the potential follow-up of this work.

## Bibliography

- [1] A. Ashkin, J.M. Dziedzic, J.E. Bjorkholm, and S. Chu. Observation of a single-beam gradient force optical trap for dielectric particles. *Opt. Lett.*, 11:288, 1986.
- [2] D.G. Grier. A revolution in optical manipulation. *Nature*, 424:810–816, 2003.
- [3] C. Bustamante, J.C Macosko, and J.L. Wuite. Grabbing the cat by the tail: manipulating molecules one by one. *Nature Reviews*, 1:130–136, 2000.
- [4] K.T. Gahagan and G.A. Swartzlander. Optical vortex trapping of particles. *Opt. Lett.*, 21:827, 1996.
- [5] P.A. Prentice, M.P. MacDonald, T.G. Frank, A. Cuschieri, G.C. Spalding, W. Sibbett, P.A. Campbell, K. Dholakia. Manipulation and filtration of low index particles with holographic Laguerre-Gaussian optical trap arrays. *Opt. Exp.*, 12:593–600, 2004.
- [6] V. Garbin, D. Cojoc, E. Ferrari, R.Z. Proietti, S. Cabrini, E. Di Fabrizio. Optical micromanipulation using Laguerre-Gaussian beams. *Japan. J. Appl. Phys.*, 44:5772–5775, 2005.
- [7] P.H. Jones, E. Stride and N. Saffari. Trapping and manipulation of microscopic bubbles with a scanning optical tweezer. *Appl. Phys. Lett.*, 89:081113, 2006.
- [8] P. Prentice, A. Cuschieri, K. Dholakia, M. Prausnitz, and P. Campbell. Membrane disruption by optically controlled microbubble cavitation. *Nat. Phys.*, 1:107–110, 2005.
- [9] V. Garbin, D. Cojoc, E. Ferrari, E. Di Fabrizio, M.L.J. Overvelde, S.M. van der Meer, N. de Jong, D. Lohse, M. Versluis. Changes in microbubble dynamics near a boundary revealed by combined optical micromanipulation and high speed imaging. *Appl. Phys. Lett.*, accepted for publication.

- 
- [10] N. de Jong, A. Bouakaz and P. Frinking. Basic acoustic properties of microbubbles. *Echocardiography*, 19:229–240, 2002.
  - [11] A.L. Klibanov. Microbubble contrast agents. Targeted ultrasound imaging and ultrasound-assisted drug-delivery applications. *Invest. Radiol.*, 41:354–362, 2006.
  - [12] M. Lankford, C.Z. Behm, J. Yeh, A.L. Klibanov, P. Robinson and J.R. Linder. Effect of microbubble ligation to cells on ultrasound signal enhancement. implications for targeted imaging. *Invest. Radiol.*, 41:721–728, 2006.
  - [13] S. Zhao, K.W. Ferrara and P.A. Dayton. Asymmetric oscillation of adherent targeted ultrasound contrast agents. *Appl. Phys. Lett.*, 87:134103, 2005.



## Chapter 2

# Optical tweezers

In the past two decades optical trapping gained a key role in micro- and nanosciences as it serves the scope of scaling experiments down to single micro- and nano-objects, from microscopic particles to nanoparticles, from living cells to single molecules. This chapter reviews the development of the optical tweezers technique and its applications in the field of biology and medicine. A historical background is first given in Section 2.1, and developments of the original setup enabling more advanced applications, based on laser beam shaping, are presented. In Section 2.2 the forces involved in the optical trapping phenomenon are then described from a theoretical standpoint.

## 2.1 Optical tweezers

### 2.1.1 Introduction

Optical tweezers find nowadays application in a wide range of disciplines, from physics to biology. The first observations of radiation pressure, i.e. the force exerted by electromagnetic radiation on matter, date back to 1609 when German astronomer Johannes Kepler noticed that the tails of comets always point away from the Sun, being blown by what he believed to be a kind of solar breeze. The fact that electromagnetic radiation exerts a pressure upon a surface exposed to it was deduced theoretically by James Clerck Maxwell in 1871, and proven experimentally by Lebedev in 1900 and by Nichols and Hull in 1901.

Experiments on radiation pressure using lasers were performed by Arthur Ashkin in the early 70s at AT&T Bell Telephone Laboratories [1, 2]. He observed that objects of high refractive index were drawn towards the center of an unfocused laser beam, and pushed in the direction of propagation. Three-dimensional trapping of objects could be performed by using two counter-propagating beams. These observations led to the invention in 1986 of the so-called single beam gradient force optical trap [3]. In their seminal paper, Ashkin and co-workers demonstrated that a single, tightly focused laser beam could be used to trap microscopic dielectric particles in three dimensions. In the following year, Ashkin also pioneered the biological application of optical tweezers by trapping Tobacco mosaic virus and single *Escherichia coli* bacteria [4] and by manipulating particles within the cytoplasm of cells [5].

The past two decades have seen optical tweezers become a commonplace tool for

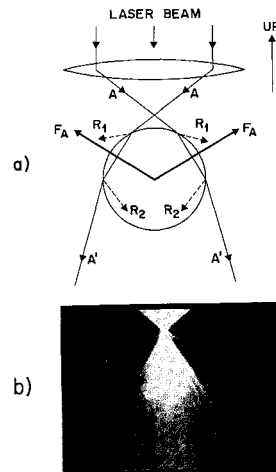


Fig. 1. a) Diagram showing the ray optics of a spherical Mie particle trapped in water by the highly convergent light of a single-beam gradient force trap. b) Photograph, taken in fluorescence, of a  $10\text{-}\mu\text{m}$  sphere trapped in water, showing the paths of the incident and scattered light rays.

**Figure 2.1** Figure from the 1986 seminal paper by Ashkin and co-workers, demonstrating single-beam gradient force optical trapping. From [5].



applications as diverse as cooling atoms [6] and confining Bose-Einstein condensates [7], manipulating and sorting microscopic particles [8], and probing cellular [9] and biomolecular properties [10]. The original setup, based on a laser beam focused through a high-numerical aperture microscope objective, has been improved to accommodate different experimental requirements. Some of the most exciting developments of the technique were introduced with the aid of laser beam shaping, as reported in 2.1.3 and 2.1.4. Optical tweezers can trap objects as small as 5 nm [11] and can exert forces exceeding 100 pN [12] with sub-pN resolution. This is the ideal range for exerting forces on biological and macromolecular systems and for measuring their responses. As a consequence, optical tweezers have also become a well-established technique for single-molecule studies, as reported in 2.1.5.

### 2.1.2 The mechanism of optical trapping

Although the theory behind optical tweezers is still being developed, the basic principles are straightforward for objects either much smaller than the wavelength of light or much larger. Small objects develop an electric dipole moment in response to the light's electric field, which is drawn up intensity gradients in the electric field, toward the focus. Such optical gradient force competes with the scattering component of radiation pressure, which pushes particles down the optical axis. Stable trapping thus requires the axial gradient force to dominate, and is achieved when the beam diverges rapidly enough away from the focal point. For this reason, optical tweezers are usually constructed around microscope objective lenses, whose high numerical apertures and well corrected aberrations focus light as tightly as possible. Larger objects act as lenses, refracting the rays of light and redirecting the momentum of photons. Intense optical fields can also induce forces *between* dielectric microparticles, leading to the phenomenon known as optical binding [13].

In order to understand the forces acting within optical tweezers, it is useful to adopt this latter approach, which through ray-optics makes the working principle immediately apparent. Since a light beam carries a linear momentum of  $h/\lambda$  per photon, the refraction of light by a transparent particle results in a change in photon momentum, and a corresponding reaction force acting on the object. In Figure 2.2 one can see that the force arising from refraction of a light ray acts to move the object towards the center of the beam. Furthermore, when the beam is tightly focused a force acts to lift the object towards the focus, thus creating a three-dimensional confinement. The ray-optics approximation holds when the wavelength of the laser is considerably smaller than the size of the object, and a model for evaluating the trapping force based on this approximation will be presented in further detail in 2.2.3.

### 2.1.3 Multiple tweezers

Optical tweezers can be configured using multiple beams to simultaneously trap more than one particle. Multiple beams of light passing simultaneously through

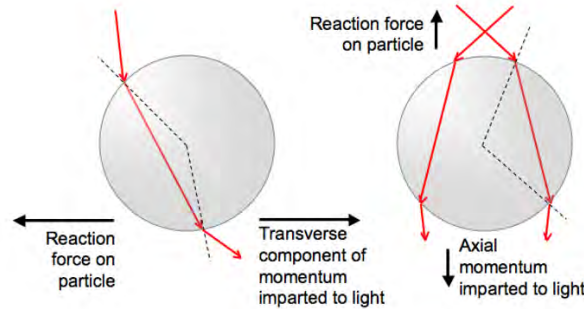


**Figure 2.2** Origin of the lateral and axial trapping force in optical tweezers within a ray optics approach.

the objective's entrance pupil focus indeed to multiple optical tweezers, the location of which is determined by the associated beam's angle of incidence and degree of collimation as it enters the objective. Multiple traps have been implemented by the rapid scanning of a single beam between two or more trap positions [14], or by splitting the incident beam to produce multiple light paths which are later recombined before entering the microscope. Their interference at the input pupil gives an amplitude and a phase pattern that characterize the downstream trapping pattern. Imposing the same modulations on a single incident beam at the input pupil would yield the same pattern of traps. Such wavefront modification can be performed by a computer-generated diffractive optical element (DOE), or hologram [8]. A computer-addressed spatial light modulator (SLM) can be used to project sequences of DOEs almost in real time [15, 16, 17, 18, 19] so that by slightly displacing the traps from one pattern to the next the particles are transferred along arbitrary three-dimensional (3D) trajectories. A different technique for generating multiple traps with an SLM is based on the generalized phase contrast (GPC) technique, where a pattern of phase modulations on the SLM is directly converted into the corresponding intensity modulation in the focal plane of the objective lens [20] and thus creates arbitrary planar trapping patterns. The conversion involves an annular phase plate similar to that used in the phase-contrast imaging method. The GPC approach avoids the need to calculate holograms and thus is extremely efficient. However, the spatial resolution of existing SLMs currently limits this technique to creating lateral traps rather than 3D optical tweezers.

#### 2.1.4 Manipulation with singular beams

The first application within optical tweezers of a laser beam that was not a fundamental Gaussian mode, was the use a high-order Hermite-Gaussian mode to align an asymmetric object within the optical trap [21]. Following that work, significant interest by many groups has been shown in using computer-generated holograms to produce Laguerre-Gaussian laser beams for use within optical tweezers. These

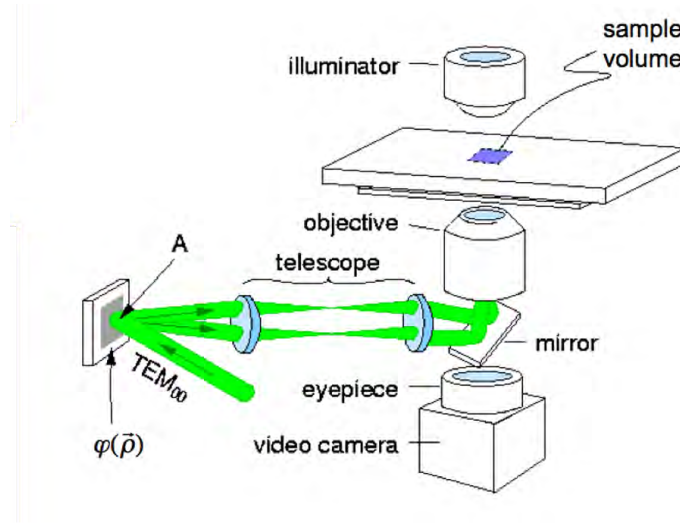


**Figure 2.3** Creation of multiple optical tweezers by using a computer-generated hologram. Projecting a collimated  $TEM_{00}$  laser beam through the input pupil of a microscope objective creates a single optical tweezers. The telescope in this implementation creates an image of the objective’s input pupil, centred at point A. Multiple beams passing through point A therefore pass into the objective lens to create multiple optical traps. A single  $TEM_{00}$  laser beam can be split into an arbitrary number of beams all emanating from point A by an appropriate computer-designed diffraction grating centred there. Adapted from [17].

beams can possess helical wavefronts which carry an orbital angular momentum [22]. Associated with the helical wavefronts is an annular intensity distribution with a zero on-axis intensity, also referred to as an “optical vortex”. The annular nature of these beams led to further applications within optical tweezers. Laguerre-Gaussian modes have enabled the three-dimensional confinement of low-refractive index particles, e.g. hollow glass spheres between 2 and 50  $\mu\text{m}$  in diameter [23, 24] and, more recently, of phospholipid-encapsulated micron-sized gas bubbles [25, 26] as it is reported in the present thesis. A further recent development in optical tweezers is the use of Bessel light beams. Bessel beams [27], which are frequently referred to as “diffraction free” beams, consists of a bright central spot surrounded by concentric rings of decreasing intensity. Over a characteristic propagation distance, the central region of the beam propagates without changing shape, creating an intensity distribution which has no gradient in the propagation direction. Bessel beams have been used within an optical tweezers to obtain stacking and guiding of trapped objects along the bright central core of the beam [28]. In this case the Bessel beam was created from a standard Gaussian beam using a specially fabricated glass axicon, although computer-generated holograms can also be used for the same purpose. Higher-order Bessel beams also have orbital angular momentum.

### 2.1.5 Optical tweezers as a force transducer

Manipulation of biological systems with optical tweezers began with relatively large objects, such as bacteria [4], yeast and mammalian cells. But optical trapping, combined with microsphere handles linked to molecules of interest enables also for single-molecule biophysics experiments [29]. It has been experimentally demonstrated by several authors [30, 31] that for small displacements from the equilibrium position within the trap, a particle experiences a restoring force which obeys Hooke's law,  $F = -\alpha x$ . As a consequence of the simple relationship observed between displacement  $x$  and restoring force  $F$ , an optical tweezers can be used as a force transducer. Once the trap stiffness  $\alpha$  is calibrated, force measurements are reduced to a position measurement. As a consequence, optical tweezers have quickly become a principal tool to measure directly the forces that hold together molecular structures. Optical tweezers can also be used for exerting external forces that modify reactions, to study the inter-conversion of mechanical and chemical energy in these processes. This area of research includes bio-chemical processes as diverse as DNA elasticity [32], protein folding [33], the behavior of molecular motors [34, 10], and in general the processes of protein-protein recognition [35]. Among the different methods available for single-molecule biophysics, optical tweezers have several unique advantages. The force on the trapped object can be calibrated against displacement and laser power, thus providing a method of direct, high-resolution force and position measurement ( $< 1$  pN and  $< 10$  nm, respectively). Also, the applicable force range ( $10^{-1} - 10^2$  pN) is highly relevant for biological systems [29]. A major disadvantage of optical tweezers is the potential for laser damage to active biological systems. Also, the data throughput is relatively low because only one molecule is handled at a time. A comparison of the optical tweezers-based force spectroscopy method with various single-molecule techniques can be found in Table 2.1. The relevant force ranges, minimum displacements, probe stiffness, practical advantages, and consequently the applications of each technique vary significantly.

## 2.2 Radiation trapping forces

### 2.2.1 Introduction

The interaction of a particle with the impinging light is defined by a momentum transfer due to scattering, absorption, or emission of photons, and by the fact that electric dipoles are drawn toward the highest amplitude of an electromagnetic field (dipole force). Generally, these forces are summarized by the Maxwell stress tensor (see Appendix A), which is a derivation of the conservation laws of electromagnetic energy and momentum [36]. These forces were described theoretically already in 1909 by Debye who applied the theory of Mie to describe the radiation pressure on spheres. The Mie scattering theory can be applied to spheres of arbitrary radius and dielectric susceptibility. However, a major issue in using this theory is the difficulty of deriving all the components of the electromagnetic field at the surface of the particle, since these include contributions

METHODS	$F_{\min-\max}$ (pN)	$x_{\min}$ (nm)	STIFFNESS (pN nm <sup>-1</sup> )	ADVANTAGES
Cantilevers	$10 - 10^5$	0.1	$1 - 10^5$	High spatial resolution Commercially available
Microneedles	$1 - 10^2$	1	$10^{-3} - 10^3$	Good operator control Soft spring constant
Flow field	$10^{-1} - 10^3$	10	n.a.	Rapid buffer exchange Simplicity of design
Magnetic Tweezers	$10^{-2} - 10$	10	n.a.	Specificity to magnets Ability to induce torque
Optical Tweezers	$10^{-1} - 10^2$	1	$10^{-7} - 1$	Specific manipulation High force resolution

**Table 2.1** Overview of single molecule manipulation techniques. Adapted from [29]

from the incident field as well as from the scattered and internal fields. A significant simplification of the problem can be achieved in the limit of a sphere of very large radius or very small radius compared to the wavelength. These two limiting cases will be discussed in Sections 2.2.3 and 2.2.4. Furthermore approximations are needed for describing the interaction with an arbitrary electromagnetic field distribution. In the case of optical tweezers, a description is needed of the highly focused Gaussian beam. The proper description of the fields in the focal region of a tightly focused Gaussian laser beam involves indeed strong axial electric field components at the focus, and thus requires the use of the vector wave equation. Even more complex is the description of the field distribution for a Laguerre-Gaussian mode, with a multi-ringed intensity distribution and helical wavefronts (see Section 3.3).

### 2.2.2 Radiation forces on spherical particles in arbitrary fields

First attempts to theoretically describe the forces on dielectric spheres in a focused laser beam were made by applying a ray-optics approach [37], which is valid for sphere diameters of  $D \approx \lambda_0$  and larger ( $\lambda_0$  is vacuum wavelength). This calculation using Snell's law and the Fresnel formulas does not take different sphere sizes into account since the phase front of the incident spherical wave is assumed not to change its shape in the focus. Gaussian optics satisfy the Helmholtz equation for small beam-divergence angles (i.e., when  $\sin(x) \approx x$ ) and were used for weak focusing of a laser beam [38] to calculate the radiation pressure with Mie theory. Gaussian beam optics improved by higher-order corrections [39] were used in an electromagnetic-field model to calculate trapping forces of highly focused laser beams [40]. Here expansion coefficients were calculated for the radial components of the incident and the scattered fields, which are used to determine trapping forces by means of the Maxwell stress tensor. This model delivers

good results as long as the sphere diameter is not larger than  $\lambda_0$ . However, it is restricted in applicability because realistic incident-field distributions cannot be simulated (e.g., the influence of the objective lens aperture, which cuts off the tails of a highly focused Gaussian beam or phase distortions such as spherical aberrations).

### 2.2.3 Ray-optics approximation

The full model for the ray-optics approximation was developed by Ashkin [37]. For this calculation, an incident parallel beam of arbitrary mode structure and polarization is considered, which enters a high-numerical aperture microscope objective, with a beam diameter equal to the lens objective aperture radius, and is focused ray by ray to a *dimensionless* spot  $f$ . The effect of neglecting the finite size of the beam focus is negligible for spheres much larger than  $\lambda$ . Consider first the force due to a single light ray of power  $P$  hitting a dielectric sphere at an angle of incidence  $\theta$  with incident momentum per second  $n_1 P/c$ , where  $n_1$  is the refractive index of the medium. Each photon (associated with a light ray) carries indeed energy

$$E = h\nu$$

where  $h = 6.6 \cdot 10^{-34}$  J s is the Planck's constant, and momentum

$$p = h/\lambda \tag{2.1}$$

The total number of photons in light with energy  $W$  is

$$N = W/h\nu \tag{2.2}$$

The momentum  $P_m = Np$  is, from Equations 2.1 and 2.2

$$P_m = \frac{W}{h\nu} \frac{h}{\lambda} = \frac{n_1 W}{c} \tag{2.3}$$

The force is the time derivative of the momentum, and the force in a medium of refractive index  $n_1$  is

$$F = \frac{n_1 P}{c} \tag{2.4}$$

where  $P$  is the incident light power in Watts. The acceleration of a 1- $\mu$ m-diameter sphere by the radiation pressure force calculated from Equation 2.4 is over  $10^5$  times larger than that of gravitation [1]. The total force on the sphere is the sum of contributions due to the reflected ray of power  $PR$  and the infinite number of emergent refracted rays of successively decreasing power  $PT^2, PT^2R, \dots, PT^2R^n, \dots$ .  $R$  and  $T$  are the Fresnel reflection and transmission coefficients of the surface at  $\theta_1$ . The net force acting through the origin  $O$

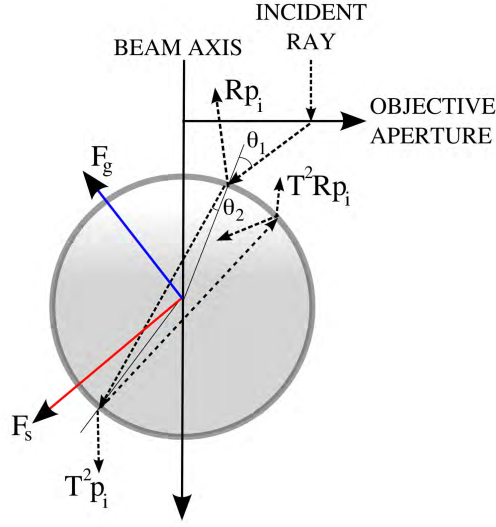


**Figure 2.4** Ray-optics model for optical trapping [37]. The scattering force  $F_s$  points in the direction of the incident ray, while the gradient force  $F_g$  is orthogonal to it. The angle of incidence is  $\theta_1$  and the angle of refraction is  $\theta_2$ .

can be broken into  $F_z$  and  $F_y$  components

$$F_z = \frac{n_1 P}{c} \left\{ 1 + R \cos 2\theta_1 - \frac{T^2 [\cos(2\theta_1 - 2\theta_2) + R \cos 2\theta_1]}{1 + R^2 + 2R \cos 2\theta_2} \right\} \quad (2.5)$$

$$F_y = \frac{n_1 P}{c} \left\{ R \sin 2\theta_1 - \frac{T^2 [\sin(2\theta_1 - 2\theta_2) + R \sin 2\theta_1]}{1 + R^2 + 2R \cos 2\theta_2} \right\} \quad (2.6)$$

where  $\theta_1$  and  $\theta_2$  are the angles of incidence and refraction. These formulas sum over all scattered rays. The forces are polarization dependent since  $R$  and  $T$  are different for rays polarized parallel or perpendicular to the plane of incidence. The intensities of the incident rays are weighted to account for the Gaussian intensity profile of the laser beam. By using a suitable weighting function, a  $TEM_{01}^*$  can also be implemented [37]. This approach was also used by Gahagan and Swartzlander [24] to compute the forces exerted by a focused Laguerre-Gaussian beam on a low-index particle (see Section 2.1.4; see Section 4.1.1 for further detail). Again, the approximation holds in the limit where the particle size is much larger than the beam wavelength. In particular, when a Laguerre-Gaussian beam is assumed to be focused to a dimensionless spot, the result also becomes independent of the size of the focused vortex, which is related to the *topological charge* of the Laguerre-Gaussian beam (see Section 3.3.2).

### 2.2.4 Point-dipole approximation

Harada and Asakura [41] investigated the range of validity of a point dipole approximation for Rayleigh particles ( $D \ll \lambda_0$ ) in a Gaussian beam. A zeroth-order approximation is used for the description of the Gaussian laser beam. A simple dipole model for the scattering force can be used in this case, since the particles scatter isotropically. The radiation force exerted on the induced dipole can be divided into the two components acting on a dielectric particle: the scattering and the gradient force. These are associated with momentum changes of the electromagnetic wave due to the scattering by the dipole, and the Lorentz force acting on the induced dipole, respectively. The dipole moment  $p(\mathbf{r}, t)$  of a dielectric sphere with radius  $a$  and dielectric constant  $\epsilon_s$  in a medium with a dielectric constant  $\epsilon_m$  particle, in the electric field  $E(\mathbf{r}, t)$ , is given by

$$p(\mathbf{r}, t) = 4\pi\epsilon_m a^3 \left( \frac{\epsilon_m - \epsilon_s}{\epsilon_m + 2\epsilon_s} \right) E(\mathbf{r}, t) = 4\pi n_m^2 \epsilon_0 a^3 \left( \frac{n^2 - 1}{n^2 + 2} \right) E(\mathbf{r}, t) \quad (2.7)$$

where  $n = n_s/n_m$  is the relative refractive index of the particle. The scattering force is given by

$$F_{scat}(\mathbf{r}) = \frac{C_{pr} \langle S(\mathbf{r}, t) \rangle_T}{c/n_{medium}} = \hat{z} \left( \frac{n_{medium}}{c} \right) C_{scat} I(\mathbf{r}) \quad (2.8)$$

being  $C_{pr}$  the cross-section for the radiation pressure of the particle, equal to the scattering cross-section  $C_{scat}$  for Rayleigh dielectric particles that scatter light isotropically:

$$C_{pr} = C_{scat} = \frac{8}{3} \pi (ka)^4 a^2 \left( \frac{n^2 - 1}{n^2 + 2} \right)^2 \quad (2.9)$$

where  $k$  is the wavenumber  $\frac{k}{2\pi}$ . The gradient force component, due to the Lorentz force acting on the dipole induced by the electromagnetic field, is given by

$$F_{grad}(\mathbf{r}) = \langle F_{grad}(\mathbf{r}, t) \rangle_T = \frac{2\pi n_m a^3}{c} \left( \frac{n^2 - 1}{n^2 + 2} \right) \nabla I(\mathbf{r}) \quad (2.10)$$

The expression of the gradient force in terms of the intensity distribution, in MKS units, allows to compare its absolute value with that of the scattering force. By a comparison of their results with a full electromagnetic model, Harada and Asakura showed that the dipole approximation holds for spheres in the size range of  $a > \lambda/20$  [41]. However, their model cannot be applied to a single-beam gradient optical trap since the zeroth-order approximation for the Gaussian beam is not valid for a highly focused Gaussian beam.

### 2.2.5 Additional forces in optical tweezers

The gradient force provides a restoring force which, over distances up to several hundred nanometers, is a linear function of displacement  $x$  [30]. For displacements within the range where the trapping force is elastic, i.e.  $F = -\alpha x$ , a



potential energy can also be defined, simply given by  $U = \frac{1}{2}\alpha x^2$  (Figure 2.5). Beyond the favorable balance between gradient force and scattering force dis-

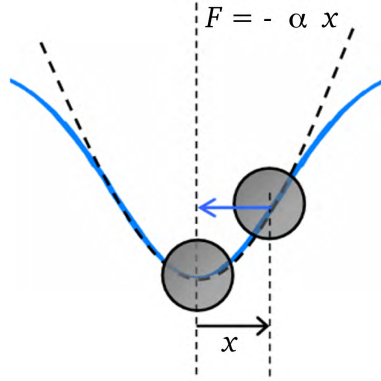


**Figure 2.5** Optical trapping potential experienced by a high-index particle in a Gaussian beam. For small displacements  $x$  from the equilibrium position the restoring force is elastic,  $F = -\alpha x$ , being  $\alpha$  the trap stiffness.

cussed in the previous Sections, the trap energy must overcome thermal energy  $k_B T$  to achieve stable trapping, being  $k_B = 1.38 \cdot 10^{-23} \text{ J K}^{-1}$  the Boltzmann's constant and  $T$  the temperature. The full force balance of a particle in an optical trap has to account for the presence of the suspension medium: the equation of motion governing the behavior of a trapped object of mass  $m$ , in a medium that gives a viscous damping  $\beta$  is a balance between inertial, viscous and elastic forces:

$$m \frac{\partial^2 x}{\partial t^2} + \beta \frac{\partial x}{\partial t} + \alpha x = 0 \quad (2.11)$$

where  $\alpha$  is the elastic constant or stiffness of the optical trap. In absence of damping, the result would be an oscillator with resonant frequency  $f_{res}$  given by

$$f_{res} = \frac{1}{2\pi} \sqrt{\frac{\alpha}{m}} \quad (2.12)$$

In typical biological applications, the stiffness  $\alpha$  of the optical tweezers is around  $0.05 \text{ pN nm}^{-1}$  and the trapped objects are around  $1 \mu\text{m}$  diameter (corresponding to a mass of  $5 \times 10^{-16} \text{ kg}$ ). Hence, the resonant frequency is approximately 50 kHz. However, because biological experiments must be performed in an aqueous medium, significant damping force arises. For micron-sized particles of radius  $r$ , moving in a fluid of viscosity  $\eta$ , the Stokes drag constant  $\beta$  is

$$\beta = 6\pi r \eta \quad (2.13)$$

For a sphere  $1 \mu\text{m}$  diameter in water,  $\beta = 1 \cdot 10^{-8} \text{ N s m}^{-1}$ . The combination of viscous damping and the spring-like stiffness of the optical tweezers gives rise to

a low pass filter with  $-3$  dB frequency  $f_0$  given by

$$f_0 = \frac{\alpha}{2\pi\beta} \quad (2.14)$$

For typical biological application this so-called “roll-off frequency” is well below 1 kHz. Since this is much lower than the resonant frequency, the motion is overdamped, therefore the inertial and gravitational forces can be neglected in a first approximation. The fluctuating thermal force (with energy  $k_B T$ ) produces a mean-squared deviation in position along one axis,  $\langle x^2 \rangle$ , calculated from

$$\frac{1}{2}\alpha \langle x^2 \rangle = \frac{1}{2} k_B T \quad (2.15)$$

Substituting typical values for temperature (biological experiments are typically performed at room temperature,  $\sim 300$  K) and tweezers stiffness, we find that the rms deviation in position is about 10 nm. To obtain a full description of the observed thermal motion, we find that it is distributed over a Lorentzian power density spectrum where the amplitude  $A_f$  of motion over each frequency interval  $f$  is given by

$$A_f = \frac{4k_B T \beta}{\alpha^2 (1 + f/f_0)^2} \quad (2.16)$$

These observations find direct application in the implementation of optical tweezers for force measurements. Such applications will be discussed in detail in Chapter 7.

## Bibliography

- [1] A. Ashkin. Acceleration and trapping of particles by radiation pressure. *Phys. Rev. Lett.*, 24:156, 1970.
- [2] A. Ashkin and J.M. Dziedzic. Optical levitation by radiation pressure. *Appl. Phys. Lett.*, 19:283, 1971.
- [3] A. Ashkin and J.M. Dziedzic. Optical trapping and manipulation of viruses and bacteria. *Science*, 235:1517–1520, 1987.
- [4] A. Ashkin, J.M. Dziedzic, and T. Yamane. Optical trapping and manipulation of single cells using infrared laser beams. *Nature (London)*, 330:769–771, 1987.
- [5] A. Ashkin, J.M. Dziedzic, J.E. Bjorkholm, and S. Chu. Observation of a single-beam gradient force optical trap for dielectric particles. *Opt. Lett.*, 11:288, 1986.
- [6] S. Chu, J.E. Bjorkholm, A. Ashkin, and A. Cable. Experimental observation of optically trapped atoms. *Phys. Rev. Lett.*, 57:314–317, 1986.

- 
- [7] D. M. Stamper-Kurn, M. R. Andrews, A. P. Chikkatur, S. Inouye, H.-J. Miesner, J. Stenger and W. Ketterle. Optical confinement of a Bose-Einstein condensate. *Phys. Rev. Lett.*, 80:2027–2030, 1998.
- [8] E.R. Dufresne, G.C. Spalding, M.T. Dearing, S.A. Sheets, and D.G. Grier. Computer-generated holographic optical tweezer arrays. *Rev. Sci. Instr.*, 72:1810–1816, 2001.
- [9] S.M. Block, D.F. Blair, and H.C. Berg. Compliance of bacterial flagella measured with optical tweezers. *Nature (London)*, 338:514–518, 1989.
- [10] K. Svoboda, C.F. Schmidt, B.J. Schnapp, and S.M. Block. Direct observation of kinesin stepping by optical trapping interferometry. *Nature (London)*, 365:721–727, 1993.
- [11] K. Svoboda and S.M. Block. Optical trapping of metallic Rayleigh particles. *Opt. Lett.*, 19:930–932, 1994.
- [12] L.P. Ghislain, N.A. Switz, and W.W. Webb. Measurement of small forces using an optical trap. *Rev. Sci. Instr.*, 65:2762–2768, 1994.
- [13] M.M. Burns, J.-M. Fournier, and J.A. Golovchenko. Optical binding. *Phys. Rev. Lett.*, 63:1233–1236, 1989.
- [14] K. Visscher, G.J. Brakenhoff, and J.J. Krol. Micromanipulation by multiple optical traps created by a single fast scanning trap integrated with the bilateral confocal scanning laser microscope. *Cytometry*, 14:105–114, 1993.
- [15] M. Reicherter, T. Haist, E.U. Wagemann, and H.J. Tiziani. Optical particle trapping with computer-generated holograms written on a liquid-crystal display. *Opt. Lett.*, 24:608–610, 1999.
- [16] J. Liesener, M. Reicherter, T. Haist, and H.J. Tiziani. Multi-functional optical tweezers using computer-generated holograms. *Opt. Commun.*, 185:77–82, 2000.
- [17] J.E. Curtis, B.A. Koss, and D.G. Grier. Dynamic holographic optical tweezers. *Opt. Commun.*, 207:169–175, 2002.
- [18] J. Leach, G. Sinclair, P. Jordan, J. Courtial, and M.J. Padgett. 3d manipulation of particles into crystal structures using holographic optical tweezers. *Opt. Expr.*, 12:220–226, 2004.
- [19] V. Emiliani, D. Cojoc, E. Ferrari, V. Garbin, C. Durieux, M. Coppey-Moisan, and E. Di Fabrizio. Wave front engineering for microscopy of living cells. *Opt. Expr.*, 13:1395–1405, 2005.
- [20] P.C. Mogensén and J. Glückstad. Dynamic array generation and pattern formation for optical tweezers. *Opt. Comm.*, 175:75–81, 2000.

- [21] S. Sato, M. Ishigure and H. Inaba. Optical trapping and rotational manipulation of microscopic particles and biological cells using higher-order mode Nd:YAG laser beams. *Electron. Lett.*, 27:1831–1832, 1991.
- [22] L. Allen, M.W. Beijersbergen, R.J.C. Spreeuw, J. Woerdman . Orbital angular momentum of light and the transformation of Laguerre-Gaussian laser modes. *Phys. Rev. A*, 45:8185–8189, 1992.
- [23] K.T. Gahagan and G.A. Swartzlander. Optical vortex trapping of particles. *Opt. Lett.*, 21:827, 1996.
- [24] K.T. Gahagan and G.A. Swartzlander. Trapping of low-index microparticles in an optical vortex. *J. Opt. Soc. Am. B*, 15:524–534, 1998.
- [25] P.A. Prentice, M.P. MacDonald, T.G. Frank, A. Cuschieri, G.C. Spalding, W. Sibbett, P.A. Campbell, K. Dholakia. Manipulation and filtration of low index particles with holographic Laguerre-Gaussian optical trap arrays. *Opt. Exp.*, 12:593–600, 2004.
- [26] V. Garbin, D. Cojoc, E. Ferrari, R.Z. Proietti, S. Cabrini, E. Di Fabrizio. Optical micromanipulation using Laguerre-Gaussian beams. *Japan. J. Appl. Phys.*, 44:5772–5775, 2005.
- [27] J. Durnin. Exact solutions for nondiffracting beams. I. The scalar theory. *J. Opt. Soc. Am. A*, 4:651–654, 1987.
- [28] V. Garcés-Chàvez, D. McGloin, H. Mellville, W. Sibbett and K. Dholakia . Simultaneous micromanipulation in multiple planes using a self-reconstructing light beam. *Nature*, 44:5772–5775, 2005.
- [29] C. Bustamante, J.C Macosko, and J.L. Wuite. Grabbing the cat by the tail: manipulating molecules one by one. *Nature Reviews*, 1:130–136, 2000.
- [30] J.E. Molloy and M.J. Padgett. Lights, action: optical tweezers. *Cont. Phys.*, 43:241–258, 2002.
- [31] K. Berg-Sorensen and H. Flyvbjerg. Power spectrum analysis for optical tweezers. *Rev. Sci. Inst.*, 75:594–612, 2004.
- [32] S.B. Smith, L. Finzi, and C. Bustamante. Direct mechanical measurements of the elasticity of single DNA molecules by using magnetic beads. *Science*, 258:1122–1126, 1992.
- [33] M. Carrion-Vazquez, A.F. Oberhauser, S.B. Fowler, P. E. Marszalek, S.E. Broedel, J. Clarke, and J.M. Fernandez. Mechanical and chemical unfolding of a single protein: a comparison. *Proc. Natl. Acad. Sci. USA*, 96:3694–3699, 1999.
- [34] A. Kishino and T. Yanagida. Force measurements by micromanipulation of a single actin filament by glass needles. *Nature*, 334:74–76, 1988.

- 
- [35] H. Nakajima, Y. Kunioka, K. Nakano, K. Shimizu, M. Seto, and T. Ando. Scanning force microscopy of the interaction events between a single molecule of heavy meromyosin and actin. *Biochem. Biophys. Res. Commun.*, 234:178–182, 1997.
- [36] J.D. Jackson. *Classical Electrodynamics*, pages 258–264. 3rd ed., Wiley, 1999.
- [37] A. Ashkin. Forces of a single-beam gradient laser trap on a dielectric sphere in the ray optics regime. *Biophys. J.*, 61:569–582, 1992.
- [38] J.S. Kim and S.S. Lee. Scattering of laser beams and the optical potential well for a homogeneous sphere. *J. Opt. Soc. Am.*, 73:303–312, 1983.
- [39] J.P. Barton and D.R. Alexander. Fifth-order corrected electromagnetic field components for a fundamental gaussian beam. *J. Appl. Phys.*, 66:2800–2802, 1989.
- [40] J.P. Barton, D.R. Alexander, and S.A. Schaub. Theoretical determination of net radiation force and torque for a spherical particle illuminated by a focused laser beam. *J. Appl. Phys.*, 66:4596–4602, 1989.
- [41] Y. Harada and T. Asakura. Radiation forces on a dielectric sphere in the Rayleigh scattering regime. *Opt. Comm.*, 124:529–541, 1996.



## Chapter 3

# Laser Beam Shaping for Optical Tweezers

The use of laser beam shaping through diffractive optical elements enables for complex optical trapping configurations. Exciting applications have been demonstrated, ranging from cell biology to colloidal sciences. The focus of the present Chapter is on laser beam shaping for low-index particles trapping. A general introduction on diffractive optical elements is given in Section 3.1. The methods and algorithms for DOEs calculation in use at TASC National Laboratory (CNR-INFM, LILIT group) are then reviewed in Sections 3.2 and 3.3. In particular, Section 3.3 reports on the diffractive optical elements developed in this thesis for trapping of individual and multiple low-index microparticles with Laguerre-Gaussian beams.

### 3.1 Introduction

Complex trapping geometries can be generated, and different tasks can be accomplished, by converting the fundamental Gaussian mode emitted from most commercial lasers into a beam of different intensity and phase structure. Diffractive optics enables for such a conversion. A general overview of the applications of laser beam shaping to optical tweezers was given in Section 2.1.1.

Diffractive optical elements (DOEs) are components that modify wavefronts by segmenting them and redirecting the segments through the use of interference and phase control. Different types of optical elements fall within the field of diffractive optics [1]:

- **Binary Optics:** DOE with a discrete number of phase-controlling levels. The simplest form has only two phase-levels, which introduce a 0 or  $\pi$ -phase difference on the incident wavefront.
- **Kinoform:** DOE whose phase-controlling surfaces are smoothly varying.
- **Computer-Generated Hologram:** DOE generated by discretizing a calculated interference pattern to a series of amplitude or phase levels. The useful wavefront is typically one of several orders generated by the pattern.

In its simplest form, a computer-generated hologram is produced from the calculated interference pattern that results when the desired (output) beam intersects the illuminating (input) laser beam at a small angle. The annular intensity distribution of a Laguerre-Gaussian beam can be obtained through computer generated holograms [2]. Focusing of a Laguerre-Gaussian beam through a microscope objective generates a so-called “donut” trap, used to trap objects with a lower refractive index than the surroundings [3].

The simplest DOE is a diffraction grating. It is known that if the incident wave is plane and monochromatic then the grating produces a set of diffraction orders propagating at different angles. If the incident wave is normal to the grating, then the directions of the incident and diffracted rays are related by the equation  $\sin \gamma^{(m)} = \frac{m\lambda}{D}$  where  $\gamma^{(m)}$  is the angle between the direction of the diffracted (into  $m^{\text{th}}$  order) rays and the normal to the grating;  $m$  is the order number;  $\lambda$  is the wavelength;  $D$  is the grating period. A DOE with a more complex structure may be considered as a grating with a variable period and orientation of lines. In this case, the ray-optics approach is not adequate to describe the energy distribution among diffraction orders. The wave approach allows describing the wavefront formed by the DOE. Assuming that the DOE is plane and infinitely thin, it can be characterized by a transmittance function  $t(\mathbf{x})$ , where  $\mathbf{x} = (x, y)$ , being  $x$  and  $y$  Cartesian coordinates in the DOE plane, and  $t$  a complex function in the general case. If the complex amplitude of the incident scalar monochromatic wave is  $W_{in}$ , then the complex amplitude of the transmitted wave in the DOE plane is  $W_{out}(\mathbf{x}) = t(\mathbf{x})W_{in}(\mathbf{x})$ . Calculating  $t(\mathbf{x})$ , and therefore the phase DOE needed to project a desired pattern of traps, is not particularly straightforward. The algorithms in use at LILIT group will be presented in Section 3.2.



### 3.1.1 Implementation of diffractive optical elements for optical tweezers

Diffractive optical elements can be designed to modulate the amplitude, phase or polarization of an incoming beam. However, phase-only modulation has become the preferred mode for applications to optical tweezers, because amplitude modulation implies diverting some of the incident beam energy from the desired output amplitude/phase distribution. Phase modulation can be achieved through relief modulation, as shown in Figure 3.1(a). When a wavefront first enters the

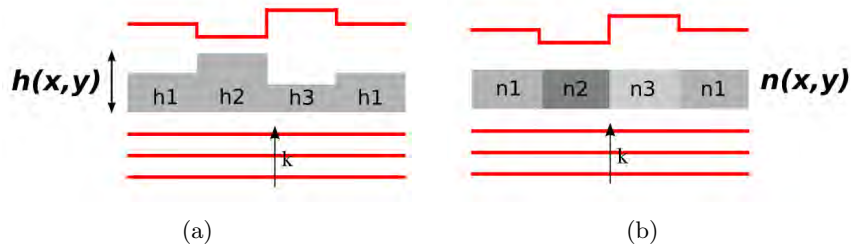


**Figure 3.1** A phase diffractive optical element encodes a pattern of phase shifts in thickness (a) or refractive index (b) modulation. A plane wave incident on the optical element acquires a spatially modulated phase.

material it is uniformly slowed to a speed  $v = c/n$ , where  $c$  is the speed of light in vacuum and  $n$  is the material's refractive index. Parts of the wavefront traveling through thinner regions of the optical element propagate outside the material at speed  $c$ , while sections remaining in the material are further delayed, with a phase delay proportional to the extra thickness of material. Consequently the relative phase at  $\mathbf{x} = (x, y)$  is proportional to the thickness,  $h(\mathbf{x})$

$$\Phi(\mathbf{x}) = 2\pi(n - 1) \frac{h(\mathbf{x})}{\lambda} \quad (3.1)$$

Similarly, phase delays can be encoded in a pattern of controlled variations of the index of refraction  $n(\mathbf{x})$ . The thickness  $h$  of the optical element is constant, and different segments of the wavefront undergo different phase delays according to the different optical path lengths  $\Delta(\mathbf{x}) = n(\mathbf{x}) h$ .

The computer-generated phase-modulation pattern can be etched on a transparent substrate (refractive index  $n$ ) in surface relief with conventional lithographic processes [4]. Using electron-beam lithography, DOEs with high spatial resolution and high spatial-bandwidth product (SBWP) can be fabricated [5]. Holographic patterns can also be transferred to a spatial light modulator (SLM) which imposes a prescribed amount of phase shift at each pixel in an array, by varying the local optical path length. Typically, this is accomplished by controlling the local orientation of molecules in a layer of liquid crystal. In 1999, Reicherter *et al.* [6] reported optical trapping with computer-generated holograms written on a liquid crystal display. They adapted a miniature display to produce a  $640 \times 480$  pixelated phase shifter with an update rate of 30 Hz. By calculating successive

holographic patterns they were able to manipulate three particles independently. The use of computer-generated holograms in combination with spatial light modulators have turned optical tweezers into very versatile tools. The hologram can be changed very quickly, at video-frame rate or faster, which allows dynamic trapping. This feature is exploited in our setup for trapping multiple low-index particles, as reported in Section 4.3.2.

**Practical considerations** Practical DOEs only diffract a portion of the incident light into the intended modes and directions. The maximum theoretical efficiencies for some types of holograms [2] are shown in Table 3.1 The undiffracted

Hologram Type	Maximum theoretical efficiency
Amplitude, binary, 100% modulation	10.1%
Amplitude, sinusoidal, 100% modulation	6.25%
Phase, binary, $\pi$ modulation	40.4%

**Table 3.1** Maximum theoretical efficiencies for different types of holograms. Adapted from [2]

portion of the beam typically forms an unwanted central spot. Furthermore, computer-generated DOEs have phase profiles that vary continuously between 0 and  $2\pi$ , which need to be discretized prior to implementation. This step necessarily introduces errors. Regardless of the implementation method, any practical phase DOE will also deviate from its design, and these deviations will further degrade its performance. In some implementations the central spot can be removed by spatially filtering the diffracted beam. Projecting holographic traps in the off-axis Fresnel geometry [7] also eliminates the central spot, but limits the number of traps that can be projected. Finally, practical DOEs also tend to project spurious “ghost” traps into symmetric positions. Spatially filtering the ghost traps generally is not practical, particularly in the case of dynamic implementation of DOEs on a SLM.

## 3.2 Computer-generated diffractive optical elements

Efficient iterative techniques, based on the thin-element approximation and the scalar diffraction theory, have been proposed to design phase DOEs with surface relief modulation in visible light [8]. The two approaches in use at the LILIT group for DOE calculation are *phase retrieval using iterative algorithms* (PRIA) followed by genetic algorithms for optimization [5] and *spherical waves propagation* [9]. The two approaches, which can be used for beam shaping and beam splitting, are shortly reviewed here; the full treatment can be found in [10].

### 3.2.1 Phase retrieval using iterative algorithms (PRIA)

The PRIA approach [11] starts from the desired intensity pattern  $I_f(\mathbf{x})$  that the DOE should generate in the output plane, being  $\mathbf{x} = (x, y)$  the vector position in a two-dimensional Cartesian system. This pattern is determined by the electric field of a collimated laser beam that is shaped by diffraction with a phase DOE and then transferred to the output plane by a suitable set of lenses. If the set of lenses is a shift invariant system the input and output fields are related by the coherent transfer function (CTF):

$$\mathcal{F}[E_f(\mathbf{x})] = \text{CTF} \mathcal{F}[E_g(\mathbf{x})] \quad (3.2)$$

where  $\mathcal{F}[*]$  is the Fourier transform,  $E_f(\mathbf{x})$  is the output field in the exit window and  $E_g(\mathbf{x})$  is the input field generated by the DOE in the system's entrance window. In order to provide high efficiency, a phase function  $\phi(\mathbf{x})$  is considered as the transfer function for the DOE, since a phase-only DOE doesn't affect the amplitude but only the phase of the transmitted wave. When illuminating the DOE with a collimated laser beam, the diffracted field at a distance  $z$  after the DOE will be:

$$E_g(\mathbf{x}; z) = P[A_g(\mathbf{x}) \exp[i\phi(\mathbf{x})]] \quad (3.3)$$

where  $A_g(\mathbf{x})$  is the amplitude of the illuminating beam and  $P[*]$  is the propagation operator, e.g. the Fourier transform for far-field and the Fresnel transform for near-field. The main problem of the DOE design is the calculation of the phase function,  $\phi(\mathbf{x})$ , such that the intensity distribution  $I_g(\mathbf{x}) = |E_g(\mathbf{x})|^2$  is proportional to the desired intensity distribution inside a specified window, called signal window (SW), of the diffracted pattern window (DPW). The approach used in the implementation of PRIA developed at LILIT is based on iterative algorithms that explore the space of phase distributions,  $\phi(\mathbf{x})$ , to retrieve the phase function that generates the desired intensity distribution. Only the intensity within the SW of the DPW is constrained, so that not only the phase in the whole DPW but also the intensity outside the SW represent a degree of freedom that can be used to facilitate the search. Phase retrieval using iterative algorithms starts with the initialization of the diffracted field,  $E_g(\mathbf{x}; z)$ . The phase function  $\phi(\mathbf{x})$  can be initialized with different phase distributions (e.g. random, constant, Gaussian). A randomly generated distribution was found to give the best result. One cycle of the iterative algorithm follows this sequence:

1. back-propagate the field  $E_g(\mathbf{x}; z)$  to the DOE plane;
2. replace the amplitude of the resulting field with the amplitude of the illuminating beam, while the phase remains unchanged;
3. propagate the field at a distance  $z$ ;
4. replace the amplitude of the resulting field with the desired amplitude,  $|E_g(\mathbf{x}; z)|$ , and calculate the mean square error (MSE) between the desired and obtained intensities

By repeating this cycle, the MSE decreases monotonically until the change of the MSE becomes insignificant and the algorithm is stopped. The phase calculated in the second step of the last iteration cycle is the phase function of the DOE. The drawback of this approach is that it doesn't allow controlling the desired intensity distribution in more than one output plane at a time, i.e. it doesn't allow generating three-dimensional intensity distributions. To this aim, the algorithm can be combined with other iterative schemes, based on genetic algorithms (GA) [5]. The phase is optimized first for each output plane; then the phase functions obtained for each plane define preliminary DOEs which are used to find the final solution in a GA scheme. An example is shown in Figure 3.2, where the desired intensity pattern in the output plane is a 2D array of four spots with the same intensities.

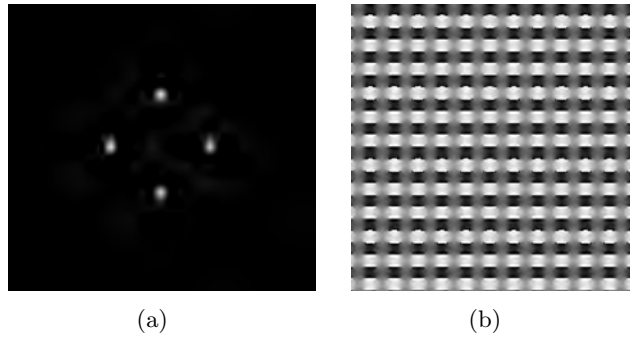


**Figure 3.2** Desired intensity pattern in the output plane (a) and DOE (b) calculated using the iterative algorithm presented in Section 3.2.1

### 3.2.2 Spherical waves propagation and superposition

The approach based on spherical wave propagation and superposition [9], provides an alternative solution to the problem of generating three-dimensional intensity distributions. The assumption is made that the DOE, illuminated by a set of point sources, generates a set of spots arranged in a prescribed configuration. This approach allows direct calculation of the DOE, avoiding the use of iterative algorithms. Assuming that both the light source and the generated pattern can be described by point sources that emit spherical waves, the phase function is derived from the propagation and superposition of the spherical wavefronts in the plane of the DOE. If the DOE is a thin element described by the transmittance function  $t(\mathbf{x}) = \exp[i\phi(\mathbf{x})]$  and  $W_{in}(\mathbf{x}; 0)$  is the complex amplitude of the incident wave, the complex amplitude of the output wave after the DOE will be:

$$W_{out}(\mathbf{x}; 0) = t(\mathbf{x})W_{in}(\mathbf{x}; 0) \quad (3.4)$$

where  $z = 0$  denotes the DOE plane. For a given input-output pair of waves satisfying the condition  $|W_{in}(\mathbf{x}; 0)| = |W_{out}(\mathbf{x}; 0)|$  the phase function is given by:

$$\phi : \phi(\mathbf{x}) = \{\arg[W_{out}(\mathbf{x}; 0)] - \arg[W_{in}(\mathbf{x}; 0)]\} \bmod 2\pi \quad (3.5)$$

If  $\{P_s(\mathbf{x}_s; z_s), s = 1 : N_s\}$  is the set of  $N_s$  points describing the source and  $\{P_g(\mathbf{x}_g; z_g), g = 1 : N_g\}$  the set of  $N_g$  points describing the generated spots, the expression for the incident and output wavefronts at the point  $P_e(\mathbf{x}_e; 0)$  in the DOE plane will be:

$$W_{in}(\mathbf{x}_e; 0) = \sum_s a_s \cos \psi_{s,e} \frac{\exp(ik\mathbf{r}_{s,e})}{\mathbf{r}_{s,e}} \quad (3.6)$$

$$W_{out}(\mathbf{x}_e; 0) = \sum_g a_g \cos \psi_{g,e} \frac{\exp(ik\mathbf{r}_{g,e} + \varphi_g)}{\mathbf{r}_{g,e}}$$

where  $a_{s(g)}$  are constants representing the amplitudes of the waves emitted by the point sources,  $\cos \psi_{s,e} = \frac{z_s}{\mathbf{r}_{s,e}}$  is the obliquity factor,  $\mathbf{r}_{s,e} = \overrightarrow{P_s P_e}$  is the distance between the point source  $P_s$  and the element  $P_e$  of the DOE,  $\varphi_g$  is the desired phase of the outgoing point  $P_g$  and  $k$  is the wavenumber  $k = \frac{2\pi}{\lambda}$ . Using equations 3.5 and 3.6 the phase function is calculated for the set of sampling points  $\{P_e(\mathbf{x}_e; z_e), e = 1 : N_e\}$  defined by an equally spaced square grid on the DOE. The number of the sampling points  $N_e$  is limited by the scalar diffraction approximation and by the sampling theorem to:  $\frac{D}{2\lambda} < N_e < \frac{D^2}{\lambda z}$ , where  $D$  is the lateral size of the DOE and  $z$  the distance from the source plane or the plane of the generated spots to the DOE. In general, equation 3.5 gives only an estimate of the phase function, which can be optimized using global optimization methods. Figure 3.3 shows some examples of DOEs, calculated using the spherical waves propagation method, which generate two- and three-dimensional configurations of focused laser spots.

### 3.3 Laguerre-Gaussian beams for optical tweezers

#### 3.3.1 Introduction

A beam with a transversal field component that includes an azimuthal complex exponential term of the form  $\exp(il\theta)$  exhibits helical wavefronts, see Figure 3.4. Since the phase value is not determined on the propagation axis, the beam is said to possess a *phase singularity* or a *vortex* of topological charge  $l$ , where the amplitude of the field vanishes. Laguerre-Gaussian beams (3.3.2) exhibit vortexes embedded within their amplitude distribution. Bessel beams also exhibit multi-ringed transversal structure, and are characterized by an integer index  $m$ , the order of the beam, that determines the charge of the vortex embedded in them. Since Laguerre-Gaussian beams are relatively easy to produce in the laboratory, they are the most common example of vortex beams.

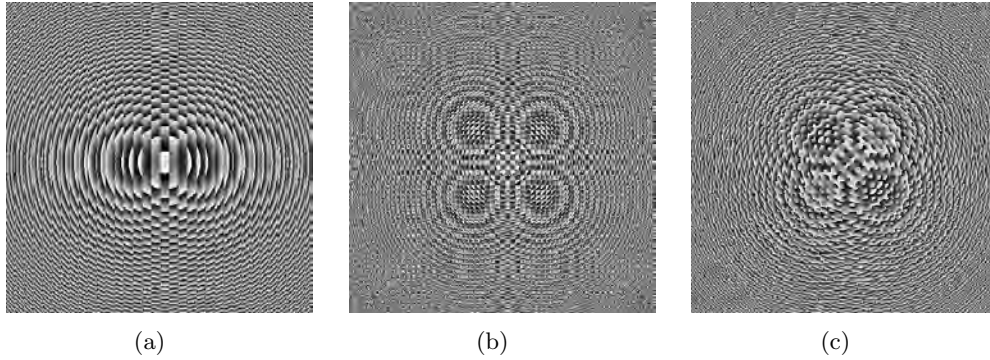


**Figure 3.3** DOEs calculated using the spherical waves approach described in Section 3.2.2. The DOE in (a) generates two spots and the DOE in (b) four spots; in both cases the generated spots are arranged in a two-dimensional array. The DOE in (c) generates five spots, arranged in the three-dimensional configuration.

The vanishing amplitude on the beam axis has found various applications within optical tweezers. When a Laguerre-Gaussian beam is tightly focused, it produces a so-called “donut” trap, also referred to as “dark” or “hollow” trap. In his early considerations of the trapping mechanism, Ashkin pointed out that it is only the off-axis rays that contribute to the axial trapping force. Indeed, his calculations predicted that modest improvements in the axial efficiency were possible using a  $TEM_{01}^*$  laser mode which has no on-axis rays [12]. With their zero on-axis intensity, Laguerre-Gaussian modes also satisfy this condition. Experimental results confirm that high-order Laguerre-Gaussian modes indeed improve the axial trapping efficiency of optical tweezers [13]. Optical vortex trapping also increased the versatility of optical tweezers by enabling confinement of low-index particles [3]. Particles exhibiting a lower refractive index than the surroundings are indeed repelled from the high-intensity region of a focused Gaussian beam since the gradient force is reversed. Once within the annular intensity distribution of a focused LG beam, a low-index particle experiences a gradient force again directed to the beam axis. Trapping of low-index particles, namely microscopic phospholipid-encapsulated gas bubbles used in ultrasound medical imaging, will be presented in Chapter 4.

### 3.3.2 Properties of Laguerre-Gaussian beams

The interest which arose in the 90s for the Laguerre-Gaussian laser modes was mostly due to their potential to carry orbital angular momentum. These modes were indeed first produced in order to demonstrate their orbital angular momentum content by Beijersbergen *et al.* in 1993 [14]. Laguerre polynomials are frequently encountered within quantum mechanics as the radial term in the solution to Schrödinger’s time-independent wave equation for a harmonic oscillator potential. As in the quantum mechanical example, the presence of an azimuthal phase term may be interpreted as indicating the presence of orbital angular mo-

mentum, hence the interest in those unusual modes.

Laguerre-Gaussian and Hermite-Gaussian beams appear as higher-order solutions to the conditions of resonance for the laser cavity. In general, transversal laser modes are best described by a product of a Hermite polynomial and a Gaussian, and are known as Hermite-Gaussian (HG) modes. In the case of a laser system, it would seem probable that given circular mirrors, the LG functions would provide the most accurate description of the transversal modes in a real laser, but this is not the case. Slight asymmetries in the laser cavity give rise to rectangular symmetry which results in product of Hermite polynomials providing a more accurate description [15]. Laser beams are thus usually described by use of a Hermite-Gaussian basis set, but a beam with helical wavefronts is best described in terms of the Laguerre-Gaussian basis set which has an explicit  $\exp(il\theta)$  phase term. Laguerre-Gaussian ( $\text{LG}_p^l$ ) modes are described by the indices  $l$  and  $p$  where the  $l$ -index relates to the azimuthal phase and the  $p$ -index to the number of additional concentric rings around the central zone. The form for the LG mode field amplitude is given by

$$u_p^l(r, \theta, z) = C_{pl} e^{-ikr^2/2R} e^{-r^2/w^2} e^{-i(2p+|l|+1)\tan^{-1}(z/z_r)} e^{-il\theta} (-1)^p (r\sqrt{2}/w)^{|l|} L_p^{|l|}(2r^2/w^2) \quad (3.7)$$

When  $l \neq 0$ , the helical phasefronts (see Figure 3.4) result in a phase discontinuity

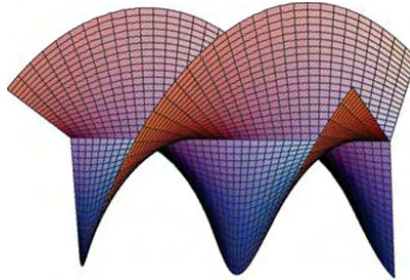


**Figure 3.4** Helical wavefront of a  $\text{LG}_0^3$  beam. Source: University of Glasgow

on the beam axis and a corresponding zero in the beam intensity. Consequently, the  $l \neq 0$  modes have the appearance of an annular ring for  $p = 0$ , or rings when  $p > 0$ . Note also the Gouy phase term  $\exp(-i(2p + |l| + 1)\tan^{-1}(z/z_r))$  which describes the phase change as a beam moves through the beam waist [16]. The index  $l$ , named *topological charge*, gives the number of  $2\pi$  cycles of phase in the azimuthal direction around the circumference of the mode, while  $p + 1$  gives the number of nodes across the radial field distribution. The radius of maximum field amplitude  $R_{I_{\max}}(z)$  is given by

$$R_{I_{\max}}(z) = \sqrt{\frac{\pi}{2}} \sqrt{l} w(z) \quad (3.8)$$

where  $w(z)$  is the radius of the Gaussian envelope [17].

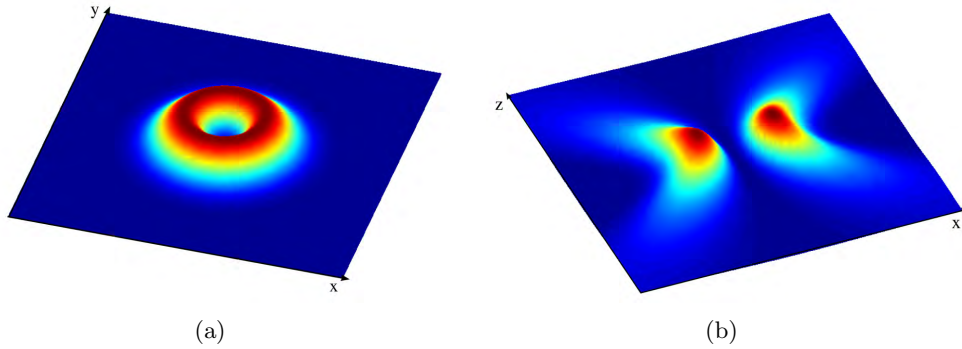


**Figure 3.5** Intensity distribution of a  $p = 0$  Laguerre-Gaussian beam. The field distribution of a mode with  $p = 0$  is a single ring with a  $2\pi l$  azimuthal phase variation. (a) Intensity profile in a plane orthogonal to the optical axis; (b) Intensity profile in a plane containing the optical axis

### 3.3.3 Laguerre-Gaussian beam converters

Conversion of a Gaussian laser beam into a Laguerre-Gaussian mode can be performed using diffractive optical elements. Following Equation 3.3.2, the phase profile of a Laguerre-Gaussian mode is simply given by

$$\phi_l(\mathbf{r}) = l\theta \text{ mod } 2\pi \quad (3.9)$$

where  $l$  is the beam's topological charge,  $\mathbf{r}$  denotes the radial position in the DOE plane and  $\theta$  the angle measured in the plane transversal to the direction of propagation. This phase profile can be simply implemented by a phase DOE, which by imposing the pattern of phase delays encoded by Equation 3.3.3 converts an incident plane wave into a helical wavefront. Such DOEs are shown in Figure 3.6 for different values of  $l$ . The DOEs were implemented on a reflection-type Hamamatsu X8267-11 spatial light modulator. The Gaussian mode coming from a 1064 nm continuous wave Yb-doped fiber laser was converted upon reflection on the SLM and coupled into the microscope objective of a Nikon TE2000 inverted microscope. The output beam shape was observed using a CCD or a CMOS sensor. Diffracted patterns in the focal plane are shown in Figure 3.7. Holography can also be used to generate an optical vortex. A computer-generated hologram can be easily computed by interfering a singular beam and a plane wave [2]. In general a phase singularity propagating along the  $z$  direction will have the form

$$E(r, \theta, z) = E_0 \exp(il\theta) \exp(-ikz) \quad (3.10)$$

where  $l$  is the topological charge of the singularity and  $\theta$  is the angle measured in the plane transversal to the direction of propagation. The interference pattern between the field in Equation 3.10 and a uniform plane wave  $u$  propagating at an angle to the  $z$  axis

$$u = \exp(-ik_x x - ik_z z) \quad (3.11)$$



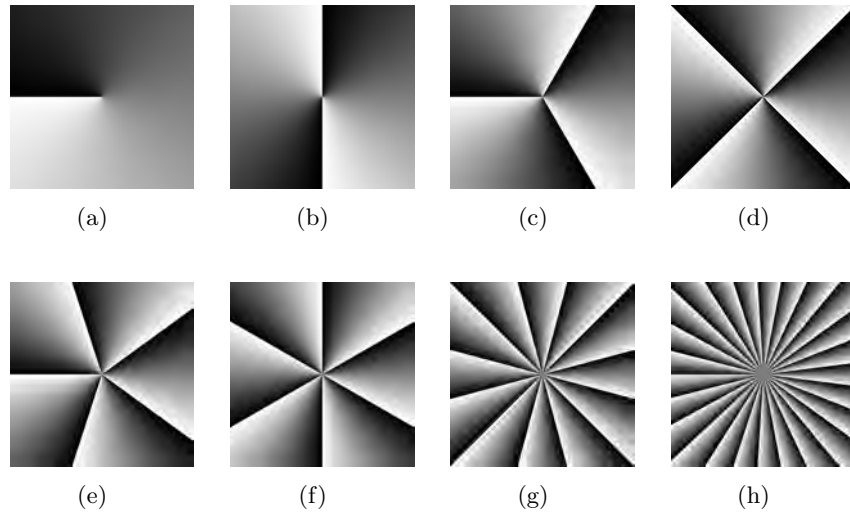


**Figure 3.6** Phase-only DOEs for generating Laguerre-Gaussian beams with different topological charge  $l$ . The DOE shown in (a) imposes one  $2\pi$  phase change for one revolution around the beam axis, i.e.  $l = 1$ . (b)  $l = 2$ . (c)  $l = 3$ . (d)  $l = 4$ . (e)  $l = 5$ . (f)  $l = 6$ . (g)  $l = 12$ . (h)  $l = 25$ .

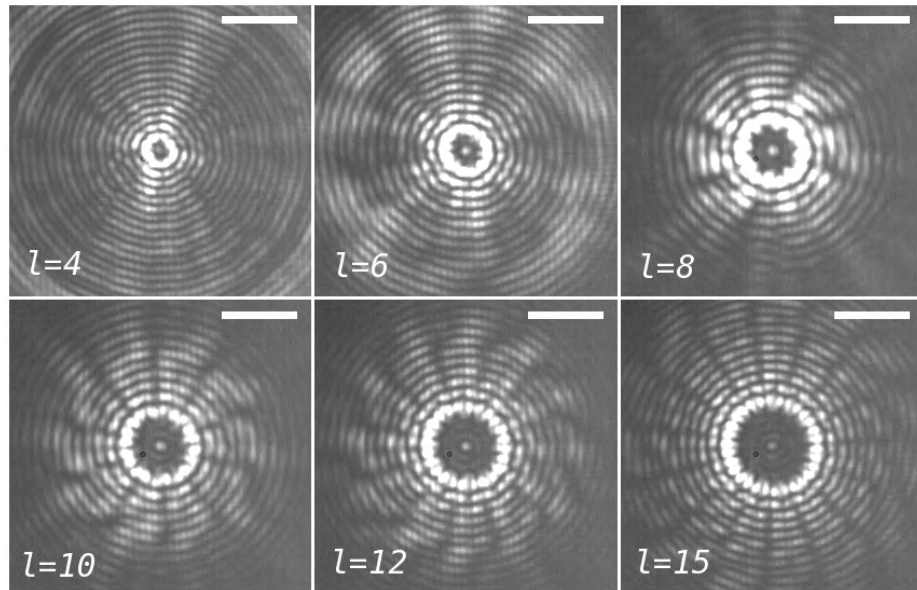


**Figure 3.7** The intensity patterns in the focal plane of a microscope objective are shown for different topological charges  $l$ . The diameter of the "donut" can be precisely controlled by tuning  $l$ . The conversion of a 1064 nm Gaussian beam into a Laguerre-Gaussian mode is performed using DOEs such as those shown in Figure 3.6, implemented on a spatial light modulator. The undiffracted light focuses to a spot in the center of the donut. Magnification of the objective  $60\times$ . Scalebar:  $10\mu\text{m}$ .

gives, in the plane  $z = 0$ , the intensity pattern expressed by:

$$I = 1 + E_0^2 + 2E_0 \cos(k_x x - l\theta) \quad (3.12)$$

The resulting phase singularity hologram is shown in Figure 3.8 for  $l = 4$ . It is similar to a grating, except that there is a defect in the center. The experimental intensity pattern in the output plane for  $l = 24$  is shown in Figure 3.9. This

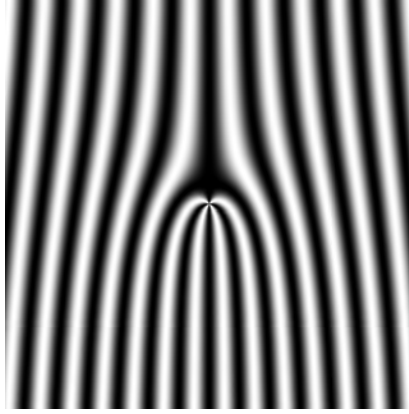


**Figure 3.8** Computer generated hologram which, illuminated by a plane wave, generates a singular beam with topological charge  $l = 4$

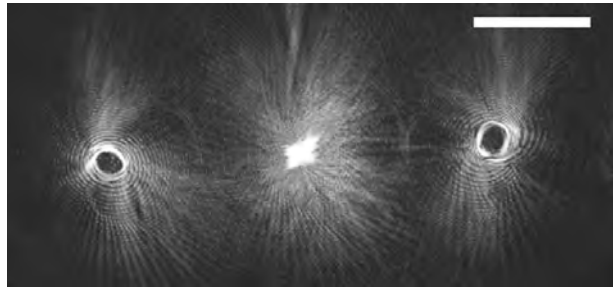


**Figure 3.9** Diffraction pattern in the far-field obtained by converting a Gaussian beam through a computer-generated hologram similar to the one shown in Figure 3.8. The first diffraction orders are shown (+1 and  $-1$ ). They are singular beams with  $l = 24$ . The zero order is visible in the center. Scalebar:  $10 \mu\text{m}$

hologram can be implemented also as an amplitude DOE, with a lower efficiency in the desired diffracted order.

### 3.3.4 Multiple helical beams

Multiple donut traps can be generated by superimposing the phase pattern  $\phi_N(\mathbf{r})$  encoding for an array of  $N$  optical traps ( $\text{mod } 2\pi$ ) to the pattern of phase delays  $\phi_l(\mathbf{r})$  encoding for a Laguerre-Gaussian beam with topological charge  $l$ , see e.g. [18]. The DOE  $\phi_N(\mathbf{r})$  can be calculated with the PRIA method as presented in 3.2.1. This approach can be used to generate 2D arrays of donut traps and to trap multiple low-index particles. The diffracted patterns and a discussion on their efficiency for low-index particle trapping are reported in Section 4.3.2. An alternative method is to embed multiple vortices in the incident beam, by dividing the DOE into several sections, each containing a single-vortex phase

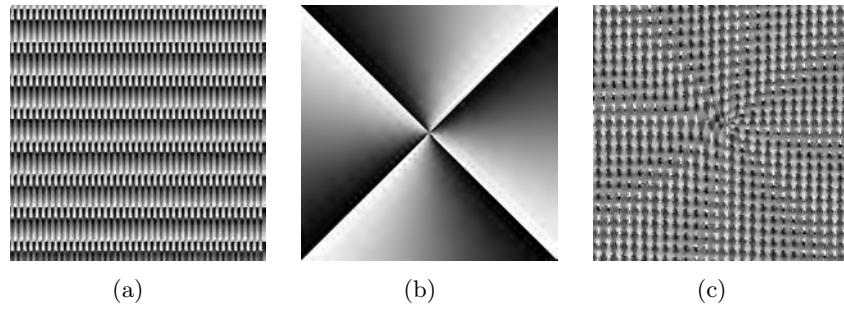


**Figure 3.10** Phase-only DOEs for generating multiple Laguerre-Gaussian beam. The DOE shown in (a) generates three spots. The one in (b) generates a LG beam with  $l = 4$ . (c) By superimposing the two phase patterns, a DOE is obtained which generates 3 LG traps.

mask, see e.g. [19, 20]. The distance between the  $N$  juxtaposed DOEs can be adjusted to change the distance between the traps in the output plane. The  $768 \times 768$  pixels DOEs which generate a single trap are resized so that  $N$  of them fit in the SLM's active area ( $768 \times 768$  pixels). The maximum number of

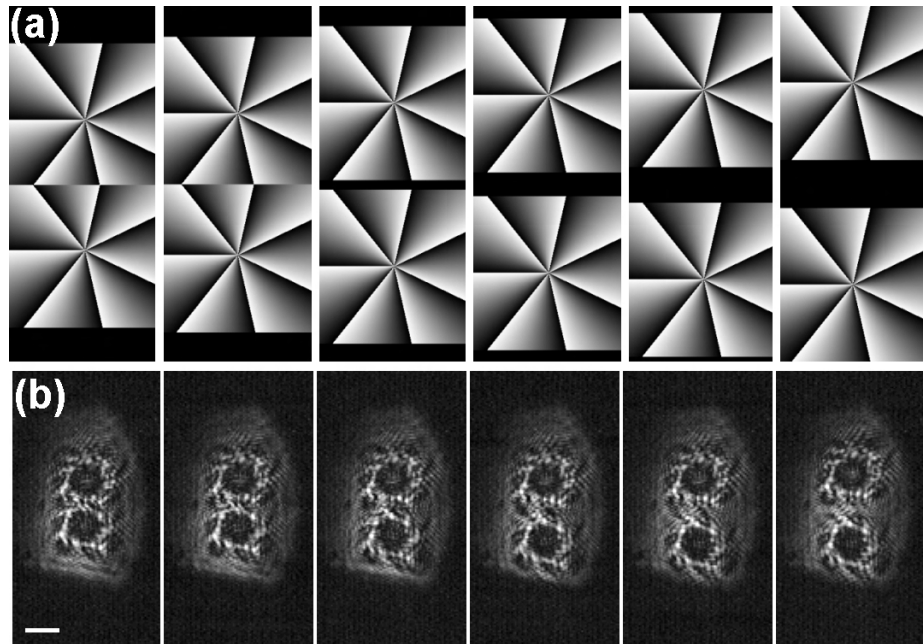


**Figure 3.11** Two Laguerre-Gaussian beams (b) are produced using tiled DOEs (a). The distance between the two traps can be controlled by changing the distance between the singularities in the DOE plane. White scalebar left bottom in (b):  $5 \mu\text{m}$ .

traps which can be generated in this case is limited by the minimum number of pixels needed to encode for each individual trap, and therefore on the topological charge. For our purposes, the quality of the generated vortices is defined by

their suitability for low-index particles trapping. Following [20], the minimum number of pixels required to generate quality vortices was investigated for a range of topological charges. Figure 3.12 shows an example of the diffracted patterns for increasing number of pixels in the case  $l = 5$ . The information on the minimum number of pixels required for generating a quality vortex is crucial when larger arrays of traps are created, as it determines the maximum number of traps that can be generated. Figure 3.13 shows an array of nine donut traps generated by juxtaposing nine  $200 \times 200$  pixel DOEs encoding for  $l = 4$  vortices. It is straightforward to apply this method also for generating arrays of traps with different sizes. The approach based on embedding multiple vortices in

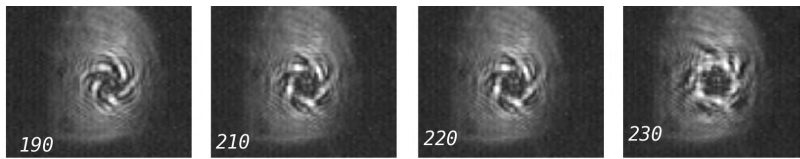


**Figure 3.12** Diffracted patterns for increasing number of pixels in the case  $l = 5$ . The number of pixels is indicated at the bottom left of each frame.

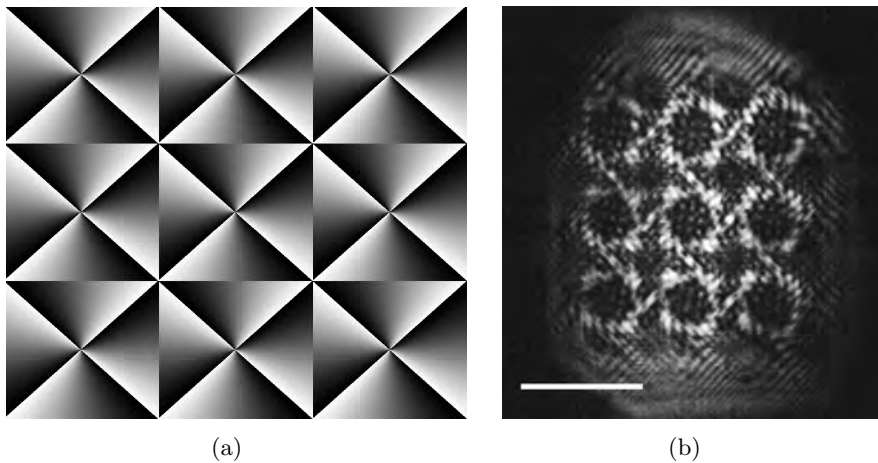


**Figure 3.13** The DOE shown in (a) is obtained by tiling  $3 \times 3$  DOEs encoding for a Laguerre-Gaussian beam. Each DOE is resized to  $200 \times 200$  pixels before juxtaposing nine of them. The final DOE is  $600 \times 600$  pixels. In (b) the diffracted pattern is shown: nine donut traps are embedded in the incident beam.

the incident beam is efficiently used to trap low-index particles and control their relative distance with  $\mu\text{m}$  precision. Such an ability is exploited in this thesis to study the interaction between microbubbles in an ultrasound field, see Section 6.3.

### 3.3.5 3D position of a vortex trap

Donut traps can also be generated in 3D configurations. In the simplest case, where the position of an individual trap is controlled, the phase profile of the converted beam has a very simple form: a spherical wave is superimposed to the singular beam

$$\phi(r, \theta) = \exp(il\theta) \frac{\exp(ikr)}{r_0} \quad (3.13)$$

leading to a phase pattern as shown in Figure 3.14. The distance  $r_0$  is taken from the point originating the spherical wave to the DOE plane. When the generated

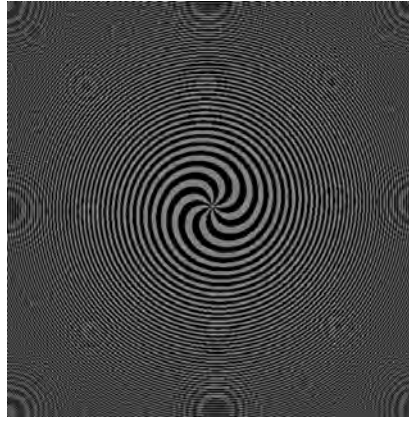


**Figure 3.14** DOE generated by superimposing a spherical wave to the singular beam. When the generated beam is focused through a microscope objective, it focuses at a distance  $z$  from the objective's focal plane according to the parameter  $r_0$  describing the superimposed spherical wave, see Equation 3.3.5.

beam is focused through a lens, the vortex is reconstructed on a plane at a distance from the focal plane which depends on  $r_0$  and on the total magnification of the optical system.

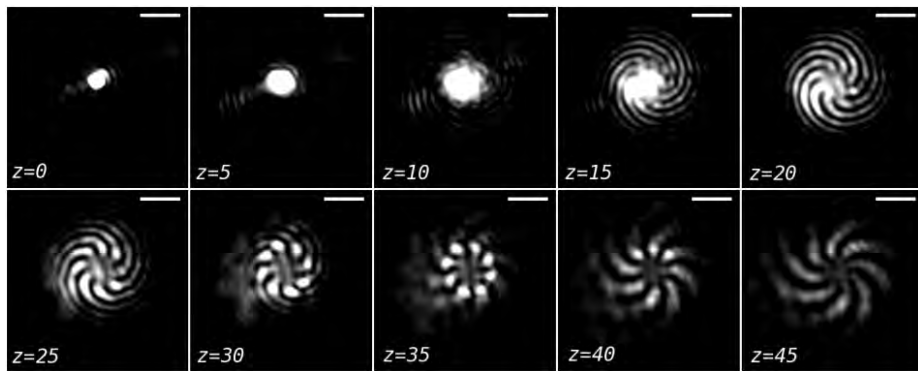


**Figure 3.15** The vortex generated by the DOE in Figure 3.14 focuses at a distance  $z \sim 30 \mu\text{m}$  from the objective's focal plane ( $z = 0$ ). The sequence of frames shows the beam profile at increasing distance ( $5 \mu\text{m}$  steps).

## 3.4 Conclusions

We investigated different methods for generating “donut” traps for low-index particles. We developed DOEs that enable to convert a Gaussian laser beam to give arbitrary configurations of donut traps. Our goal is to trap and manipulate phospholipid-coated microbubbles and to study their properties upon insonation with medical diagnostic ultrasound. Implementation of the DOEs in an optical tweezers setup, for 2D and 3D trapping of microbubbles, is reported in Chapter 4.

## Bibliography

- [1] D.C. O’Shea, T.J. Suleski, A.D. Kathman, and D.W. Prather. *Diffraction Optics - Design, Fabrication, and Test*. SPIE Press, 2004.
- [2] H. He, N.R. Heckenberg, and H. Rubinsztein-Dunlop. Optical particle trapping with higher-order doughnut beams using high-efficiency computer generated holograms. *J. Mod. Opt.*, 42:217–223, 1995.
- [3] K.T. Gahagan and G.A. Swartzlander. Optical vortex trapping of particles. *Opt. Lett.*, 21:827, 1996.
- [4] E.R. Dufresne, G.C. Spalding, M.T. Dearing, S.A. Sheets, and D.G. Grier. Computer-generated holographic optical tweezer arrays. *Rev. Sci. Inst.*, 72:1810–1816, 2001.
- [5] D. Cojoc, E. Di Fabrizio, L. Businaro, S. Cabrini, F. Romanato, L. Vaccari, and M. Altissimo. Design and fabrication of diffractive optical elements for optical tweezers arrays by means of e-beam lithography. *Microelectr. Eng.*, 61-62:963–969, 2002.
- [6] M. Reicherter, T. Haist, E.U. Wagemann, and H.J. Tiziani. Optical particle trapping with computer-generated holograms written on a liquid-crystal display. *Opt. Lett.*, 24:608–610, 1999.
- [7] A. Jesacher, S. Fürhapter, S. Bernet and M. Ritsch-Marte. Diffractive optical tweezers in the Fresnel regime. *Opt. Exp.*, 12:2243–2250, 2004.
- [8] M. Bernhardt, F. Wyrowski, and O. Bryngdahl. Iterative techniques to integrate different optical functions in a diffractive phase elements. *Appl. Opt.*, 30:4629–4635, 1991.
- [9] D. Cojoc, V. Emiliani, E. Ferrari, R. Malureanu, S. Cabrini, R.Z. Proietti, and E. Di Fabrizio. Multiple optical trapping by means of diffractive optical elements. *Japan J. Appl. Phys.*, 43:3910–3915, 2004.
- [10] E. Di Fabrizio, D. Cojoc, V. Emiliani, S. Cabrini, M. Coppey-Moisan, E. Ferrari, V. Garbin, and M. Altissimo. Microscopy of biological sample through

- advanced diffractive optics from visible to x-ray wavelength regime. *Micr. Res. Techn.*, 65:252–262, 2004.
- [11] R.W. Gershberg and W.O. Saxton. A practical algorithm for the determination of phase from image and diffraction plane pictures. *Optik*, 35:237–246, 1972.
- [12] A. Ashkin. Forces of a single-beam gradient laser trap on a dielectric sphere in the ray optics regime. *Biophys. J.*, 61:569–582, 1992.
- [13] A.T. O’Neil and M.J. Padgett. Axial and lateral trapping efficiency of Laguerre-Gaussian modes in inverted optical tweezers. *Opt. Commun.*, 193:45–50, 2001.
- [14] L. Allen, M.W. Beijersbergen, R.J.C. Spreeuw, J. Woerdman. Orbital angular momentum of light and the transformation of Laguerre-Gaussian laser modes. *Phys. Rev. A*, 45:8185–8189, 1992.
- [15] M. Padgett, J. Arlt, N. Simpson, L. Allen. An experiment to observe the intensity and phase structure of Laguerre-Gaussian laser modes. *Am. J. Phys.*, 64:77–82, 1996.
- [16] L. Allen, S.M. Barnett, and M.J. Padgett. *Optical Angular Momentum*, pages 109–113. Institute of Physics Publishing, Bristol, UK, 1990.
- [17] M.J. Padgett and L. Allen. The Poynting vector in Laguerre-Gaussian laser modes. *Opt. Commun.*, 121:36–40, 1995.
- [18] J.E. Curtis, B.A. Koss, and D.G. Grier. Dynamic holographic optical tweezers. *Opt. Commun.*, 207:169–175, 2002.
- [19] D. Rozas, C.T. Law, and G.A. Swartzlander. Propagation dynamics of optical vortices. *J. Opt. Soc. Am. B*, 14:3054–3063, 1997.
- [20] N. Chattrapiban, E.A. Rogers, I.V Arakelian, R. Roy, and W.T. Hill. Laser beams with embedded vortices: tools for atom optics. *J. Opt. Soc. Am. B*, 23:391–399, 2006.



## Chapter 4

# Low-index particles trapping using Laguerre-Gaussian beams

In this Chapter optical trapping and manipulation of microbubbles will be presented. First an overview is given of the various methods that have been proposed for manipulating such particles in 4.1. Our approach is based on Laguerre-Gaussian beams and the experimental setup is described in 4.2. Three-dimensional trapping is demonstrated and more complex trapping configurations based on multiple Laguerre-Gaussian beams are introduced in 4.3.

## 4.1 Introduction

### 4.1.1 Optical trapping of low-index particles

Particles cannot be trapped by a conventional Gaussian laser beam when their relative refractive index  $n = \frac{n_{particle}}{n_{medium}}$  is smaller than 1. From the equation for the gradient force (2.2.4)

$$F_{grad}(\mathbf{r}) = \frac{2\pi R^3}{c} \left( \frac{n^2 - 1}{n + 2} \right) \nabla I(\mathbf{r}) \quad (4.1)$$

where  $R$  is the particle radius,  $c$  the speed of light and  $I$  the beam intensity profile, one can see indeed that  $F_{grad}$  is directed along the gradient when  $n > 1$ , and in the opposite direction when  $n < 1$ .

Arthur Ashkin, in his experiments on radiation pressure, reported in 1974 optical levitation of low-index particles [1]: hollow glass spheres 30-60  $\mu\text{m}$  in diameter were launched into a vertically directed  $\text{TEM}_{01}^*$  laser beam and levitated into the air. A force arising from intensity gradients was already known to repel low-index particles away from high-intensity regions. A beam with a dark core was in fact used to confine the particles in a minimum-intensity region, but the scattering force directed along the direction of propagation of the beam could only be counterbalanced by the downward pull of gravity. Unger *et al.* achieved stable levitation of small air bubbles (10-30  $\mu\text{m}$  in radius) in water in a downward directed visible laser beam [2].

Gradient force optical traps [3] were introduced in 1986. A force due to intensity gradients in a tightly focused Gaussian beam was observed not only on a plane transversal to the optical axis, but also along the optical axis, pointing towards the beam focus. Scattering force, always pointing along the propagation direction, can thus be counterbalanced by the axial component of the gradient force when focusing is strong enough, enabling three-dimensional confinement of particles. Low-index particles trapping in a gradient force optical trap was first demonstrated by Gahagan and Swartzlander in 1996 [4]. They thereafter studied two different low-index particles systems: hollow glass spheres (12 – 36  $\mu\text{m}$  in diameter) in water and water droplets (4 – 20  $\mu\text{m}$  in diameter) in acetophenone [5]. Particles were trapped by a charge  $l = 1$  vortex trap generated by computer generated hologram from a  $\lambda = 514 \text{ nm}$  Gaussian laser beam, focused through a 100 $\times$ , NA = 1.30 microscope objective. In both cases the wavelength  $\lambda$  and the focused beam radius  $w_f$  were thus smaller than the particle radius. Therefore, a ray-optics model could be used to describe trapping: an equilibrium position where gradient force counterbalances scattering force was predicted and experimentally observed.

Several methods have been implemented for generating traps for low-index particles: two-dimensional trapping can be performed by using an interferometric pattern of bright and dark fringes [6], by generating donut-shaped intensity distributions using the generalized phase-contrast method [7], or by using a Bessel beam [8]. In addition to focusing an optical vortex beam, three-dimensional trap-

ping can be obtained also by rapidly scanning the beam in a circular trajectory [9].

### 4.1.2 Optical trapping of UCA microbubbles

Trapping and micromanipulation of low-index particles recently found important applications in the field of medical imaging. Micron-sized gas bubbles, encapsulated by a thin shell of phospholipids, proteins or polymer, are commonly used in ultrasound diagnostic imaging as a contrast enhancer. In recent years their application to drug delivery has also been proposed, although a deeper understanding of their behavior remains elusive. One of the difficulties comes from the fact that bubbles stick together forming bubble clusters, and it is in general difficult to control their position due to buoyancy and flow. Various groups have recently demonstrated optical trapping and manipulation of ultrasound contrast agent microbubbles, to the purpose of studying their properties with controlled and repeatable experimental conditions [10, 11, 12]. Phospholipid-stabilized gas microbubbles, such as those used in our experiments, will behave as low-index particles even if they have a high-index shell [4]. The phospholipid monolayer is in fact a few nanometers thick, and the behavior of the microparticle is dominated by the interaction of the laser with the gas core.

## 4.2 Materials and Methods

We developed an optical tweezers setup based on Laguerre-Gaussian beams for trapping and micromanipulation of ultrasound contrast agent microbubbles. Laguerre-Gaussian beams, generated by converting a Gaussian laser beam through diffractive optical elements (DOEs), are focused through high-numerical aperture objectives, generating “donut” traps. For our system, even for a beam with topological charge  $l = 1$ , the diameter of the focused  $\lambda = 1064$  nm LG beam is larger than the bubble size. The effect on trapping is that a transversal confinement due to the gradient force is still observed, but along the optical axis the scattering force is not counterbalanced by the gradient force. Therefore, a gradient force optical trap cannot be obtained. Microbubbles can nevertheless be confined in 3D using an upright microscope (see Figure 4.1(a)), by balancing bubble buoyancy in a levitation-type trap [2]. Detail of the setup is given in the present Section, while information on the DOEs used for beam shaping can be found in Section 3.3.

### 4.2.1 Optical setup

The setup for three-dimensional trapping of microbubbles was based on a Olympus LUMPLFL objective,  $100\times$  magnification with numerical aperture  $NA = 1.0$  in water. A schematic view of the setup is presented in Figure 4.1(b). A  $TEM_{00}$  beam coming from a single-mode, continuous-wave (CW) Yb-doped laser fiber (YLM-10W from IPG Photonics,  $\lambda = 1064$  nm, linear polarization, collimated) is converted into a Laguerre-Gaussian beam by a phase DOE displayed on the

parallel aligned nematic liquid crystal display (LCD) of a Hamamatsu X8267-11 spatial light modulator (SLM). The SLM exhibits high efficiency (40%) and the phase mode can be completely decoupled from the intensity mode, allowing very accurate implementation of multi-level phase-only DOEs. A maximum phase shift higher than  $2\pi$  is provided at 1064 nm with 19 lp/mm maximum display resolution on the LCD, over an active area of 20 mm  $\times$  20 mm. A 3 $\times$  beam expander is used to fill the whole LCD area with the incident beam (initial diameter 7 mm). Ideally no zero order should be observed when converting the incident beam with phase-only DOEs, but due to the mismatch of the phase levels implemented on the LCD from the calculated values (see 3.1.1), the sum over the DOE of the phase modulation errors introduced by the LCD gives a constant term in the DOE plane, which is converted in the zero (non diffracted) order peak in the observation plane. Lenses  $L_2$  and  $L_3$  (plano-convex,  $f_2 = 150$  mm,  $f_3 = 75$  mm) resize the beam to properly fill the 100 $\times$  objective back aperture. The beam is directed into the objective with a dichroic mirror. The mirror allows the visible light used for illumination to pass through. Transmission imaging is performed through the second objective (either Olympus SLCPlanFl 40 $\times$  or Nikon Plan Fluor 60 $\times$ ). The image is collected by a CMOS sensor (Epix, VCA1281 sensor; 1280  $\times$  1024 maximum resolution, sensor size 8.96 mm  $\times$  7.17 mm, pixel size 7  $\mu$ m  $\times$  7  $\mu$ m).

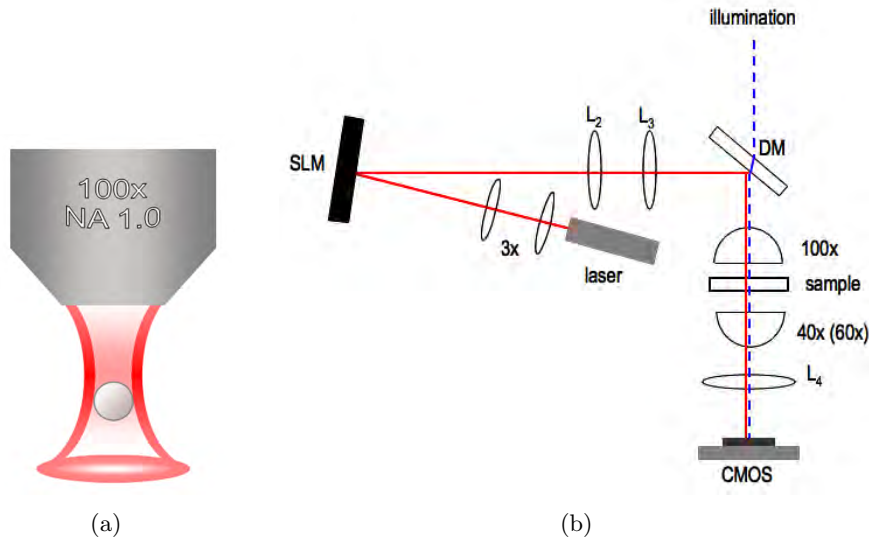


**Figure 4.1** (a) Schematic of a microbubble in a Laguerre-Gaussian optical trap. (b) Optical setup. 1064 nm Ytterbium doped fiber laser; SLM: spatial light modulator; 3 $\times$ : beam expander;  $L_2$  and  $L_3$ : 150 mm and 75 mm plano-convex lenses; DM: dichroic mirror, directs laser beam into microscope objective and lets illumination light pass through; 100 $\times$ : water immersion objective for trapping; 40 $\times$ , 60 $\times$ : long-working distance objectives for imaging; the sample cell is mounted on a  $x, y, z$  piezo stage.

### 4.2.2 Sample preparation

Ultrasound contrast agent (UCA) microbubbles are phospholipid-shelled gas bubbles, ranging in radius from 0.5 to 4  $\mu\text{m}$ . The inner gas core refractive index is assumed to be unity. Since their shell is a phospholipid monolayer, approximately 2 nm thick, it is negligible compared to the bubble size. Therefore, they behave as low-index particles. The experimental contrast agent BR-14 used throughout this thesis was provided by Bracco Research S.A. (Geneva, Switzerland). A solution containing UCAs is injected in a sample cell made of two microscope cover slides separated by 100-150  $\mu\text{m}$  thick sticky tape. The sample cell is placed on a programmable piezo-actuated translation stage (Nanocube, Melles-Griot) to enable trapping force measurements.

### 4.2.3 Forces balance on UCA microbubbles

Gas bubbles and water exhibit, in addition to the refractive index mismatch, a strong density mismatch. The buoyancy force is relevant in determining the forces balance. The buoyancy force acting on gas microbubbles ranging in radius  $R$  between 0.5  $\mu\text{m}$  and 4  $\mu\text{m}$  is calculated from

$$F_{\text{buoy}} = \frac{4}{3}\pi R^3 (\rho_{\text{water}} - \rho_{\text{air}}) g \quad (4.2)$$

The following values are used for the constants:  $\rho_{\text{water}} = 1000 \text{ kg m}^{-3}$  (water density at 4 °C);  $\rho_{\text{air}} = 1 \text{ kg m}^{-3}$ ;  $g = 9.81 \text{ m s}^{-2}$ . Some values for the buoyant force are shown in Table 4.1. The terminal rise velocity is also shown. The drag force is given by

$$F_{\text{drag}} = 6\pi R \eta_{\text{water}} v \quad (4.3)$$

where  $\eta_{\text{water}} = 1.01 \cdot 10^{-3} \text{ N s m}^{-2}$  is the viscosity of water at 20 °C. The terminal rise velocity is then given by

$$v_{\text{max}} = \frac{v_{\text{bubble}} \rho_{\text{water}} g}{6\pi R \eta} \quad (4.4)$$

The values of velocity for buoyant bubbles show that, short after sample preparation, even the smallest bubbles reach the top surface of the sample cell. For UCA microbubbles, the buoyancy force ranges from 0.01 pN ( $R = 0.5 \mu\text{m}$ ), up to 3 pN ( $R = 8 \mu\text{m}$ ), and it is counterbalanced by the optical scattering force enabling 3D confinement.

The transversal trapping force can be estimated by measuring the escape velocity from the trap. The programmable piezo stage enables for controlled displacements of the sample with increasing velocity. When the drag force experienced by the microbubble due to the viscous fluid flow overcomes the trapping force, an estimate of the maximum trapping force is obtained. Typical values of the transversal trapping force of 10 – 20 pN are observed for UCA microbubbles ( $R \sim 0.5 \div 4 \mu\text{m}$ ), corresponding to velocities of the order of 100  $\mu\text{m s}^{-1}$ .

Bubble radius ( $\mu\text{m}$ )	Buoyant force (pN)	Velocity ( $\mu\text{m s}^{-1}$ )
0.5	0.01	0.54
1.0	0.04	2.16
1.5	0.14	4.86
2.0	0.33	8.63
2.5	0.64	13.49
3.0	1.11	19.43
3.5	1.76	26.44
4.0	2.63	34.54

**Table 4.1** Values of buoyancy force and velocity are estimated for free gas bubbles immersed in water. Typical radii for BR-14 UCAs. The contrast agent is provided by Bracco Research S.A. (Geneva). The effect of the phospholipid shell is assumed to be negligible.

## 4.3 Results

### 4.3.1 Three-dimensional trapping

Low-index particles are not entering spontaneously the Laguerre-Gaussian trap, since they experience a force directed away from high-intensity regions. One procedure for trapping individual microbubbles is to block the beam, align its position over a microbubble, and then unblock the beam. The microbubble will be confined in the dark center of the beam, and will reach an equilibrium position in the vertical direction (below the trapping objective focal plane) given by the balance between scattering force, gradient force and buoyancy. The DOE encoding for a suitable vortex can be chosen depending on the microbubble's size. In Figure 4.2 a sequence shows trapping of an individual UCA microbubble, 3–4  $\mu\text{m}$  diameter, away from the top surface of the sample cell. The topological charge of the vortex is  $l = 7$ . After trapping the microbubble with the procedure described above, we change its distance from the chamber wall by positioning the sample chamber upwards. The final position is at 20  $\mu\text{m}$  from the wall. Imaging is performed through the second objective (see Figure 4.1) and is thus decoupled from trapping; this enables easy monitoring of the system. The sequence in Figure 4.2 shows a microbubble stably trapped away from the top surface; the sequence is taken by scanning the second objective along the optical axis with 5  $\mu\text{m}$  steps. The first image (a) is taken at the top surface of the sample cell. The following images are taken 5  $\mu\text{m}$  (b), 10  $\mu\text{m}$  (c), 15  $\mu\text{m}$  (d) and 20  $\mu\text{m}$  (e) below the top surface. We thus proved that confinement is three-dimensional. We could move the trapped microbubbles at a desired position up to 100 – 150  $\mu\text{m}$  away from the top surface.

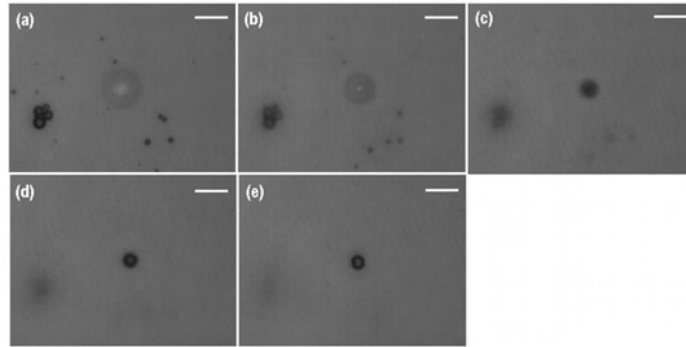


**Figure 4.2** Individual,  $3\ \mu\text{m}$  microbubble trapped with a  $l = 7$  Laguerre-Gaussian beam. The images are taken by scanning the imaging objective,  $5\ \mu\text{m}$  step. Initially the bubbles at the top surface are shown (a) and the trapped microbubble is out of focus. Images (b), (c) and (d) show the top surfaces going out focus and the trapped bubble coming in focus. In the last image (e) the trapped microbubble is in focus,  $20\ \mu\text{m}$  below the initial position. Scale bar  $10\ \mu\text{m}$ .

### 4.3.2 Multi-trapping of microbubbles

Here we report our procedures for sorting microbubbles from a set, trapping them on an array, and dynamically changing the trapping configuration [11, 13, 14]. As mentioned above, low-index particles are not entering spontaneously the donut trap. The procedure of blocking the beam, aligning its position over a microbubble, and unblocking the beam is not as reliable for multiple trapping as it is for individual trapping. Microfabricated DOEs do not allow to change in real-time the configuration of traps, and multiple trapping can only be achieved when the concentration of microbubbles ensures a reasonable probability for trapping multiple microbubbles when the beam is unblocked [10]. A procedure for subsequently switching on multiple traps is highly desirable. The ability of individually switching on and off individual traps is crucial when the particles in solution exhibit a large size distribution, as it happens for UCA microbubbles, and one is interested in sorting particles of a given size. This ability was demonstrated by applying the generalized phase contrast [7] but only two-dimensional confinement was obtained.

**2D multi-trapping** Preliminary experiments were performed to demonstrate multiple trapping by coupling the laser beam into an inverted microscope (Nikon TE2000) [13]. This gives only two-dimensional confinement, since buoyancy is not counterbalanced, and the microbubbles are trapped at the sample chamber wall. A sequence of DOEs was prepared with an increasing number of donut traps, following the method presented in 3.3.4. In Figure 4.3 the sequence of DOEs for subsequently switching on three identical traps with  $l = 8$  is shown: we locate the first trap, obtained by displaying the first DOE (a), and block the beam; we position the trap over the first microbubble to trap, and finally unblock

the beam. The second microbubble is selected and after positioning where the second trap will be generated, we change DOE (b) so that two traps are obtained and the second microbubble is trapped. The same procedure allows to trap the third microbubble by switching to the third DOE (c) and so on for bigger arrays. This procedure allows effective sorting of the desired microbubbles from the set, as shown in Figure 4.4.

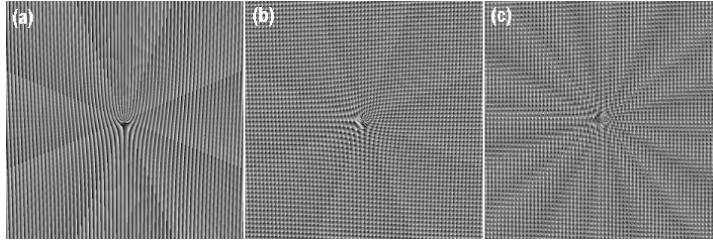


**Figure 4.3** Sequence of DOEs for multiple microbubbles trapping. They encode respectively for one (a), two (b) and three (c) vortex traps with  $l = 8$ . They are displayed in sequence on the SLM and allow to trap subsequently microbubbles chosen from the set.

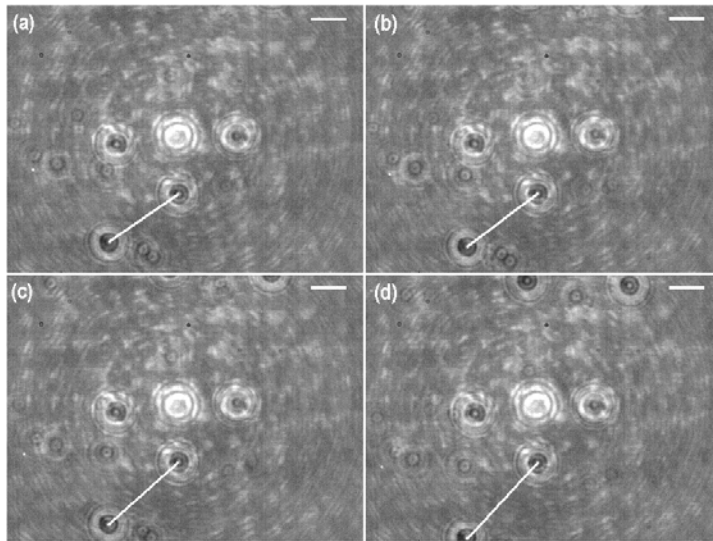


**Figure 4.4** Three microbubbles are stably trapped in identical  $l = 8$  vortex traps. They have been subsequently trapped by displaying a suitable sequence of DOEs on the SLM. The stability of trapping is proved by moving the sample chamber. Scale bar:  $10 \mu\text{m}$ .

**3D multi-trapping and manipulation** Here we show an additional functionality that can be implemented by displaying a sequence of DOEs on the SLM. After trapping multiple microbubbles in a desired configuration following the procedure described above, we can control the distance and move the microbubbles,



simply by changing the DOE. We calculate sequences where small displacements are imposed so that the microbubbles remain stably trapped. In Figure 4.5 the intensity pattern generated by such a sequence is shown: the bright spot in the center is the on-axis non-diffracted order, the topological charge of the two vortices is  $l = 8$ . With a first DOE a single trap is generated (a) beside the optical axis; a second DOE switches on the second trap (b) in a symmetric position relative to the optical axis. The following DOEs change the distance between the two traps. Manipulation of two microbubbles is then performed, as shown in Figure 4.6. Two microbubbles are trapped following the procedure described before. They are then positioned  $30 \mu\text{m}$  below the top surface, by moving the sample chamber upwards. Images on different planes are taken by scanning the imaging objective. The first image shows the microbubbles at the top surface of the sample chamber, and the laser intensity in this plane (a). The second image (b) shows a plane half the way between the top surface and the plane where two microbubbles are trapped. The third image (c) shows two microbubbles,  $4 - 5 \mu\text{m}$  diameter, stably trapped on a plane  $30 \mu\text{m}$  below the initial plane. The following images (d, e, f, g, h) show manipulation and control of the distance between the two microbubbles: by changing the DOEs displayed on the SLM, the distance is slowly increased. For our applications, the approach of embedding multiple

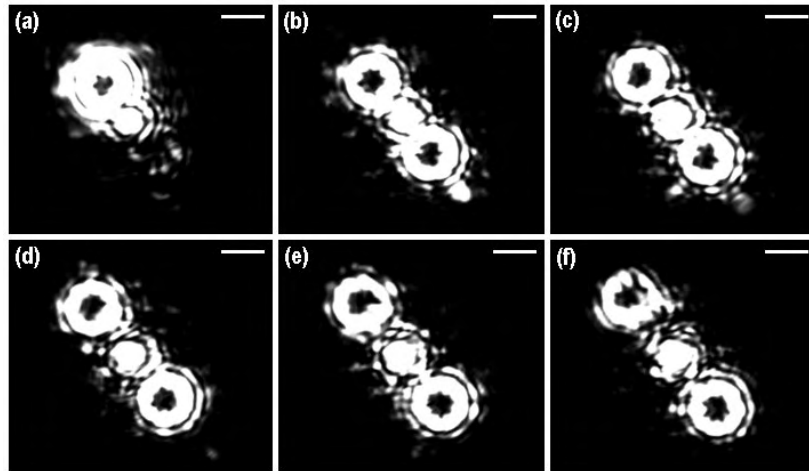


**Figure 4.5** Laser beam shaping for two microbubbles trapping and manipulation. The images show the laser intensity obtained in the microscope objective focal plane for 6 different DOEs. The first DOE displayed on the SLM creates a trap for the first bubble (a). The second DOE adds a trap for the second bubble (b) in a symmetric position with respect to the optical axis. The sequence of DOEs that follows changes the distance between the two traps (c, d, e, f). Scale bar:  $10 \mu\text{m}$ .

vortexes in the beam, using the DOEs presented in 3.3.4, is very convenient, and even more flexible. The distance between the two juxtaposed DOEs can be indeed easily adjusted to change the distance between the two traps, resulting in precise, sub- $\mu\text{m}$  positioning of the two trapped microbubbles, as in Figure 3.11 [14]. Furthermore, it is straightforward to adjust the trap size for each individ-

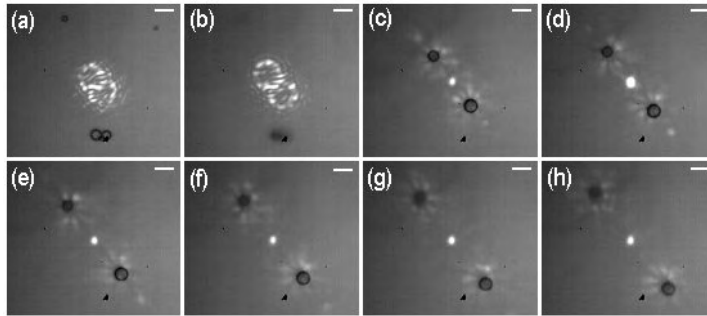


**Figure 4.6** Two microbubbles trapping and manipulation. The first image shows the microbubbles at the top surface of the sample cell and the laser intensity in this plane (a). The second image shows a plane between the top surface and the plane where two microbubbles are trapped (b). The third image shows two microbubbles stably trapped on a plane  $30\ \mu\text{m}$  below the initial plane (c). The following images (d, e, f, g, h) show manipulation and control over the distance between the two microbubbles by changing the DOEs displayed on the SLM. Scale bar:  $5\ \mu\text{m}$ .

ual trap. Figure 4.7 shows a set of bubble pairs, with different sizes, trapped at different distances, using this approach.

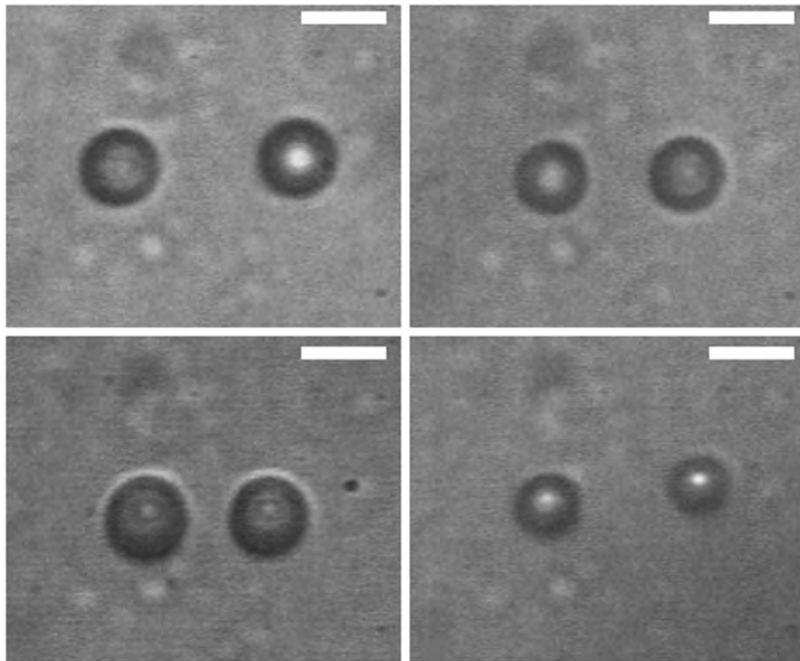


**Figure 4.7** Trapping of two UCA microbubbles. A filter blocks the laser light so that the traps are not visible. Bubbles with different sizes are trapped, and the distance can be precisely controlled. Scale bar:  $5\ \mu\text{m}$ .

## 4.4 Conclusions

Optical trapping of ultrasound contrast agent microbubbles is demonstrated. The confinement is observed to be three-dimensional in a setup where a downward directed trapping beam counterbalances buoyancy. Single and multiple Laguerre-Gaussian beams are generated by means of phase diffractive optical elements implemented on a programmable spatial light modulator. The use of a SLM allows to reconfigure the traps in real time: this enables full control on multiple microbubbles. Positioning and manipulation can also be performed, by simply switching between suitable DOEs. Microbubbles can be trapped in arrays that can be subsequently rearranged by individually switching on and off each trap, and by changing the distance between the traps. These features can be exploited for studying ultrasound contrast agent microbubbles under well-controlled, repeatable experimental conditions.

## Bibliography

- [1] A. Ashkin and J.M. Dziedzic. Stability of optical levitation by radiation pressure. *Appl. Phys. Lett.*, 24:586–588, 1974.
- [2] B.T. Unger and P.L. Marston. Optical levitation of bubbles in water by the radiation pressure of a laser beam: An acoustically quiet levitator. *J. Acoust. Soc. Am.*, 83:970–975, 1988.
- [3] A. Ashkin, J.M. Dziedzic, J.E. Bjorkholm, and S. Chu. Observation of a single-beam gradient force optical trap for dielectric particles. *Opt. Lett.*, 11:288, 1986.
- [4] K.T. Gahagan and G.A. Swartzlander. Optical vortex trapping of particles. *Opt. Lett.*, 21:827, 1996.
- [5] K.T. Gahagan and G.A. Swartzlander. Trapping of low-index microparticles in an optical vortex. *J. Opt. Soc. Am. B*, 15:524–534, 1998.
- [6] M.P. McDonald, L. Paterson, W. Sibbet and K. Dholakia. Trapping and manipulation of low-index particles in a 2-dimensional interferometric optical trap. *Opt. Lett.*, 26:863–865, 2001.
- [7] P.J. Rodrigo, V.R. Daria and J. Glückstad. Real-time interactive optical micromanipulation of a mixture of high- and low-index particles. *Opt. Exp.*, 12:1417–1425, 2004.
- [8] V. Garcés-Chávez, D. McGloin, H. Mellville, W. Sibbett and K. Dholakia. Simultaneous micromanipulation in multiple planes using a self-reconstructing light beam. *Nature*, 44:5772–5775, 2005.
- [9] K. Sasaki, M. Koshioka, H. Mishawa, N. Kitamura, H. Masuhara. Optical trapping of a metal particle and a water droplet by a scanning laser beam. *Appl. Phys. Lett.*, 60:807–809, 1992.

- [10] P.A. Prentice, M.P. MacDonald, T.G. Frank, A. Cuschieri, G.C. Spalding, W. Sibbett, P.A. Campbell, K. Dholakia. Manipulation and filtration of low index particles with holographic Laguerre-Gaussian optical trap arrays. *Opt. Exp.*, 12:593–600, 2004.
- [11] V. Garbin, D. Cojoc, E. Ferrari, R. Kulkarni, and E. Di Fabrizio. Manipulation of single and multiple low-index particles by means of optical tweezers. In *Proc. SPIE Vol. 5930*, pages 492–501, 2005.
- [12] P.H. Jones, E. Stride and N. Saffari. Trapping and manipulation of microscopic bubbles with a scanning optical tweezer. *Appl. Phys. Lett.*, 89:081113, 2006.
- [13] V. Garbin, D. Cojoc, E. Ferrari, R.Z. Proietti, S. Cabrini, E. Di Fabrizio. Optical micromanipulation using Laguerre-Gaussian beams. *Japan. J. Appl. Phys.*, 44:5772–5775, 2005.
- [14] V. Garbin, D. Cojoc, E. Ferrari, E. Di Fabrizio, M.L. Overvelde, M. Versluis, S.M. van der Meer, N. de Jong, and D. Lohse. Time-resolved nanoseconds dynamics of ultrasound contrast agent microbubbles manipulated and controlled by optical tweezers. In *Proc. SPIE Vol. 6326*.

## Chapter 5

# Combined optical micromanipulation and ultra-high speed imaging of UCA microbubbles

The dynamics of micron-sized phospholipid-coated gas bubbles, which are used in medical ultrasound imaging as contrast enhancers, can be studied using an ultra-high speed camera which can record up to 25 million frames per second (5.1). These studies are hampered by buoyant forces that make the bubbles rise, by bubble clustering, or by the presence of hard and soft interfaces that change the dynamics of the bubbles. Optical tweezers allow overcoming such difficulties (5.2). The microbubbles can be trapped and manipulated by Laguerre-Gaussian laser beams, so that their position relative to a neighboring wall or interface can be precisely controlled in 3D space. This enables studying the dynamics of microbubbles with prescribed, repeatable conditions (5.3).

## 5.1 Introduction

Micron-sized gas bubbles are routinely used as contrast agent in ultrasound medical imaging. They are usually encapsulated by a phospholipid, protein or polymeric shell and contain air or an inert gas. In the ultrasound field, at typical medical imaging frequencies between 1 and 10 MHz, they undergo linear and non-linear oscillation. This acoustical response signature allows discriminating the blood pool from the surrounding tissues [1]. In the past decade, the study of the acoustical response of ultrasound contrast agent (UCA) microbubbles has attracted wide interest, both from the medical and acoustical communities, as non-linear oscillations, complex surface modes and cavitation phenomena are involved in bubble dynamics [2]. The dynamics of UCA microbubbles is commonly recorded acoustically using ultrasound transducers, collecting the backscattering generated from bubble oscillations. More recently, bubble oscillations at ultrasound frequencies were successfully recorded optically [3, 4, 5], with the advantage of providing direct evidence of phenomena involving non-linear oscillations [6], bubble rupture, surface modes and interactions with neighboring objects [7, 8]. Optical recordings of UCA microbubbles dynamics upon insonification require a sampling rate in the million frames per second (Mfps) range, to allow accurate representation of the oscillation period and amplitude. In addition, more than 100 frames are desirable as the ultrasound typically lasts for 10 cycles during which the response of the microbubbles can be highly non-linear, and the number of frames should be sufficient to record the whole process. In this thesis, ultra-high speed imaging is performed using a digital rotating mirror camera, named “Brandaris 128”, capable of 128-frame recordings at 25 Mfps [9]. This instrument has been specifically developed to investigate microbubble dynamics. The microbubbles are traditionally studied by confining them in space either by injection in a soft, acoustically transparent capillary [10] or by producing bubbles in a rising train [11]. A problem common to all experiments on UCA microbubbles is the lack of control on the position and distance from interfaces and neighboring bubbles, due to buoyancy and flow. Even though soft capillaries do not scatter ultrasound, their walls do affect bubble dynamics; in addition, the effect of neighboring bubbles may not be negligible.

Optical tweezers provide an elegant solution for studying UCA microbubble behavior with controlled boundary conditions. As shown in Chapter 4, this technique enables indeed full manipulation of microbubbles, which can be sorted and precisely controlled in 3D space. Recently, optical trapping of UCA microbubbles for the purpose of studying their properties with controlled experimental conditions was demonstrated by various groups [12, 13, 14].

In addition, optical trapping has been combined with different imaging systems, allowing the study of a wide variety of biologically relevant phenomena: optical tweezers were successfully combined with e.g. micro-Raman spectroscopy for resonance Raman studies of single functional trapped cells [15], and with single molecule fluorescence for monitoring biomolecular interactions [16]. The possibility of coupling optical trapping with fluorescence microscopy for probing

single cell mechanics has also been demonstrated [17]. We developed a setup that combines optical trapping with ultra-high speed imaging: UCA microbubbles can be manipulated with Laguerre-Gaussian optical tweezers (see Chapter 4) to obtain desirable boundary conditions, and their dynamics can be optically recorded at up to 25 Mfps using the ultra-high speed camera described in Section 5.2.2. In Section 5.2 the combined setup is presented in full detail.

## 5.2 Methods and apparatus

The setup combines an optical tweezers system based on an upright microscope and a spatial light modulator, with the ultra ultra-high speed camera Brandaris 128 [9]. The camera is directly connected to the output port of the microscope.

### 5.2.1 Optical tweezers setup

The optical tweezers setup is based on the setup described in Chapter 4. The laser beam shaping for generating a Laguerre-Gaussian beam is performed by using phase-only diffractive optical elements (DOEs), implemented on a programmable spatial light modulator (SLM): the DOE is displayed on a liquid crystal display ( $768 \times 768$  pixels) in the front part of the SLM, allowing a refresh rate of up to 60 Hz. The use of computer-generated DOEs enables us to generate arrays of traps, which may contain up to tens of bubbles and/or particles, and the possibility to change the DOE in real-time on the LCD allows dynamically reconfiguring the number, positions and size of traps [16]. The setup for optical trapping (see Figure 5.1) is based on an upright microscope (BXFM, Olympus). The Gaussian beam coming from a 1064 nm continuous wave Yb-doped fiber laser (YLM, IPG Photonics) is converted into a Laguerre-Gaussian mode upon reflection on the SLM (X8267-15, Hamamatsu). The beam is then resized by lenses  $L_1$  and  $L_2$  to fit the objective entrance pupil. These lenses also allow adjusting the convergence of the beam. A dichroic mirror (CVI Laser) reflects the beam into the  $100\times$  microscope objective (LUMPLFL, Olympus;  $NA = 1.00$ , water immersion). The Laguerre-Gaussian beam is then focused into a sample cell containing the microbubbles. Transmission imaging is performed by illuminating the sample either with a metal-halide high-brightness CW light source (ILP-1, Olympus) or with a xenon flash source (MVS-7010, Perkin-Elmer) via a fiber optic cable. Real time imaging is performed through a CCD camera (LCL-902HS, Watec). A beam splitter (BS) transmits 20% of the incident light to the CCD, and reflects the remaining 80% into the high speed camera. Beam shape and position can be monitored on the CCD, while an IR filter (CVI Laser) is inserted in the path of the high speed camera.

### 5.2.2 The “Brandaris 128” camera

The ultra-high speed camera, named Brandaris 128, is a digital rotating mirror camera (Figure 5.2). A rotating three-faced mirror prism directs the incoming

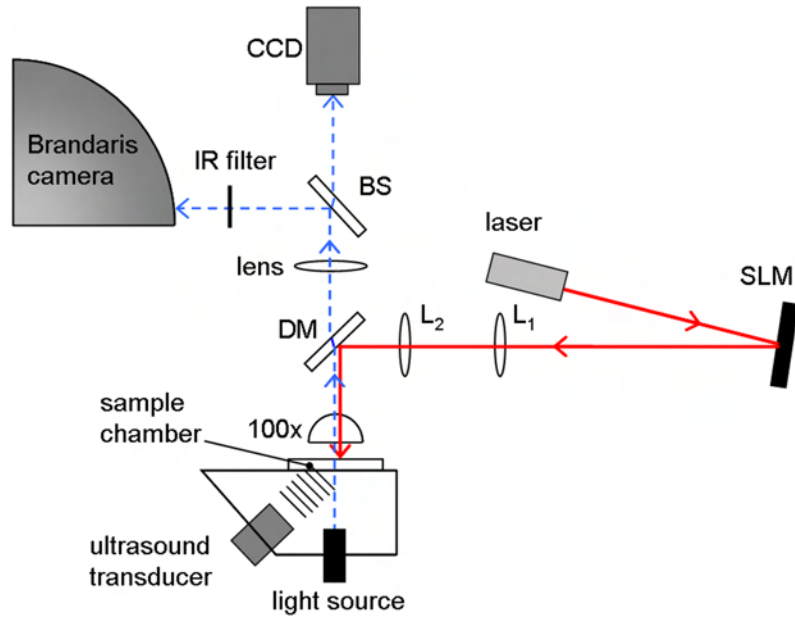


**Figure 5.1** Optical setup for microbubble trapping and ultra-high speed imaging. The laser beam is reflected by the spatial light modulator (SLM) and resized by a telescope (lenses  $L_1$  and  $L_2$ ); it enters the objective ( $100\times$ ) upon reflection on a dichroic mirror (DM) and is focused into the sample volume. Imaging is performed by illuminating the sample in transmission. The image is formed by the microscope tube lens at the primary image plane of the high-speed camera, and on a CCD camera. A beam splitter (BS) enables the two imaging modes. An IR filter blocks any residual IR light coming through the dichroic mirror.

light to 128 optical channels arranged in an arc of 70 degrees. The images are transferred by a bank of small lenses to the image arc, where they are recorded on 128 high sensitivity CCD detectors. The mirror is driven by a pressurized helium flow, controlled by a mass flow controller which keeps the flow, and hence the rotation of the mirror, at a preset speed, corresponding to a given frame rate of the camera. The number of pixels used is  $500 \times 292$ . The optical resolution is determined by the resolving power of the small lenses in the lens bank; in combination with the microscope it can resolve to a scale of 500 nm [9]. The 128 CCDs are controlled by custom-designed electronics. The high rotation speed of the mirror, together with the high sensitivity of the CCD cameras, enables interframe intervals down to 40 ns (25 million frames per second). 128 frames are stored in each recording, and 6 full recordings can be stored consecutively, with a minimum time interval of 40 ms. This instrument has been specifically developed to investigate microbubble dynamics in ultrasound. The camera and its working principle are described in detail in [9].



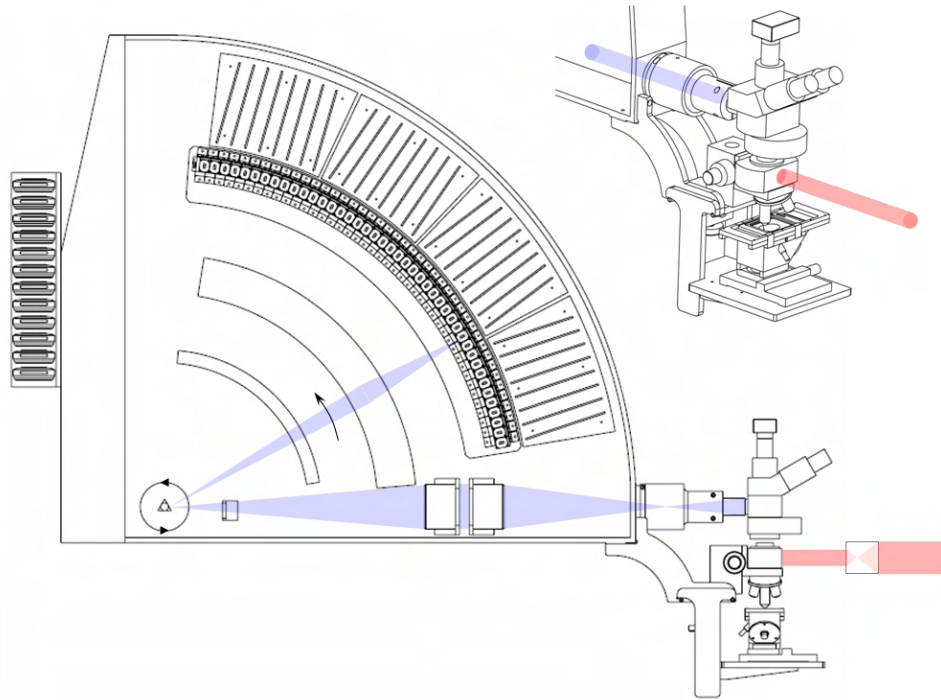


**Figure 5.2** The “Brandaris 128” ultra-high speed camera, coupled to an upright microscope for combined optical trapping and ultra-high speed imaging. The red pathline represents the laser beam, which is resized by a telescope before entering the microscope through the fluorescence port. The blue pathline represents the imaging optical path. The image is focused in the primary image plane of the camera, and transferred by a set of relay lenses to the rotating mirror. The mirror sweeps the image over the 128 CCD sensors arranged in an arc of 70 degrees.

### 5.2.3 Ultrasound setup

A small water container with an unfocused 2.25 MHz transducer (V306, Panametrics Inc.) is mounted on a  $x, y, z$  micropositioning stage located below the objective. The transducer is mounted with  $45^\circ$  incidence angle to the optical axis, so that the acoustical field overlaps the optical focal volume. The transducer is driven using a function generator (33120A, Agilent) in conjunction with an RF power amplifier (350L, ENI). An OptiCell cell culture chamber (BioCrystal, Inc.), which is formed by two polystyrene-matrix material membranes of  $75\ \mu\text{m}$  thickness, positioned at 2 mm spacing, is placed perpendicular to the optical axis into the overlap region. In previous experiments [18], the membranes were observed to exhibit optimum optical and acoustical transmission. The chamber volume (10 ml) is filled with a degassed 0.9% NaCl aqueous solution prior to UCA microbubble injection. A  $100\ \mu\text{l}$  volume of UCA microbubbles is then injected in the chamber. All studies are performed with an experimental contrast agent, BR-14 (Bracco Research S.A., Geneva), which is a phospholipid-stabilized agent com-



**Figure 5.3** Picture of the combined Brandaris camera and optical tweezers setup (Feb 03, 2006)

prising of perfluorobutane-filled microbubbles. The bubble density is optimized to have up to 5-10 bubbles in the field of view of the camera.

#### 5.2.4 Combined optical trapping and ultra-high speed imaging

The setup for optical trapping (Figure 5.1) is very similar to the one described in Section 4.2.1. In that case the trapped bubbles were imaged through a second objective. Here, the imaging and trapping objective need to coincide, since a second objective cannot be easily introduced in the setup. The intrinsic mismatch between trapping and image plane needs to be compensated for. The bubbles are indeed trapped below the focal plane of the objective, at a distance  $z_{trap} \sim 20 - 30 \mu\text{m}$ , where a favorable balance between the scattering force, gradient force and buoyancy arises. The trap position thus needs to be lifted by a distance  $z'$  so that the bubbles are trapped in focus. This can be achieved by causing the beam to enter the objective with a slight convergence. The distance between the lenses  $L_1$  and  $L_2$  can be adjusted to serve this scope.

First, the optical system consisting of lenses  $L_1$  (focal length  $f_1$ ) and  $L_2$  (focal length  $f_2$ ) and microscope objective (focal length  $f_0 = 1.8 \text{ mm}$ ) is considered. The shift  $z'$  is expressed in terms of the distance  $d_{1-2}$  between the lenses using Newton's equation for image formation by thin lenses

$$f^2 = -s s' \quad (5.1)$$

where  $f$  is the focal length of the thin lens,  $s$  is the distance of the object and  $s'$  the distance of the image. We find:

$$z' = \frac{f_0^2}{f_0 - d_{0-2} + f_2 - \frac{f_2^2}{f_1 + f_2 - d_{1-2}}} \quad (5.2)$$

In Figure 5.5  $z'$  is plotted as a function of the distance  $d_{1-2}$  between the lenses, for three different sets of lenses. Two sets of lenses were tested before choosing the

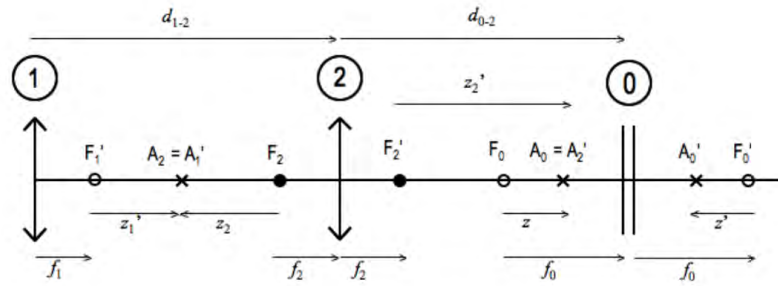


**Figure 5.4** The system of lenses is considered, consisting of lenses  $L_1$  (focal length  $f_1$ ) and  $L_2$  (focal length  $f_2$ ) and microscope objective (focal length  $f_0 = 1.8$  mm). The shift  $z'$  of the focused trap relative to the microscope objective's focal plane, located at  $F_0'$ , depends upon the distance  $d_{1-2}$  between lenses  $L_1$  and  $L_2$ .

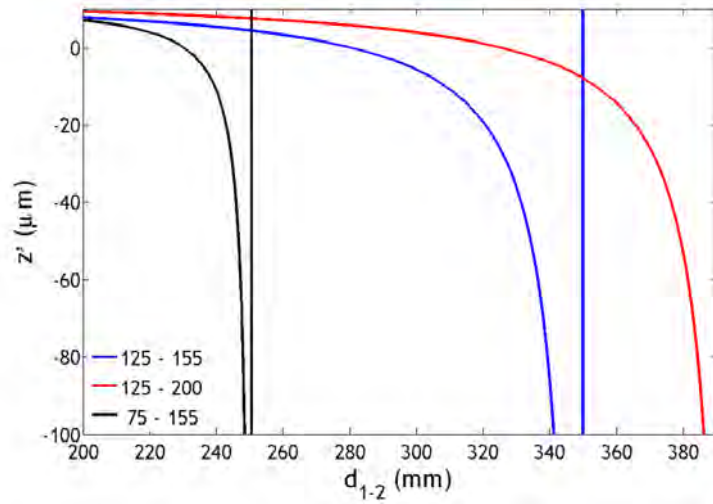


**Figure 5.5** The plots show the calculated shift  $z'$  of the focused trap relative to the microscope objective's focal plane, as a function of the distance  $d_{1-2}$  between lenses  $L_1$  and  $L_2$ .  $z'$  is negative taking the direction of propagation as positive. Different sets of lenses are considered.

combination with  $f_1 = 150$  mm and  $f_2 = 125$  mm, which gave the best control on

the position of the bubble for small displacements of  $L_1$  and small adjustments of the incident laser power.

Initially, the possibility to simply compensate for the image plane position, using relay optics, was also considered. When an object is at a distance  $f_0 + z$  from the objective, its image is produced at a distance  $f_3 - z_3$  (see Figure 5.6) so the image plane is inside the microscope. The easiest is therefore to adjust the trap position.

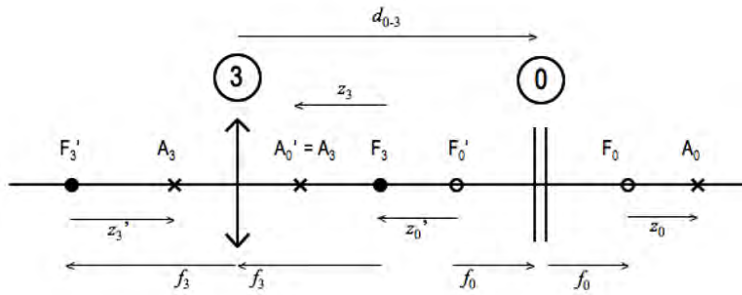


**Figure 5.6** The system of lenses is considered, consisting of the microscope tube lens  $L_3$  and the microscope objective. The image of an object placed in  $A_0$  is formed in  $A_3$ . It is thus inside the microscope in our setup.

## 5.3 Results

The setup combining optical tweezers and ultra-high speed imaging, enables for a characterization of the boundary-dependent UCA microbubble dynamics at the single-bubble level. We are able to compare the behavior of the very same UCA microbubble under different boundary conditions, by a well-controlled positioning of individual bubbles. The laser is blocked during the recording to avoid interfering optical forces, but short enough for the bubble to remain in the trapped position. More experiments can thus be repeated on the same bubble, as it is always found back in the trap after the laser is retransmitted. For analysis and comparison with theoretical models, the movies are processed to track the bubble radius as a function of time, resulting in a so-called *radius-time curve* of the bubble,  $R - t$ . An FFT algorithm is applied to the  $R - t$  curve to compute its Fourier transform. The square of this quantity gives the power spectrum  $P_R$  of the radius-time curve.

### 5.3.1 Recordings of freely oscillating microbubbles

An individual UCA microbubble can be selected and trapped. It can be subsequently positioned at a prescribed distance from the chamber wall, by moving the chamber upwards with  $\mu\text{m}$  precision, using a micropositioning stage. The dynamics of a freely oscillating microbubble can thus be investigated. A sequence is shown in Figure 5.7, where an individual bubble oscillates at  $50 \mu\text{m}$  from the sample chamber wall. The insonifying ultrasound wave consists of a burst of 8 cycles, the first and the last of which are modulated by a Gaussian envelope. The applied acoustic pressure  $P_{AC}$  is 150 kPa (peak negative pressure, PNP) at a frequency of 2.25 MHz. The acquisition frame rate is 15 Mfps, corresponding to a temporal resolution of about 65 ns. Figure 5.8 shows the results of the image processing: the experimental  $R - t$  curve is obtained, and from it the power spectrum is calculated.

### 5.3.2 Influence of the laser trap on bubble dynamics

The possible influence of the laser trap was also investigated by recording the same bubble free from the trap and inside the trap with the laser beam switched on. No apparent influence on the frequency or amplitude of the oscillations was observed (see Figure 5.9) in 12 repeated experiments carried out at 2.25 MHz with an applied pressure of 150 – 200 kPa. As a consequence, experiments requiring longer acquisition times than those described here can also be performed, as the laser needs not to be switched off during the recording, thus providing the necessary 3D confinement for the bubble not to go out of focus due to buoyancy. It is also noteworthy that laser absorption by the particle is negligible in this trapping configuration, as it is confined in the region of minimum intensity, and thermal damage of contrast bubbles does not occur.

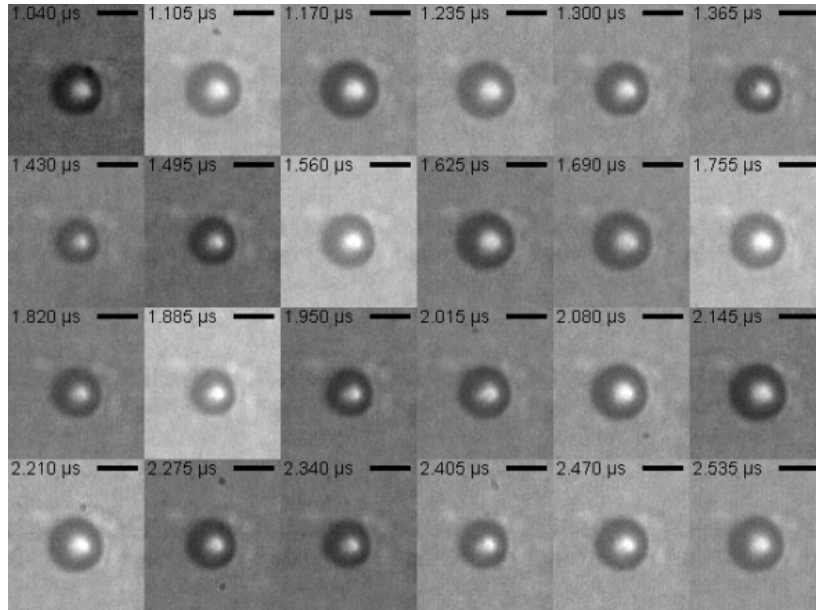


**Figure 5.7** Microbubble freely oscillating at 2.25 MHz recorded at 15 Mfps, after release from the optical trap. In figure, 24 of the 128 frames are shown; each frame is recorded by a different CCD. The interframe time is 65 ns. Scalebar  $2\ \mu\text{m}$ .

## 5.4 Conclusions

A setup was described that allows time-resolved optical monitoring of ultrasound contrast agent microbubble dynamics under ultrasound, with controlled boundary conditions. A digital rotating mirror high-speed camera allows achieving the temporal resolution required for investigating the oscillation dynamics in the sub- $\mu\text{s}$  timescale. Coupling of this instrument to an optical tweezers setup allowed manipulation of microbubbles, so that controlled boundary conditions for the oscillating bubbles can be achieved. We therefore introduced a powerful tool for investigating how the bubble dynamics, hence the acoustical signature, changes with varying distance to neighboring objects. The results of the experiments performed with this setup will be the subject of Chapter 6.

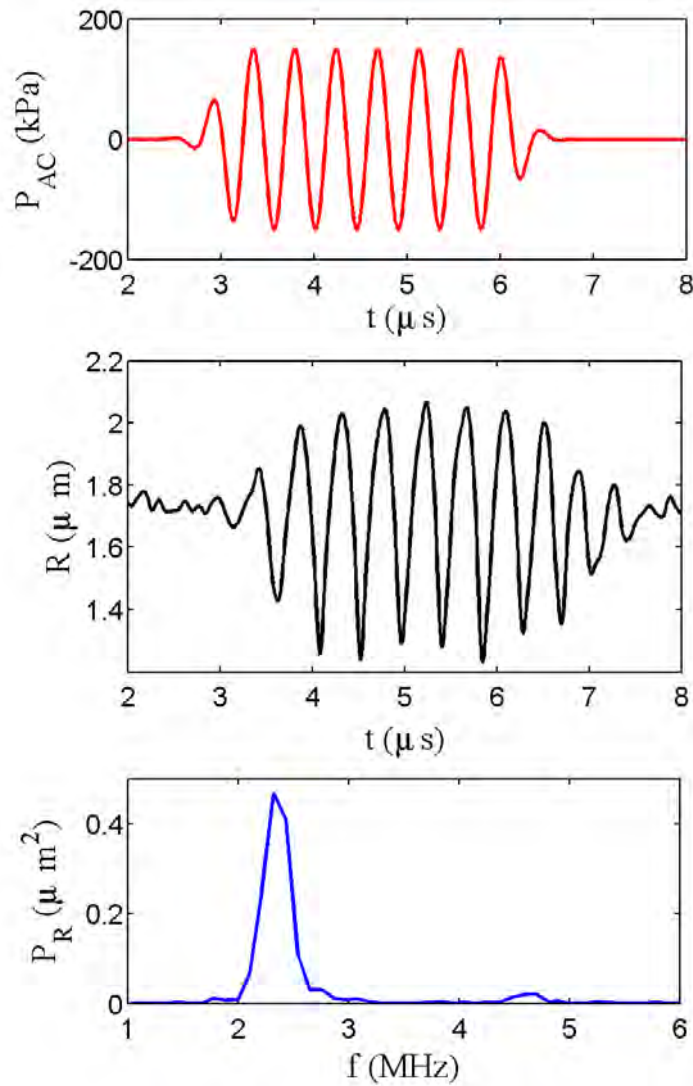


**Figure 5.8** Bubble radius oscillations upon insonification. Red curve: applied acoustic pressure  $P_{AC}$  (ultrasound burst of 8 cycles at a frequency of 2.25 MHz, with Gaussian envelope on first and last cycle, PNP 150 kPa). Black curve: the  $R - t$  curve is obtained by image processing from the recorded 128-frame movie. In the plot 112 of the 128 data points are shown. Blue curve: power spectrum of the bubble oscillations. The linear response is remarkably pronounced (peak at 2.25 MHz) compared to the non-linear contribution (peak at 4.5 MHz, second harmonics).

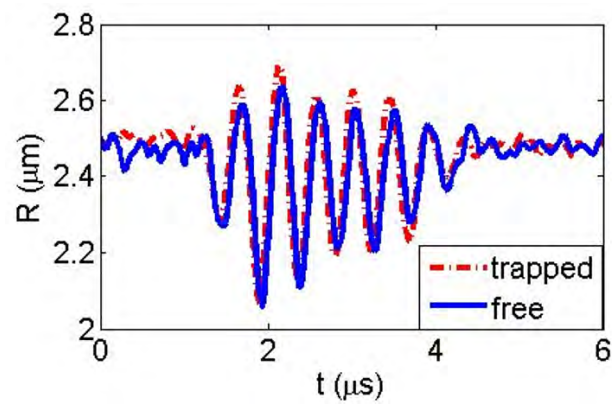


**Figure 5.9** The dynamics of the very same, single  $2.5 \mu\text{m}$  bubble is recorded with the bubble trapped in the LG beam (red dashed line) and after the bubble is released from the optical trap (blue solid line). The applied pressure amplitude is 150 kPa with a frequency of 2.25 MHz. In repeated experiments on different bubbles, no significant difference is observed in the amplitude or frequency of oscillation.



## Bibliography

- [1] J. Raichlen B.B. Goldberg and F. Forsberg. *Ultrasound Contrast Agents: Basic Principles and Clinical Applications, 2nd ed.* London: Dunitz, 2001.
- [2] N. de Jong, A. Bouakaz and P. Frinking. Basic acoustic properties of microbubbles. *Echocardiography*, 19:229–240, 2002.
- [3] J. Chomas, P. Dayton, D. May, J. Allen, A. Klibanov and K. Ferrara. Optical observation of contrast agent destruction. *Appl. Phys. Lett.*, 77:1056–1058, 2000.
- [4] N. de Jong, P. Frinking, A. Bouakaz, M. Goorden, T. Schourmans, X. Jingping and F. Mastik. Optical imaging of contrast agent microbubbles in an ultrasound field with a 100-mhz camera. *Ultrasound Med. Biol.*, 26:487–492, 2000.
- [5] N. Kudo, T. Miyaoka, K. Kuribayashi and K. Yamamoto. Study of the mechanism of fragmentation of a microbubble exposed to ultrasound using a high-speed observation system. *J. Acoust. Soc. Am.*, 108:2547, 2000.
- [6] P. Marmottant, S.M. van der Meer, M. Emmer, M. Versluis, N. de Jong, S. Hilgenfeldt and D. Lohse. A model for large amplitude oscillations of coated bubbles accounting for buckling and rupture. *J. Acoust. Soc. Am.*, 118:3499–3505, 2005.
- [7] K. Tachibana, T. Uchida, K. Ogawa, N. Yamashita and K. Tamura. Induction of cell-membrane porosity by ultrasound. *Lancet*, 353:1409, 1999.
- [8] P. Marmottant and S. Hilgenfeldt. Controlled vesicle deformation and lysis by single oscillating bubble. *Nature*, 243:153–156, 2003.
- [9] C.T. Chin, C. Lancée, J. Borsboom, F. Mastik, M.E. Frijlink, N. de Jong, M. Versluis and D. Lohse. Brandaris 128: A digital 25 million frames per second camera with 128 highly sensitive frames. *Rev. Sci. Instr.*, 74:1–9, 2003.
- [10] A. Bouakaz, M. Versluis and N. De Jong. High-speed optical observations of contrast agent destruction. *Ultrasound Med. Biol.*, 3:391–399, 2005.
- [11] P. Palanchon, P. Tortoli, A. Bouakaz, M. Versluis and N. De Jong. Optical observations of acoustical radiation force effects on individual air bubbles. *IEEE Trans. Ultrasound Ferroel. Freq. Control*, 52:104–110, 2005.
- [12] P.A. Prentice, M.P. MacDonald, T.G. Frank, A. Cuschieri, G.C. Spalding, W. Sibbett, P.A. Campbell, K. Dholakia. Manipulation and filtration of low index particles with holographic Laguerre-Gaussian optical trap arrays. *Opt. Exp.*, 12:593–600, 2004.

- [13] V. Garbin, D. Cojoc, E. Ferrari, R. Kulkarni, and E. Di Fabrizio. Manipulation of single and multiple low-index particles by means of optical tweezers. In *Proc. SPIE Vol. 5930*, pages 492–501, 2005.
- [14] P.H. Jones, E. Stride and N. Saffari. Trapping and manipulation of microscopic bubbles with a scanning optical tweezer. *Appl. Phys. Lett.*, 89:081113, 2006.
- [15] K. Ramser, K. Logg, M. Gosko, J. Enger, M. Kall and D. Hanstorp. Resonance Raman spectroscopy of optically trapped functional erythrocytes. *J. Biomed. Opt.*, 9:593–600, 2004.
- [16] M.J. Lang, P.M. Fordyce, A.M. Engh, K.C., and S.M. Block. Simultaneous, coincident optical trapping and single molecule fluorescence. *Nature Methods*, 1:1–7, 2004.
- [17] V. Emiliani, D. Cojoc, E. Ferrari, V. Garbin, C. Durieux, M. Coppey-Moisan, and E. Di Fabrizio. Wave front engineering for microscopy of living cells. *Opt. Exp.*, 13:1395–1405, 2005.
- [18] A. van Wamel, A. Bouakaz, M. Versluis and N. de Jong. Micromanipulation of endothelial cells: Ultrasound-microbubble-cell interaction. *Ultrasound in Med. Biol.*, 30:1255–1258, 2004.

## Chapter 6

# 3D optical manipulation of microbubbles: bubble-wall and bubble-bubble interactions

The first experiments performed with the setup which combines 3D optical micro-manipulation and ultra-high speed imaging of UCA microbubbles are presented here. The influence of a neighboring object (a rigid interface or a second bubble) on the bubble dynamics is studied with well-controlled and repeatable conditions. In our experiments we compare the behavior of the very same bubble under different boundaries. The experimental results are compared to a Rayleigh-Plesset-like model for the single-bubble case. For a precise quantification of the force balance in the two-bubble case, the translation dynamics is also modeled. A recent model accounting for the shell properties is used to extend the model for uncoated bubbles. The importance of this investigation for molecular imaging applications is presented in 6.1. Bubble phenomena are shortly described from a theoretical standpoint in 6.2. Experimental results showing changes in the dynamics of one and the same UCA microbubble near a boundary are presented and discussed in 6.3.

## 6.1 Introduction

### 6.1.1 UCA microbubbles

Ultrasound contrast agents increase the echo from the blood pool in ultrasound diagnostic imaging, and allow the delineation of blood vessels [1]. Microbubbles are widely used as ultrasound contrast agents in clinical use and research. These agents consist of a gaseous center stabilized by an outer shell. The shell prevents

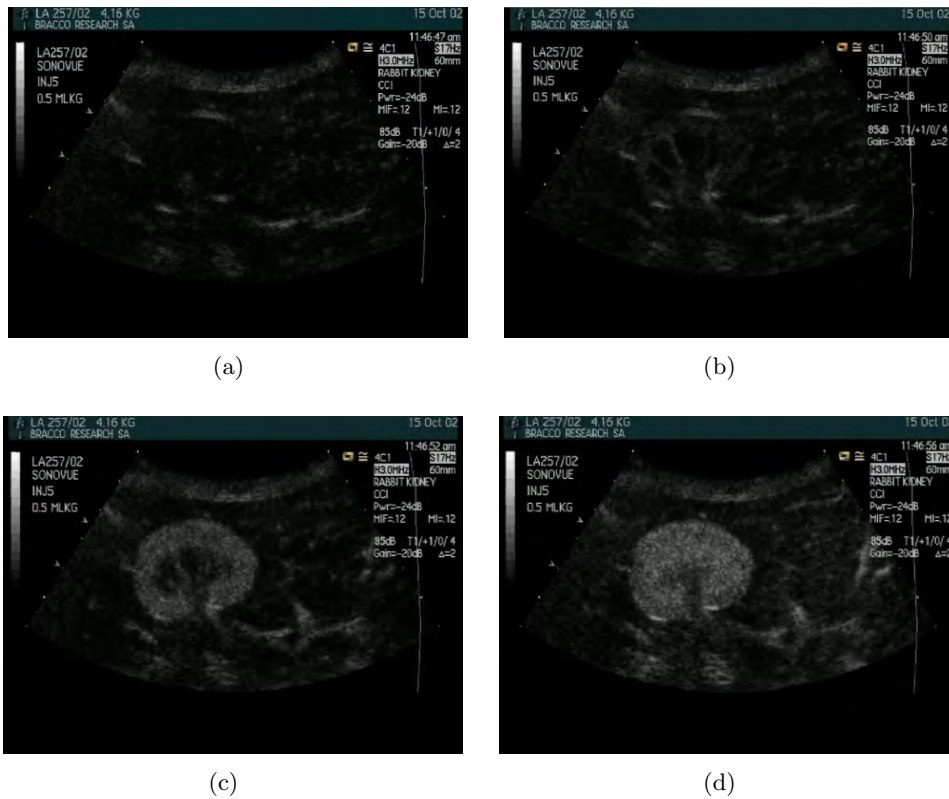


**Figure 6.1** Ultrasound image of a rabbit kidney before (a) and after (b, c, d) injection of UCA microbubbles. The perfusion to the kidney is visualized when bubbles circulate in the vasculature. Courtesy of: Bracco Research S.A. (Geneva).

the core gas from rapidly dissolving in the surrounding medium. Gas dissolution for these bubbles is driven by surface tension  $\sigma_0$  of the gas-water interface, which generates a Laplace pressure  $\frac{2\sigma_0}{R}$  inside the bubble, therefore smaller bubbles lose gas and disappear faster. Coated bubble preparations have the ability to pass through the lungs and successfully recirculate in the bloodstream. The shell can be made from denatured protein (e.g. human serum albumin), polymer, or a phospholipid monolayer. However, a thin shell is not sufficient to prevent gas diffusion, therefore a poorly soluble gas is used to achieve sufficient circulation time. In typical clinical use, a small amount (microliters to milliliters) of prepared contrast agent solution is injected intravenously during an ultrasonic examination,

and the microbubbles travel through the circulation enhancing the echo signal from the blood pool.

### 6.1.2 Interaction of UCA microbubbles with ultrasound

When a gas bubble is insonified by a US wave, it generates two kinds of responses. First, the wave will be reflected at the surface of the bubble because of the large difference in acoustic impedance between the surrounding medium and the gas inside the bubble. More importantly, however, when the bubble size is much smaller than the wavelength of the US wave, it is forced into volume pulsation (for a 3-MHz US wave, the wavelength in water is 0.5 mm). The volume pulsation of the bubble is frequency-dependent and shows a clear maximum at a specific frequency, which is referred to as the resonance frequency, and is inversely related to the bubble size (see Section 6.8). The resonance phenomenon is an important effect because a resonating bubble yields an enhancement of the backscatter signal. The response of a gas bubble to a US wave depends on the acoustic pressure amplitude [2]. For small amplitudes of the US wave, the relative compression and expansion of the bubble is the same and, therefore, the bubble size is linearly related to the applied acoustic pressure. For higher amplitudes, however, the compression and expansion curves are different and nonlinearity occurs. Consequently, the bubble size is not linearly related to the applied acoustic pressure [3], and the bubble vibration contains second and higher multiples of the transmitted frequency. In this way, the backscatter signal from the bubble not only contains the fundamental (transmitted) frequency, but also harmonic frequencies, most notably at twice the fundamental frequency. This effect is not shown so markedly by tissue and it, therefore, offers the possibility of separating the response of the bubble from that of the surrounding tissue. Important applications to diagnostic imaging include the quantification of organ perfusion (see Figure 6.1), or the visualization of angiogenesis.

### 6.1.3 Experimental characterization of UCA microbubble dynamics

Many aspects of the dynamics of UCA microbubbles still remain elusive, and this has attracted in the past two decades the interest of both the medical and acoustical communities, as non-linear oscillations, complex surface modes, cavitation phenomena and mutual interactions between bubbles occur [4]. A precise, quantitative understanding of such bubble phenomena may find direct applications in diagnostic ultrasound, as it would allow to further develop bubble technology on one hand, and to improve the imaging protocols on the other hand. Furthermore, lively interest in the study of UCA microbubble oscillations in the vicinity of a wall has been raised by their use for sonoporation [5, 6] and molecular imaging [7]. For molecular imaging applications, it will be crucial to develop methods for selectively detecting adherent UCA microbubbles that have bound to specific molecular targets from freely flowing ones, primarily based on a change in their acoustic response. Considerable differences in the amplitude of oscillations [8, 9]

and in the spectral response [10] were reported recently. In general, however, the studies on UCA microbubble dynamics suffer from the lack of control on bubble position, due to buoyancy and bubble clustering, and they are therefore based on ensemble averaging and statistical observations of many different bubbles.

The use of optical tweezers for 3D micromanipulation and positioning of UCA microbubbles was presented in Chapter 4, and the setup combining optical trapping capabilities to ultra-high speed imaging, for time-resolved optical recordings of bubble dynamics was described in Chapter 5. Here we show how the dynamics of one and the same UCA microbubble changes under different boundary conditions, namely in the vicinity of a wall or in close proximity to a second bubble, by controlling the position of individual microbubbles with optical tweezers and recording their dynamics at 15 million frames per second.

## 6.2 Theory

In this Section a model is presented for the dynamics of UCA microbubbles in ultrasound. For simplicity the dynamics is first described in the case of an uncoated bubble. The effect of a coating is then included.

### 6.2.1 Radial dynamics of a free gas bubble

To examine the dynamics in ultrasound of gas microbubbles, the model developed in 1917 by Lord Rayleigh for collapsing voids in water is used as the theoretical basis. The response of a spherical bubble to an external, time-varying pressure field in a boundless, inviscid incompressible fluid obeys [11]:

$$\rho(R\ddot{R} + \frac{3}{2}\dot{R}^2) = P_g - P_l \quad (6.1)$$

where  $R = R(t)$  is the instantaneous bubble radius,  $\rho$  is the density of the surrounding liquid,  $P_l$  is the pressure in the liquid, and  $P_g$  is the gas pressure inside the bubble. The bubble is assumed to remain spherical at all times, therefore it is characterized simply by its radius  $R(t)$ . The acoustic wavelength is much larger than  $R$ , the density of the liquid  $\rho$  is large compared to the gas density, and the gas pressure inside the bubble is uniform. Also, the vapor pressure is assumed to be constant during the oscillations. The pressure in the liquid writes  $P_l = P_0 + P_{AC}(t)$ ,  $P_0$  being the hydrostatic pressure and  $P_{AC}(t)$  the externally applied acoustic pressure. An extension of Equation 6.1 leads to what is now called the *Rayleigh-Plesset equation* [12, 13], a model for many important bubble phenomena. This includes the effect of surface tension, through the Laplace capillary pressure term  $2\sigma_0/R$ , and the effect of viscosity, which gives an effective pressure  $4\mu\dot{R}/R$ , yielding:

$$\rho(R\ddot{R} + \frac{3}{2}\dot{R}^2) = P_g - P_0 - P_{AC}(t) - 2\frac{\sigma_0}{R} - 4\mu\frac{\dot{R}}{R} \quad (6.2)$$

where  $\sigma_0$  denotes the surface tension of the liquid/gas interface, and  $\mu$  denotes the liquid viscosity.

To account for the gas pressure inside the bubble an ideal polytropic gas law can be chosen,  $P_g \propto R^{-3\kappa}$ , with  $\kappa$  as the polytropic gas exponent. It is 1 for bubbles behaving isothermally, and equal to the ratio of specific heats (close to 1.07 for  $C_4F_{10}$ ) for bubbles behaving adiabatically [14]. When the thermal diffusion length in the gas during a period is small compared to the radius, the adiabatic version is used. The Keller-Miksis equation [15], a modified version of the Rayleigh-Plesset equation which describes large amplitude oscillations by incorporating the effects of acoustic radiation by the bubble, in the approximation of a linear polytropic exponent, gives for a free gas bubble with resting radius  $R_0$ :

$$\rho \left( R\ddot{R} + \frac{3}{2}\dot{R}^2 \right) = \left( P_0 + \frac{2\sigma_0}{R_0} \right) \left( \frac{R}{R_0} \right)^{-3\kappa} \left( 1 - \frac{3\kappa\dot{R}}{c} \right) - P_0 - P_{AC}(t) - \frac{2\sigma_0}{R} - 4\mu\frac{\dot{R}}{R} \quad (6.3)$$

This highly nonlinear equation can be solved numerically to predict the radial dynamics of non-encapsulated gas bubbles. Thermal damping is neglected.

### 6.2.2 Sound radiation

In an incompressible fluid, the pressure gradient is related to the fluid velocity by Euler's equation. The sound radiated by an oscillating bubble at a distance  $r \gg R_0$  from the bubble is given by [11]:

$$P_s(r, t) = -\rho \frac{\partial}{\partial t} \left( \frac{R^2 \dot{R}}{r} \right) = \rho \frac{2R\dot{R}^2 + R^2 \ddot{R}}{r} \quad (6.4)$$

The radius  $R$  of a UCA microbubble is  $\sim 2 \mu\text{m}$ . For a typical radial excursion of  $0.2 \mu\text{m}$  at a frequency of 2 MHz, the velocity of the wall is therefore of the order of  $1 \text{ ms}^{-1}$ . The corresponding acceleration of the bubble wall is  $\sim 2 \times 10^6 \text{ ms}^{-2}$ . The sound radiation is inversely proportional to the distance; at  $r = 10 \mu\text{m}$  (typical distance from a neighboring bubble) the magnitude of the radiated pressure is 1 kPa, and at  $r = 1 \text{ cm}$  (typical distance from the transducer) it decays to  $10^{-3}$  kPa.

### 6.2.3 The microbubble as a forced linear oscillator

The bubble approximates to a linear oscillator when driven at low amplitude [11, 16]. The oscillator mass is provided by the fluid surrounding the bubble, and the elastic restoring force by the internal energy stored in the bubble gas. Letting the radius be  $R = R_0(1 + x)$ , where  $x$  is a small perturbation, gives:

$$\ddot{x} + \omega_0 \delta \dot{x} + \omega_0^2 x = F(t) \quad (6.5)$$

with  $f_0 = \omega_0/2\pi$  the eigenfrequency of the system and  $\delta$  the linear dimensionless damping coefficient.  $F(t)$  is the time-dependent forcing term, e.g.  $F(t) = F_0 \sin \omega t$ . The amplitude of the radial variation of the bubble depends on the driving frequency  $f = \frac{\omega}{2\pi}$ . Writing  $x(t) = x_0 \sin(\omega t + \phi)$  one gets from Equation 6.5:

$$x_0(\omega) = \frac{F_0}{\sqrt{(\omega_0^2 - \omega^2)^2 + (\delta\omega\omega_0)^2}} \quad (6.6)$$

This equation defines the resonance curve, displaying a maximum at the resonance frequency:

$$f_{res} = f_0 \sqrt{1 - \frac{\delta^2}{2}} \quad (6.7)$$

which is lower than the eigenfrequency in the presence of damping. The damping mechanisms for an uncoated bubble are the re-radiation of sound by the oscillating bubble and viscosity, both of which are accounted for in Equation 6.3, and thermal damping:  $\delta = \delta_{rad} + \delta_{vis} + \delta_{therm}$ . Here, thermal damping is neglected.

For a mass-spring system, when  $\omega \ll \omega_0$  the driving force and the oscillator displacements are in phase (*stiffness controlled*) and at  $\omega \gg \omega_0$  (*inertia controlled*) they are in antiphase. Similarly, the bubbles oscillate in phase or in anti-phase with the driving pressure, depending on whether the frequency of the incoming wave is smaller or larger than their resonance frequency.

#### 6.2.4 Resonance frequency

Linearization of Equation 6.3 yields the eigenfrequency as a function of the bubble resting radius  $R_0$ :

$$f_0 = \frac{1}{2\pi} \sqrt{\frac{1}{\rho R_0^2} \left( 3\kappa P_0 + \frac{2(3\kappa - 1)\sigma_0}{R_0} \right)} \quad (6.8)$$

Neglecting the surface tension in Equation 6.8 gives the Minnaert frequency [17]. For a given insonation frequency, a resonant radius can therefore be defined, for which the insonation frequency corresponds to the resonance frequency.

#### 6.2.5 Dynamics of a bubble near a rigid wall

The behavior of oscillating bubbles close to a rigid wall is of great practical interest, and it has been studied extensively both in theory and experiments [18, 19, 20, 21, 22]. The model presented here is very simple, but still it contains some remarkable features of the bubble-wall system. The flow field near a wall can be modeled, in a first approximation, by replacing the wall with an *acoustic image* located symmetrically on the other side of the wall, in order to satisfy a vanishing normal velocity at the wall [11]. This can be accounted for by simply including the sound radiation of the image bubble in Equation 6.3. The image bubble has the same radius  $R(t)$  of the oscillating bubble at all times, and we assume that the bubble remains spherical. We use the far-field approximation



for the sound radiated by the image bubble, see Equation 6.4, although this is clearly not the case for a bubble in contact with the wall. The equation of motion of the bubble wall then writes:

$$\rho\left(R\ddot{R} + \frac{3}{2}\dot{R}^2\right) = \left(P_0 + \frac{2\sigma_0}{R_0}\right)\left(\frac{R}{R_0}\right)^{-3\kappa}\left(1 - \frac{3\kappa\dot{R}}{c}\right) + \quad (6.9)$$

$$- P_0 - P_{AC}(t) - \frac{2\sigma_0}{R} - 4\mu\frac{\dot{R}}{R} - \rho\frac{\partial}{\partial t}\left(\frac{R^2\dot{R}}{r}\right)$$

where  $r$  is the center-to-center distance between the bubbles. For a bubble in contact with the wall  $r = 2R$  and the equation becomes:

$$\rho\left(\frac{3}{2}R\ddot{R} + 2\dot{R}^2\right) = \left(P_0 + \frac{2\sigma_0}{R_0}\right)\left(\frac{R}{R_0}\right)^{-3\kappa}\left(1 - \frac{3\kappa\dot{R}}{c}\right) + \quad (6.10)$$

$$- P_0 - P_{AC}(t) - \frac{2\sigma_0}{R} - 4\mu\frac{\dot{R}}{R}$$

Linearizing to a harmonic oscillator, the mass at the wall is increased by a factor  $\frac{3}{2}$  (increased pre-factor of  $\ddot{R}$ ) and this results in a decrease of the natural frequency by a factor  $\sqrt{\frac{2}{3}}$ . A resonance frequency shift for non-spherical bubbles was predicted using this simple approach by Strasberg in 1953 [23]. Figure 6.2 shows the resonance frequency curves predicted by the image bubble model for an uncoated bubble with resting radius  $R_0 = 1.5 \mu\text{m}$ . The blue solid line is for the bubble in free space, the red dashed line for the bubble in contact with the wall. Besides a decrease in the resonance frequency, this model also predicts a larger amplitude of the resonance curve for the bubble at the wall. We anticipate that this is not observed in experiments (see Section 6.3.2), as the model does not account for important dissipation effects occurring in the viscous boundary layer at the wall.

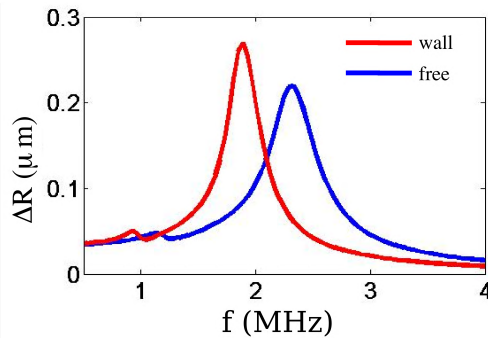


**Figure 6.2** Resonance frequency curves predicted by the image bubble model for an uncoated bubble with resting radius  $R_0 = 1.5 \mu\text{m}$ . The blue solid line is for the bubble in free space, the red dashed line for the bubble in contact with the wall. From [24].

### 6.2.6 Acoustic radiation pressure

A pulsating bubble, driven by a sound field, absorbs and scatters the incident acoustic wave. Absorption of the momentum associated with the incoming wave gives rise to a *radiation pressure*. A body of volume  $V$  in a pressure gradient  $\nabla p$  experiences a force [11]:

$$F_B = -V\nabla p \quad (6.11)$$

The radiation force on a bubble in a standing-wave field is termed *primary Bjerknes force*. In a standing-wave field, the pressure gradient oscillates. As discussed in Section 6.2.3, a bubble of less than resonant size oscillates in-phase with the sound field, and a bubble larger than resonance oscillates  $\pi$  out of phase with the field. When the bubble and the field are oscillating in phase, the bubble volume is minimum when the pressure is maximum, and viceversa if the two are oscillating out of phase. Therefore the quantity  $-\langle V\nabla p \rangle$  will be in one direction for bubbles below resonance and in the opposite direction for bubbles above resonance. Therefore, in a standing wave field, bubbles of less than resonant size travel up a pressure gradient towards the pressure antinodes, and those larger than resonance travel down the gradient to the node.

The pressure field radiated by one pulsating bubble (see Section 6.2.2) also generates radiation forces on neighboring bubbles. The radiation force exerted on one pulsating bubble by the sound field emitted by another is termed *secondary* (or *mutual*) *Bjerknes force*. The mutual force between two pulsating gas bubbles in a liquid was first studied by V. F. K. Bjerknes (1906) and C. A. Bjerknes (1915). They observed that this mutual force, caused the bubbles to either attract or repel each other depending upon whether the bubble pulsations were in phase or out of phase, respectively. In particular, when the frequency of an applied acoustic field was greater than or less than the natural oscillation frequencies of both bubbles, then the bubbles were found to oscillate in phase and attract, whereas if the driving frequency was in between the two natural frequencies, the bubbles would oscillate out of phase and repel each other. Note that the instantaneous secondary Bjerknes force is alternatively attractive and repulsive. Averaging over time, however, if the two bubbles oscillate in phase (out of phase) they will experience a net attractive (repulsive) secondary Bjerknes force.

### 6.2.7 Dynamics of a bubble pair

We adapt the model presented by Harkin *et al.* [25], which is derived in the context of potential flow theory up to the 4<sup>th</sup> order in the inverse separation distance between the bubbles, and gives the equations of motion for a bubble pair in oscillation and translation, in the case  $R_1 \neq R_2$ .

The force balance which gives the translation equations of the bubble centers is shortly discussed here. Considering the forces acting along the direction of the line of centers  $z$ , the bubbles experience the following inertial force components: the added mass force, due to the acceleration of the fluid, and the secondary Bjerknes acoustic force. Dissipative forces are the translation drag force and

the expansion drag force which is caused by the oscillations of the other bubble. Magnaudet and Legendre [26] showed that when at least one of the translation and radial Reynolds numbers is large, a high-Reynolds number formalism for the drag force can be safely used. When both Reynolds numbers are small, then a history force term needs to be included. For our system the translational velocity  $u_t$  is  $\sim 1 \text{ ms}^{-1}$ , as is the radial velocity  $u_r$ . Typical bubble radii are  $\sim 2 \mu\text{m}$ . Therefore, both the translation Reynolds number  $Re_t = R u_t / \nu$  and the radial Reynolds number  $Re_r = R u_r / \nu$  are not in the small number range. However, we are in an intermediate region where low Reynolds numbers effects may play a role.

Within these approximations, we linearize the set of equations for the radial and translation dynamics derived by Harkin *et al.* [25]. Let  $R_1(t)$ ,  $R_2(t)$  be the bubble radii, and  $z_1(t)$ ,  $z_2(t)$  their positions along the direction of the line of centers. Linearization yields the following set of equations:

$$R_i \ddot{R}_i + \frac{3}{2} \dot{R}_i^2 = \frac{1}{\rho} \left( P_{gas}(R_i) - 4\mu \frac{\dot{R}_i}{R_i} - \frac{2\sigma_0}{R_i} - P_0 - P_{AC}(t) \right) + \frac{\dot{z}_i^2}{4} - \frac{2R_j \dot{R}_j^2 + R_j^2 \ddot{R}_j}{|z_2 - z_1|} \quad (6.12)$$

for the radial motion ( $i, j = 1, 2$  with  $i \neq j$ ), where

$$P_{gas}(R_i) = \left( P_0 + \frac{2\sigma_0}{R_{i,0}} \right) \left( \frac{R_i}{R_{i,0}} \right)^{-3\kappa} \left( 1 - 3\kappa \frac{\dot{R}_i}{c} \right) \quad (6.13)$$

The second term on the right-hand side of Equation 6.12 accounts for the effect of the bubble translation on the oscillations, and the third term is the pressure radiated by the other bubble. For the translation the two equations of motion write:

$$\ddot{z}_1 = -3 \frac{R_2^2 \ddot{R}_2 + 2R_2 \dot{R}_2^2}{(z_2 - z_1)^2} - 18\nu \frac{\dot{z}_1}{R_1^2} - 3 \frac{\dot{R}_1 \dot{z}_1}{R_1} \quad (6.14)$$

$$\ddot{z}_2 = 3 \frac{R_1^2 \ddot{R}_1 + 2R_1 \dot{R}_1^2}{(z_2 - z_1)^2} - 18\nu \frac{\dot{z}_2}{R_2^2} - 3 \frac{\dot{R}_2 \dot{z}_2}{R_2} \quad (6.15)$$

The first term on the right-hand side is the secondary Bjerknes force, the second term is the viscous drag force and the third term is the added mass force of a bubble with time-varying radius [27]. The expansion drag force is a higher order term and it is here neglected.

### 6.2.8 Dynamics of a coated bubble

The model presented by Marmottant *et al.* [28] accounting for the UCA microbubble coating is shortly presented here. The coating modifies the effective surface tension. We focus on phospholipid monolayer coatings, used in several contrast agent bubbles, including the agent BR-14 (Bracco Research S.A.,

Geneva) used throughout this investigation. The phospholipid molecules naturally adsorb to the interface and shield the water from the air, reducing the surface tension to a value lower than that of pure water (0.072 N/m). The compression of the monolayer decreases the area available per molecule. When this area reaches that covered by the lipid molecules, the effective surface tension decreases sharply. The variation of surface tension with the area  $A = 4\pi R^2$  is expressed with the *elastic compression modulus* defined by  $\chi = A(d\sigma/dA)$ , of order 0.2 N/m for a slow compression [28]. Further compression leads to an unstable situation where the monolayer buckles and the surface tension nearly vanishes. In contrast, a slow expansion separates molecules from each other: surface tension rises. For small vibration amplitudes,  $|R - R_0| \ll R_0$ , the lipid monolayer behaves as if composed of a thin solid and elastic material. The surface tension can be linearized around a constant value:

$$\sigma(R) = \sigma(R_0) + \chi \left( \frac{R^2}{R_0^2} - 1 \right) \simeq \sigma(R_0) + 2\chi \left( \frac{R}{R_0} - 1 \right) \quad (6.16)$$

The shell is elastic only in a narrow area range. The lower limit is given by buckling, the upper limit by the maximum surface tension,  $\sigma_{water}$ , before rupture of the shell. During the oscillation, the balance of normal stresses at the interface is:

$$P_g(t) - P_l(t) = \frac{2\sigma(R)}{R} + 4\mu \frac{\dot{R}}{R} + 4\kappa_s \frac{\dot{R}}{R^2} \quad (6.17)$$

with  $P_g$  the gas pressure in the bubble,  $P_l$  the the liquid pressure,  $\mu$  the surrounding liquid viscosity, and  $\kappa_s$  the *surface dilatational viscosity* from the monolayer. The second term on the right-hand side is the stress arising from the frictions in the liquid and the third from frictions in the shell [29]. In this model  $\kappa_s$  does not depend on the surface area. Combining Equation 6.3 with the boundary condition 6.17 we obtain the model for the bubble dynamics

$$\begin{aligned} \rho \left( R\ddot{R} + \frac{3}{2}\dot{R}^2 \right) &= \left( P_0 + \frac{2\sigma(R_0)}{R_0} \right) \left( \frac{R}{R_0} \right)^{-3\kappa} \left( 1 - \frac{3\kappa\dot{R}}{c} \right) - \\ &- P_0 - P_{AC}(t) - \frac{2\sigma(R)}{R} - 4\mu \frac{\dot{R}}{R} - 4\kappa_s \frac{\dot{R}}{R^2} \end{aligned} \quad (6.18)$$

Equation 6.18 differs from the free gas bubble Equation 6.3 only for the effective surface tension  $\sigma(R)$  term and the shell viscosity term. This model has been shown to capture the features of coated bubble phenomena, such as the bubble compressibility, even for large-amplitude oscillations (e.g. compression-only behavior) [28]. Linearization of equation 6.18 yields the following eigenfrequency in the elastic regime [30]:

$$f_0 = \frac{1}{2\pi} \sqrt{\frac{1}{\rho R_0^2} \left( 3\kappa P_0 + \frac{2(3\kappa - 1)\sigma(R_0)}{R_0} + \frac{4\chi}{R_0} \right)} \quad (6.19)$$

The eigenfrequency has two contributions, the eigenfrequency 6.8 for an uncoated bubble, and a shell contribution which increases the eigenfrequency. The linearization also gives the expression of the total damping coefficient (neglecting thermal damping) in presence of a shell: [30]  $\delta = \delta_{rad} + \delta_{vis} + \delta_{shell}$ , with a contribution coming from the re-radiation of sound:

$$\delta_{rad} = \frac{\omega_0 R_0}{c} \quad (6.20)$$

a viscous contribution:

$$\delta_{vis} = \frac{4\mu}{R_0^2 \rho \omega_0} \quad (6.21)$$

and a shell viscosity contribution:

$$\delta_{shell} = \frac{4\kappa_s}{R_0^3 \rho \omega_0}. \quad (6.22)$$

## 6.3 Experimental results

The experiments presented in this section were performed with the setup combining the optical tweezers to the ultra-high speed camera “Brandaris 128”, which is described in Chapter 5.

### 6.3.1 Amplitude of oscillations near a boundary

The influence of the sample chamber wall on the bubble dynamics was studied by comparing the behavior of the same bubble near the wall and away from the wall [31]. A bubble with a resting radius of  $R_0 = 2.45 \mu\text{m}$ , initially floating at the top wall of the sample chamber, was trapped with the optical tweezers and positioned in a region of the sample where no other bubbles were present in an area of approximately  $50 \times 50 \mu\text{m}^2$ . The radial oscillation upon ultrasound insonation was initially recorded with the bubble freely floating against the wall. Operating at 15 Mfps the temporal resolution of the high-speed camera was 65 ns. Then the bubble was positioned  $50 \mu\text{m}$  away from the wall and its dynamics was recorded; finally it was positioned back at the wall and the oscillations were recorded again, to double-check whether a difference in its behavior should be ascribed to a change in bubble properties. The radius-time curves shown in Figure 6.3 indicate that the vicinity of the wall suppresses the amplitude of oscillations for one and the same microbubble by more than 50%. This finding can be attributed to three distinct effects. First, the vicinity of a rigid wall is expected to cause a shift in the resonance frequency of the bubble [23]. As these experiments were carried out at a fixed insonation frequency of 2.25 MHz, a shift in the resonance frequency results in different amplitudes of oscillations being observed at the wall and away from the wall. Second, a full description of the bubble-wall system has to account also for a dissipation introduced by the viscous boundary layer at the wall, which is not taken into account when applying the image bubble method. This phenomenon

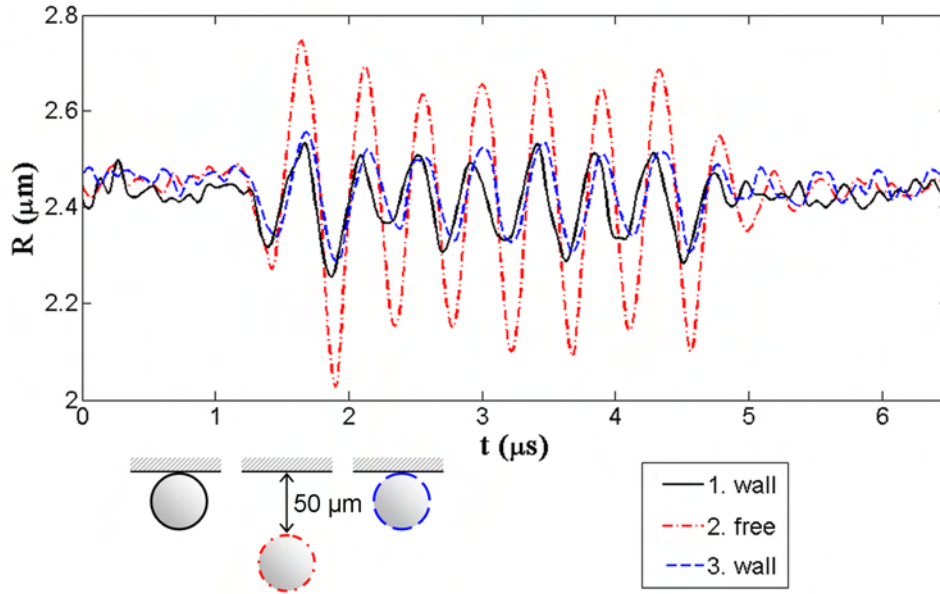


**Figure 6.3** Three  $R-t$  curves of a single bubble with an initial radius  $R_0 = 2.45 \mu\text{m}$ , insonified with a 8-cycle ultrasound burst at 2.25 MHz with an applied pressure of 200 kPa. The frame rate is 15 Mfps. The solid line represents the amplitude of oscillations at the wall; the dash-dotted line is recorded with the bubble at a distance of  $50 \mu\text{m}$  away from the wall. The dashed line is the radius-time curve of the same bubble repeated at the wall.

contributes to the damping of the oscillations, in addition to the other damping mechanisms for coated bubbles (bulk and shell viscosity, thermal diffusion, re-radiation of sound). Finally, asymmetric oscillations may arise in the vicinity of the wall. The eccentricity of bubbles in the vicinity of a capillary wall and driven at comparable pressures has been indeed reported to be close to 0.7 [8], although these observations were made on adherent bubbles. In our experiments, the possible adhesion to the wall was excluded by verifying with the optical tweezers whether bubbles were indeed non-adherent, yet in contact with the wall. In order to visualize asymmetric oscillations the behavior in a plane orthogonal to the wall should be observed, however this was not possible in our present setup without major modifications. The optical tweezers setup allowed nonetheless decoupling of the mechanisms listed above. The resonance frequency shift induced by the image bubble can be observed by studying a real two-bubbles system. Then the viscous boundary layer induced by the wall is not present. Furthermore in this case the system is imaged in the plane containing both the bubbles. Should asymmetric oscillations arise, they would then be detected from this point of observation. We therefore investigated the radial dynamics of a bubble pair, then released one bubble and studied the behavior of the residual bubble. Two bubbles having similar size were trapped using a two-trap DOE (see Section 4.3.2), with a distance between the bubbles in the same order as their diameter. The bubble

pair was then positioned  $50\ \mu\text{m}$  away from the wall to reduce wall effects as previously discussed, and to extract information purely on the bubble-bubble interaction. Figure 6.4 shows the result of such an experiment: the initial radius of the bubbles is  $2.25\ \mu\text{m}$  and  $2.40\ \mu\text{m}$ , respectively, the bubble centers being  $8\ \mu\text{m}$  apart. The dynamics of the bubble pair in ultrasound ( $f = 2.25\ \text{MHz}$ ,  $P_{AC} = 150\ \text{kPa}$ ) was first recorded at 15 Mfps, see the radius-time curves of Figure 6.4(c). Subsequently one trap was switched off and the dynamics of the remaining bubble was recorded. Figure 6.4(d) shows the corresponding radius-time curve, together with the radius-time curve previously recorded for the same bubble in presence of the second bubble. When comparing the two  $R - t$  curves for the very same bubble in presence and in absence of a second bubble, it is apparent that bubble oscillations are highly suppressed by the presence of the neighboring bubble. In repeated experiments the two bubbles retained their spherical symmetry. In this case, we can thus ascribe the change in the bubble response to the coupling of oscillations. In order to get a deeper insight in these mechanisms, experiments were then performed to measure the resonance frequency curves.

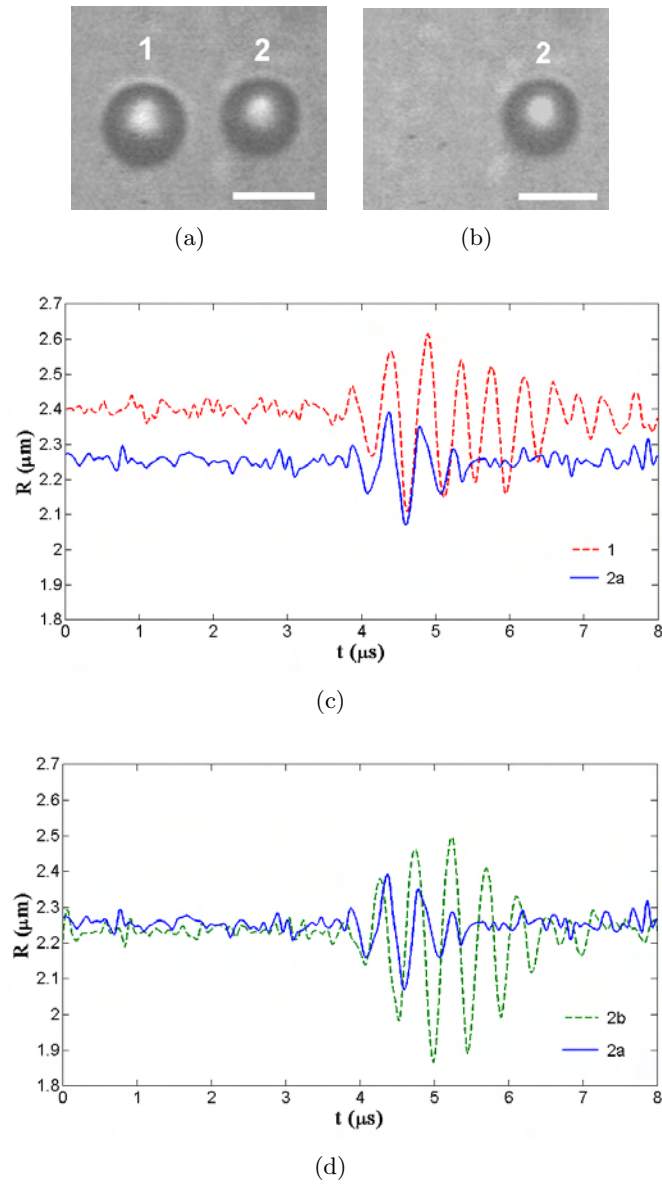


**Figure 6.4** (a) Two UCA microbubbles are trapped at a center-to-center distance of  $8\ \mu\text{m}$ , and positioned  $50\ \mu\text{m}$  away from the wall; (b) One of the microbubbles is released by switching off one of the optical traps. Scalebar:  $5\ \mu\text{m}$ . (c)  $R-t$  curves of the two bubbles as shown in Figure 6.4(a); the dashed curve 1 corresponds to bubble 1, the solid line 2a corresponds to bubble 2. (d) The dashed line 2b represents the  $R-t$  curve of bubble 2 oscillating after bubble 1 has been released. The  $R-t$  curve 2a is also plotted for comparison.



### 6.3.2 Resonance frequency shift

Resonance frequency curves of individual microbubbles can be reconstructed using the Brandaris 128 camera [32], with the method developed by van der Meer *et al.* [30]. The method, termed *bubble spectroscopy*, is shortly described here. The camera can record six movies of 128 frames at up to 25 million frames per second. Furthermore, it was designed to operate in a segmented mode: the conventional single acquisition of 128 frames can be replaced by recording two segments of 64 frames each. The camera houses memory space for six conventional acquisitions of 128 frames, before the images are transferred to the PC. This procedure results in the recording of 12 sets of 64 frames. The camera is operated at a framing rate of 15 million frames per second. The segmented mode allows to construct a resonance curve of the bubble in a single acquisition. We initially estimate the radius of the bubble from the images of the CCD camera, and estimate its approximate resonance frequency through Equation 6.8, taking into account that the shell elasticity shifts the resonance frequency up. The bubble is then subjected to a scan of 12 different frequencies, in a range of roughly 1 MHz below and above the expected resonance frequency. The movies are processed to obtain the 12  $R - t$  curves and the amplitude of oscillation for each frequency component is quantified using the algorithm presented in [30]. Plotting the results yields an experimental resonance frequency curve. We extract a resonance frequency curve by fitting the data with a linear oscillator response (6.2.3). Any non-linear influence of the acoustic amplitude is neglected, even though in that case the resonance curves can become asymmetrical, with the maximum shifted to a lower frequency.

**Resonance frequency shift for a bubble close to a wall** We performed a bubble spectroscopy experiment on the very same microbubble under different boundary conditions: close to the sample chamber wall, and positioned  $50 \mu\text{m}$  away from the wall. In this experiment the laser trap is not switched off during the recordings for the bubble away from the wall. The 12 recordings are performed in a single run, with a delay of 40 ms between the recordings, therefore the bubble would rise up due to buoyancy. The optical trap allows controlling the position of the bubble throughout the experiment. The possible influence of the optical trap on the dynamics was preliminarily assessed, and repeated measurement showed that the bubble behavior is not affected by the laser, as reported in Section 5.3.2. Figure 6.5 shows the result of a bubble spectroscopy experiment on a bubble having resting radius  $R_0 = 1.7 \mu\text{m}$ , insonified with a set of frequencies from 1.7 MHz to 3.5 MHz with an applied pressure  $P_{AC} = 100 \text{ kPa}$ . The red curve is recorded when the bubble is freely floating against the wall. Positioning of the bubble  $50 \mu\text{m}$  away from the wall results in the blue curve. A shift in resonance frequency due to the wall vicinity is indeed observed, as predicted by the image bubble model. The amplitude of the resonance frequency curve at the wall is smaller than for the free bubble, as opposed to the predictions of the image-bubble model which does not include the dissipation at the viscous boundary

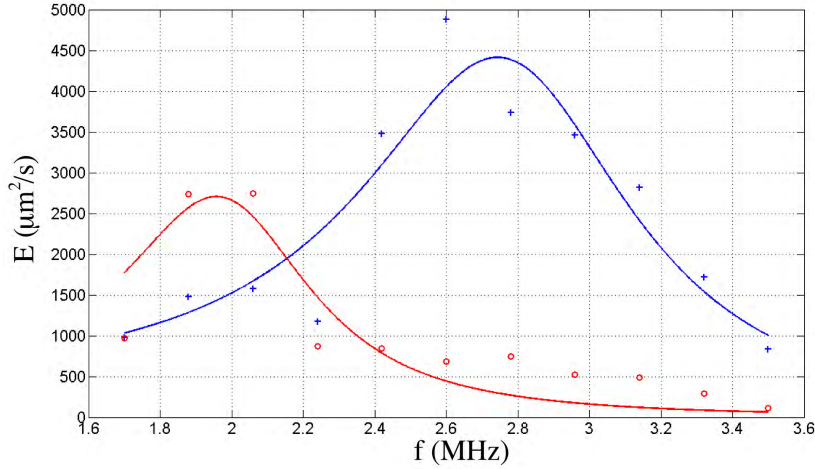


**Figure 6.5** Bubble spectroscopy experiments on a bubble having resting radius  $R_0 = 1.7 \mu\text{m}$ . The very same bubble is first insonified when it is freely floating against the chamber wall (red curve), and then after positioning it  $50 \mu\text{m}$  away from the wall using the optical tweezers (blue curve). To reconstruct the two resonance frequency curves, in both experiments the bubble is insonified with a set of frequencies from 1.7 MHz to 3.5 MHz, with an applied pressure  $P_{AC} = 100 \text{ kPa}$ . The shift in resonance frequency due to the wall vicinity is consistent with the theoretical predictions.

layer at the wall. Again, the same experiment can be performed on the real two-bubble system, with the advantage of decoupling boundary layer effects from the acoustic mechanism responsible for the change in bubble behavior.

**Resonance frequency shift for a bubble pair** Using the same method, we compared the resonance frequency curves for one and the same bubble oscillating in vicinity of a second bubble, and then freely oscillating after releasing the other bubble from the optical trap. Figure 6.6 shows the resonance frequency curves for a  $1.9 \mu\text{m}$  bubble. Two bubbles are initially trapped, with a center-to-center distance of  $8 \mu\text{m}$ , and resting radius  $R_{1,0} = 1.9 \mu\text{m}$  and  $R_{2,0} = 2.0 \mu\text{m}$ , respectively. They are then positioned  $70 \mu\text{m}$  away from the chamber wall to reduce wall effects. The resonance frequency curves are reconstructed for the two bubbles: in Figure 6.6 the curve for the  $1.9 \mu\text{m}$  bubble is plotted in blue. The  $2.0 \mu\text{m}$  bubble is then released by switching off the corresponding trap. The residual bubble is insonified again and its resonance frequency curve as a freely oscillating bubble is recorded (green). In both experiments the applied pressure is  $P_{AC} = 90 \text{ kPa}$ . The resonance frequency is decreased for the case where the bubble oscillates close to the second bubble, as expected from the analogy with the bubble-image bubble system. Note that in this case the shift is smaller, due to the fact that the two bubbles are a few  $\mu\text{m}$  apart, whereas the shift calculated in Section 6.2.5 was for a bubble *in contact* with the wall (i.e. for two bubbles in contact). Remarkably, in this case the amplitude of the curves follows the

predictions of the image bubble model, since there is no boundary layer due to a wall. The amplitude of the resonance curve for the bubble oscillating next to another bubble is indeed larger than for the free bubble.

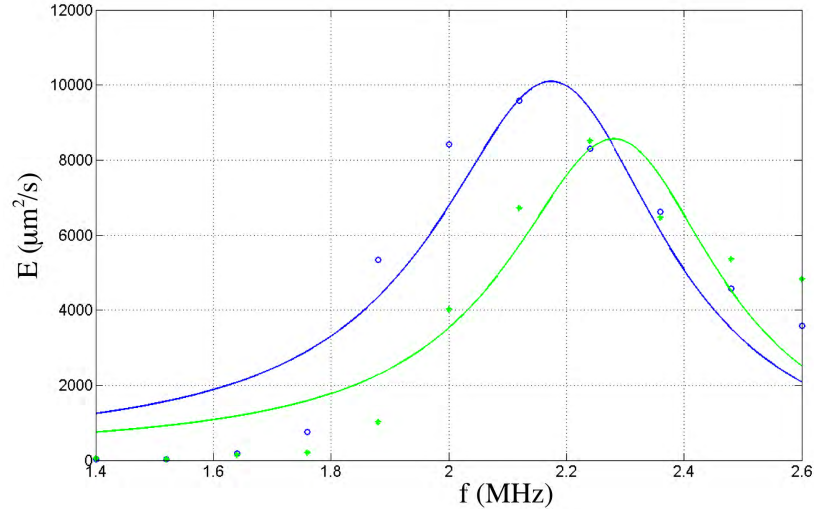


**Figure 6.6** Resonance frequency curves for the same bubble when it freely oscillates (green) and when it oscillates in proximity of a second bubbles. The bubble radii are  $R_{1,0} = 1.9 \mu\text{m}$  and  $R_{2,0} = 2.0 \mu\text{m}$  respectively. The two curves are recorded for the  $1.9 \mu\text{m}$  bubble. The bubbles are positioned  $70 \mu\text{m}$  away from the wall to reduce wall effects. The applied pressure is 90 kPa. The resonance curve for the bubble oscillating in close vicinity to the second bubble exhibits a lower resonance frequency and a larger amplitude, as expected from the models.

### 6.3.3 Secondary Bjerknes force

The effect of the secondary Bjerknes force in the two-bubble experiments is evaluated by tracking the bubble centers coordinates, calculating the displacements along the line of centers  $z$ ,  $z_1(t)$  and  $z_2(t)$  respectively, and plotting the evolution in time of the distance between the bubbles,  $D(t) = |z_2(t) - z_1(t)|$ . We calculated such distance-time curves for the experiments where 128-frame movies of bubble pairs were recorded. In Figure 6.7 a distance-time curve is shown (green) for two bubbles with resting radius  $R_{1,0} = 2.0 \mu\text{m}$  and  $R_{2,0} = 2.0 \mu\text{m}$ . The interframe time (65 ns) allows resolving the translation oscillations due to the alternating secondary Bjerknes force. A net attractive force is observed, since the bubbles oscillate in phase (see  $R - t$  curves in Figure 6.7). Initially, the distance between the bubbles is  $6.7 \mu\text{m}$ . During the insonation the bubbles are attracted, and when the acoustic pressure is removed their final distance is  $5.5 \mu\text{m}$ . A comparison of

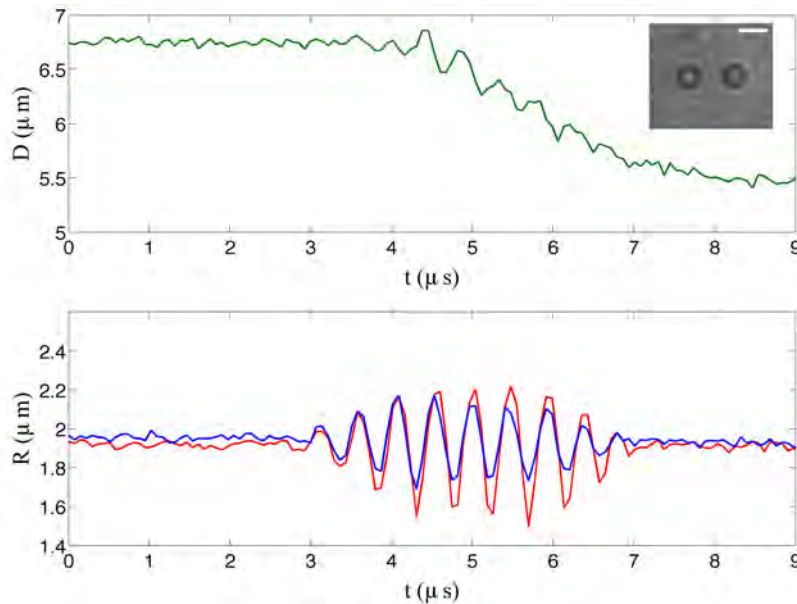
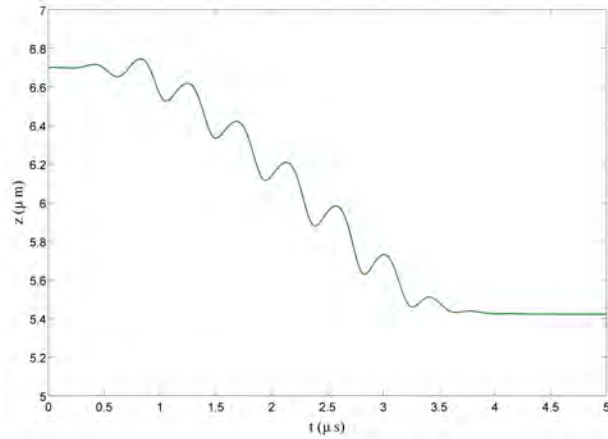


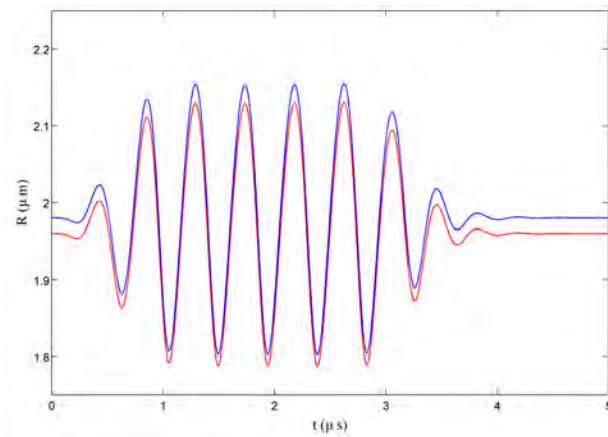
**Figure 6.7** Distance-time curve (green) for two bubbles with resting radius  $R_{1,0} = 2.0 \mu\text{m}$  and  $R_{2,0} = 2.0 \mu\text{m}$ . Initially, the distance between the bubbles is  $6.7 \mu\text{m}$ . A net attractive secondary Bjerknes force is observed, since the bubbles oscillate in phase, as it can be seen from the  $R - t$  curves (red, blue).

these observations with the theoretical force balance described in Section 6.2.7 can provide quantitative information on the interplay of acoustical and hydrodynamical forces acting on the system. Quantification of viscous forces remains elusive on the microscale, and small-Reynolds number effects may not be negligible in the present case. We compute distance-time curves by numerically solving the set of ODEs 6.12, 6.14 and 6.15. The effect of the coating is also included, as described in Section 6.2.8, through a shell viscosity  $\kappa_s$  and a shell elasticity  $\chi$ . In Figure 6.8(a) the resulting distance-time curve,  $z(t)$  is shown for two bubbles

having initial radius  $R_{1,0} = 1,96 \mu\text{m}$  and  $R_{2,0} = 1.98 \mu\text{m}$ , respectively, with an initial distance  $z_0 = 6.7 \mu\text{m}$ , corresponding to the experiment of Figure 6.7. A good agreement is already observed both in the  $R - t$  and distance-time curves. The model will be refined for a direct, quantitative comparison with the experiments, to give an estimate of the secondary Bjerknes force and of the importance of small-Reynolds number effects.



(a)



(b)

**Figure 6.8** Result of numerical simulations for two bubbles with initial radius  $R_{1,0} = 1,96 \mu\text{m}$  and  $R_{2,0} = 1.98 \mu\text{m}$  at an initial distance  $z_0 = 6.7 \mu\text{m}$  insonified at 90 kPa. The parameters of the shell are  $\kappa_s = 2 \times 10^{-8} \text{ kg/s}$  and  $\chi = 0.6 \text{ N/m}$ . Distance-time curve (green) and radius-time curves (blue, red).

## 6.4 Conclusions

We presented some preliminary experiments directed to the quantitative characterization of the boundary-dependent UCA microbubble dynamics at the single-bubble level. We compared the behavior of the very same UCA microbubble under different boundary conditions, by a well-controlled positioning of individual bubbles using Laguerre-Gaussian optical tweezers and by recording their ultrasound-driven oscillations with an ultra-high speed camera. We therefore introduced a powerful tool for investigating how the bubble dynamics, hence the acoustical signature, changes with varying distance to neighboring objects. A deeper understanding of these phenomena may lead to novel imaging modalities together with the use of functionalized microbubbles specifically designed for targeted diagnostic ultrasound imaging.

## Bibliography

- [1] J. Raichlen B.B. Goldberg and F. Forsberg. *Ultrasound Contrast Agents: Basic Principles and Clinical Applications, 2nd ed.* London: Dunitz, 2001.
- [2] P. Frinking, A. Bouakaz, J. Kirkhorn, F. ten Cate and N. de Jong. Ultrasound contrast imaging: current and potential methods. *Ultrasound Med. Biol.*, 26:965–975, 2000.
- [3] N. de Jong, R. Cornet, C.T. Lancée. Higher harmonics of vibrating gas filled microspheres. Part one: Simulations. *Ultrasonics*, 32:447–453, 1994.
- [4] N. de Jong, A. Bouakaz and P. Frinking. Basic acoustic properties of microbubbles. *Echocardiography*, 19:229–240, 2002.
- [5] D.L. Miller, J. Quddus. Sonoporation of monolayer cells by diagnostic ultrasound activation of contrast-agent gas bodies. *Ultrasound. Med. Biol.*, 26:661–667, 2000.
- [6] A. van Wamel, K. Kooiman, M. Hartevelde, M. Emmer, F.J. ten Cate, M. Versluis, N. de Jong. Vibrating microbubbles poking individual cells: Drug transfer into cells via sonoporation. *J. Control. Release*, 112:149–155, 2006.
- [7] A.L. Klibanov. Microbubble contrast agents. Targeted ultrasound imaging and ultrasound-assisted drug-delivery applications. *Invest. Radiol.*, 41:354–362, 2006.
- [8] S. Zhao, K.W. Ferrara and P.A. Dayton. Asymmetric oscillation of adherent targeted ultrasound contrast agents. *Appl. Phys. Lett.*, 87:134103, 2005.
- [9] M. Lankford, C.Z. Behm, J. Yeh, A.L. Klibanov, P. Robinson and J.R. Lindner. Effect of microbubble ligation to cells on ultrasound signal enhancement. implications for targeted imaging. *Invest. Radiol.*, 41:721–728, 2006.
- [10] S. Zhao, D.E. Kruse, K.W. Ferrara, and P.A. Dayton. Acoustic response from adherent targeted contrast agents. *J. Acoust. Soc. Am.*, 120:EL63–EL69, 2006.
- [11] T.G. Leighton. *The acoustic bubble.* London: Academic Press, 1994.
- [12] M.S. Plesset and A. Prosperetti. Bubble dynamics and cavitation. *Annu. Rev. Fluid Mech.*, 9:145–185, 1977.
- [13] C.E. Brennen. *Cavitation and Bubble Dynamics.* New York: Oxford U. Press, 1995.
- [14] A. Prosperetti. Bubble phenomena in sound fields: Part one. *Ultrasonics*, 9:69–77, 1984.
- [15] J.B. Keller and M. Miksis. Bubble oscillations of large amplitude. *J. Acoust. Soc. Am.*, 68:628–633, 1980.

- 
- [16] S. Hilgenfeldt, D. Lohse and M. Zomack. Response of bubbles to diagnostic ultrasound: a unifying theoretical approach. *Eur. Phys. J. B*, 4:247–255, 1998.
- [17] M. Minnaert. On musical air-bubbles and the sounds of running water. *Phil. Mag.*, 16:235–248, 1933.
- [18] K. Sato, Y. Tomita, and A. Shima. Numerical-analysis of a gas bubble near a rigid boundary in an oscillatory pressure field. *J. Acoust. Soc. Am.*, 95:2416–2424, 1994.
- [19] C.C. Church. The effects of an elastic solid surface layer on the radial pulsations of gas-bubbles. *J. Acoust. Soc. Am.*, 97:1510–1521, 1995.
- [20] E. A. Brujan, K. Nahen, P. Schmidt and A. Vogel. Dynamics of laser-induced cavitation bubbles near an elastic boundary. *J. Fluid. Mech.*, 433:251–281, 2001.
- [21] Y. Tomita, P.B. Robinson, R.P. Tong and J.R. Blake. Growth and collapse of cavitation bubbles near a curved rigid boundary. *J. Fluid. Mech.*, 466:259–283, 2002.
- [22] P. Marmottant, M. Versluis, N. de Jong, S. Hilgenfeldt, D. Lohse. High-speed imaging of an ultrasound-driven bubble in contact with a wall: “narcissus” effect and resolved acoustic streaming. *Exp. Fluids*, 41:147–153, 2006.
- [23] M. Strasberg. The pulsation frequency of nonspherical gas bubbles in liquids. *J. Acoust. Soc. Am.*, 25:536–537, 1953.
- [24] M.L.J. Overvelde. *3D optical micromanipulation of ultrasound contrast agents: bubble-bubble and bubble-wall interactions*. MSc thesis, University of Twente, The Netherlands, 2006.
- [25] A. Harkin, T.J. Kaper, and A. Nadim. Coupled pulsation and translation of two gas bubbles in a liquid. *J. Fluid Mech.*, 445:377–411, 2001.
- [26] J. Magnaudet, D. Legendre. The viscous drag force on a spherical bubble with time-dependent radius. *Phys. Fluids*, 10:550–554, 1998.
- [27] C.D. Ohl, A. Tijink and A. Prosperetti. The added mass of an expanding bubble. *J. Fluid Mech.*, 482:271–290, 2003.
- [28] P. Marmottant, S.M. van der Meer, M. Emmer, M. Versluis, N. de Jong, S. Hilgenfeldt and D. Lohse. A model for large amplitude oscillations of coated bubbles accounting for buckling and rupture. *J. Acoust. Soc. Am.*, 118:3499–3505, 2005.
- [29] D. Chatterjee and K. Sarkar. A newtonian rheological model for the interface of microbubble contrast agents. *Ultrasound. Med. Biol.*, 29:1749–1757, 2003.



- 
- [30] S.M. van der Meer, B. Dollet, M.M. Voormolen, C.T. Chin, A. Bouakaz, N. de Jong, M. Versluis, D. Lohse. Microbubble spectroscopy of ultrasound contrast agents. *J. Acoust. Soc. Am.*, 121:684–656, 2007.
- [31] V. Garbin, D. Cojoc, E. Ferrari, E. Di Fabrizio, M.L.J. Overvelde, S.M. van der Meer, N. de Jong, D. Lohse, M. Versluis. Changes in microbubble dynamics near a boundary revealed by combined optical micromanipulation and high speed imaging. *Appl. Phys. Lett.*, accepted for publication.
- [32] C.T. Chin, C. Lancée, J. Borsboom, F. Mastik, M.E. Frijlink, N. de Jong, M. Versluis and D. Lohse. Brandaris 128: A digital 25 million frames per second camera with 128 highly sensitive frames. *Rev. Sci. Instr.*, 74:1–9, 2003.



## Chapter 7

# Force spectroscopy of antigen-antibody complexes

This Chapter presents the experiments performed during a research stay at Lang Lab, Biological Engineering Division of MIT. Optical tweezers were applied to single-molecule force spectroscopy of antigen-antibody complexes. The interest in single-molecule studies is shortly motivated in 7.1. The working principles of optical tweezers as a force sensor are first reviewed in 7.2. The optical tweezers setup in use at Lang Lab, and the protocols for tethered bead assays preparation, are then described in 7.3. Finally, some preliminary rupture force measurements on the fluorescein-anti fluorescein complex are presented in 7.4.

## 7.1 Introduction

The characterization of ligand-receptor interactions is crucial for targeted molecular imaging applications. Antigen-antibody recognition and binding plays an important role besides the immune response, as antibodies against different molecules can be produced and engineered, and used for specific targeting. Single-molecule techniques can aid ligand optimization, receptor design, and screening processes, by giving a deeper insight in the interaction than the macroscopic, ensemble-averaged, affinity measurements. Probe microscopy techniques, mainly atomic force microscopy [1] and optical tweezers [2], enabled examination of intermolecular interactions for individual molecular pairs, by measuring the rupture force of the bond, which is typically of the order of few pN for DNA base pairing, or tens to hundreds of pN for protein-protein interactions.

### 7.1.1 Characterization of individual intermolecular bonds

Weak bonds are central to reversible interactions between biomolecules. Noncovalent forces play a key role in DNA replication, protein folding, specific recognition of substrates by enzymes, and detection of signal molecules. Intermolecular bonds are traditionally investigated in bulk, with the reactants free in solution under equilibrium conditions. The ensemble average of the behavior of the molecules is thus observed. For some molecules, however, the environment of the solution is not an accurate reproduction of the relevant *in vivo* conditions: for example membrane proteins, which are not water-soluble, in solution change their conformation and then their behavior. Optical tweezers have been demonstrated to function as an effective force transducer in the range spanning fractions of pN to few hundreds of pN [3]. They are thus a suitable tool for characterizing weak bonds, also in severe environmental conditions. In addition, this technique can be coupled to well established imaging techniques (single- and two-photon fluorescence, single molecule fluorescence, FRET) giving simultaneously mechanical and optical information.

### 7.1.2 Rupture force probability distribution

The relevant parameters in describing a ligand-receptor system displaying simple reversible 1:1 binding are the rates of spontaneous association ( $k_{on}$ ), and dissociation ( $k_{off}$ ) and their ratio, the dissociation constant  $K_D = \frac{k_{off}}{k_{on}}$ , which describes the equilibrium behavior. Biomolecular linkages will fail under any level of pulling force if held for sufficient time [4]: under external force the energetic state of a chemical bond drops as the constituents separate to an ultimate state comparable to infinite dilution. Dissociation under force is far from equilibrium kinetics: the on-rate of bond association can be neglected. Rupture strengths depend on the rate of force application and duration of loading. By definition [4], bond strength is the force that produces the most frequent failure in repeated testes of breakage, i.e. the peak in the distribution of rupture forces. The likelihood of bond detachment under force represents a first-order kinetic process. The probability

of failure is expressed by [5, 6]:

$$p(F) = \frac{k_{off}}{\frac{\partial F}{\partial t}} \exp\left(\frac{F x}{k_B T}\right) \exp\left(\frac{k_{off} k_B T}{\frac{\partial F}{\partial t} x} \left(1 - \exp\left(\frac{F x}{k_B T}\right)\right)\right) \quad (7.1)$$

where  $k_B$  is the Boltzmann constant,  $T$  the temperature and  $\frac{\partial F}{\partial t}$  is the (constant) loading rate. From the rupture force distributions, we extract zero-force parameters for the system, namely the thermal off-rate  $k_{off}$  in absence of load and the distance  $x$  to the transition state along the reaction coordinate.  $F$  represents the  $x$  component of the rupture force.

## 7.2 Methods

### 7.2.1 Optical-trap force sensor

The approach for probing biomolecular complexes includes the use of polystyrene or silica microbeads as tiny handles. Such materials are strongly trapped by optical tweezers, and the shape and uniform size of commercially available microbeads facilitate calibration. The molecules of interest can be linked through non-specific adhesion, covalent bond or through a tether molecule to beads and various substrates. Typically, one of the molecules is linked to a microbead confined in the optical trap. The other molecule can be linked to another bead confined in a second optical trap [7], to a micropipette [8], or to a coverslip. The displacement  $x$  of the trapped bead from its equilibrium position in the optical trap gives a measurement of the force exerted on the system. For small displacements  $x$  from the center of the trap, the particle indeed experiences an approximately harmonic potential and the force on the particle is given by Hooke's law:

$$F = -\alpha x$$

To compute the force  $F$ , the *stiffness*  $\alpha$  of the trap is first determined. It is then used in conjunction with the measured displacement  $x$  from the equilibrium trap position. In most applications, forces are calibrated against viscous drag exerted by fluid flow. Calibration is facilitated by the fact that the Reynolds number is typically small for micron-sized objects:  $Re = va\rho/\eta \sim 10^{-5}$ , where  $v$  is the fluid velocity,  $a$  is the particle size,  $\rho$  is the particle density, and  $\eta$  is the fluid viscosity. Inertial forces are therefore negligible, and the drag force on a stationary object is  $F_{drag} = \beta v$ , where  $\beta$  is the drag coefficient and  $v$  is the fluid velocity [9]. For a sphere of radius  $a$ ,  $\beta$  is given by Stokes' law:  $\beta = 6\pi\eta a$ . Position detection can be performed in different ways, for instance by directly imaging the particle, or by interferential methods (for a recent review including design considerations, see e.g. [10]).

Here, position measurement is performed with nm-precision by detecting, in the back-focal plane of the microscope condenser, the pattern of fringes generated by the interference between the light forward-scattered by the particle, and the

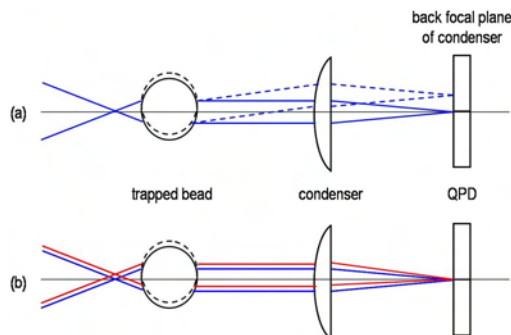


Figure 7.1 Back-focal plane detection.

unscattered portion of the beam. A second, low power laser beam is used for generating such interference pattern, which is detected by a quadrant photodiode (QPD) or other position sensitive detector (PSD). For the commonly employed geometry in which the molecular complex of interest is attached between the surface of the trapping cell and a trapped bead, incorporation of a piezoelectric stage enables for dynamic positioning of the sample chamber relative to the trap and for calibration.

**Back-focal plane position detection** As mentioned above, laser light passing through the specimen is collected on a PSD placed on the optical axis in a position that is optically conjugate to the back-focal plane of the condenser. In this configuration the PSD response is insensitive to the  $(x, y)$  position of the optical trap, wherever the trap is located (within an area  $\sim 5 \mu\text{m} \times 5 \mu\text{m}$ ). Only displacements of trapped objects relative to the center of the trap are detected (see Figure 7.1). Position measurement would be indeed totally independent of trap location, if the beam was perfectly collimated by the trapped bead. In practice, position-independent response can be achieved for a given particle by adjusting the axial position of the sensor while moving both the optical trap and the particle together, until the detector signal is nulled.

## 7.2.2 Force measurements

The procedure for measuring  $F$  can be summarized as follows:

- **position calibration:** calibration of the detector output as a function of position. A stuck bead is scanned through the trap area, see 7.2.3. This step is required also for stiffness calibration.
- trapping of a bead and positioning at a known distance  $h$  from the wall
- **stiffness calibration** with one of the methods presented in 7.2.4
- **force measurement:** by measuring the displacement  $x$  of the bead from the center of the trap during the experiment.

### 7.2.3 Position calibration

Position calibration can be accomplished by moving a fixed bead through the detection beam and recording the detector output as a function of position. The bead can be moved in a raster scan across the detection region, while recording output signal for each point on the grid. One can either move a stuck bead, by moving the stage, or a trapped bead, by moving the trapping beam (when the detection beam is not the same as the trapping beam), for instance by deflecting the trapping beam using acousto-optic deflectors (AOD).

### 7.2.4 Stiffness calibration

Stiffness calibration can be performed following different methods. Here, three methods are described which rely on back-focal plane (BFP) detection of the particle's displacement relative to the center of the trap.

#### 7.2.4.1 Power spectrum

The power spectrum of the thermal fluctuations of a trapped object in a harmonic potential (see Section 2.2.5) is described by a Lorentzian (for one dimension,  $x$  or  $y$ )

$$S(f) = \frac{k_B T}{\pi^2 \beta (f_0^2 + f^2)} \quad (7.2)$$

where the *roll-off frequency*  $f_0$  is given by

$$f_0 = \frac{\alpha}{2\pi\beta} \quad (7.3)$$

One can thus record the power spectrum of a trapped particle, fit the data in order to extract the roll-off frequency and, knowing the drag coefficient  $\beta$ , calculate the stiffness  $\alpha$ . The drag coefficient calculation will be discussed in 7.2.4.3.

#### 7.2.4.2 Equipartition

The equipartition theorem for the Brownian motion of an object in a harmonic potential reads:

$$\frac{1}{2} k_B T = \frac{1}{2} \alpha \langle x^2 \rangle \quad (7.4)$$

The positional variance  $\langle x^2 \rangle$  can be measured (acquisition of a number  $N$  of displacements  $x_i$ , due to Brownian motion, average  $\frac{\sum_{i=1}^N x_i}{N}$ ) and, knowing the temperature  $T(K)$ , and the Boltzmann constant  $k_B = 1.38 \cdot 10^{-23} \text{ m}^2 \text{ kg s}^{-2} \text{ K}^{-1}$ , the stiffness can be calculated.

#### 7.2.4.3 Drag force

The displacement of a trapped bead from its equilibrium position is measured, in response to viscous force. This can be produced by moving the stage. A set

of measurements can be acquired performing subsequent steps, each one with increasing velocity  $v$  (not so high as to cause the particle to escape the trap). For each velocity  $v$  the displacement from the center of the trap is measured, and the drag force can be estimated ( $F = -\beta v$ ) allowing to calculate the stiffness:

$$\alpha = -\frac{F}{x} \quad (7.5)$$

The results for  $\alpha$  can finally be averaged.

**Drag coefficient** The main drawback to the drag force method is that the drag must be corrected for the proximity to the coverglass surface, the effect of which can be large when the distance from the surface is comparable with the particle radius. The viscous drag coefficient of a sphere with radius  $a$  whose center is at a distance  $h$  from the surface is given by the Faxen's law [9]:

$$\beta = \frac{6\pi\eta a}{1 - \frac{9}{16}\left(\frac{a}{h}\right) + \frac{1}{8}\left(\frac{a}{h}\right)^3 - \frac{45}{256}\left(\frac{a}{h}\right)^4 - \frac{1}{16}\left(\frac{a}{h}\right)^5} \quad (7.6)$$

where  $a$  is the bead radius,  $h$  the distance above the surface,  $\eta$  the medium viscosity. For this reason it is important to know the distance of the trapped bead from the wall before stiffness calibration, for instance by moving the trap down and then back to the desired position.

#### 7.2.4.4 Influence of axial trapping position

The detection schemes described above were developed to measure lateral displacement of objects within the specimen plane, a major focus of most optical trapping work. Detecting axial motion within the optical trap has rarely been implemented and has not been as well characterized until recently, see e.g. [11]. However, the axial equilibrium trapping position is a function of transverse position [12]. Therefore, the interpretation of calibration measurements in  $(x, y)$  is not necessarily straightforward. The transverse position-dependent axial displacement would lead to an underestimate of force in experiments that strictly confine the particle to the equilibrium plane. Ashkin's computations suggest that this underestimate leads to only a small error (-5%), at least for larger particles [13].

## 7.3 Materials and apparatus

### 7.3.1 Fluorescein-anti fluorescein assay

Antigen binding affinities, reaction kinetics, spectral properties of several monoclonal anti-fluorescein antibodies are characterized in [14]. Five IgG antibodies were found exhibiting different, yet relatively high (nanomolar) affinities for fluorescein. We used the high-affinity, murine anti-fluorescein monoclonal antibody, clone 4-4-20 for unbinding measurements performed using a tethered-bead



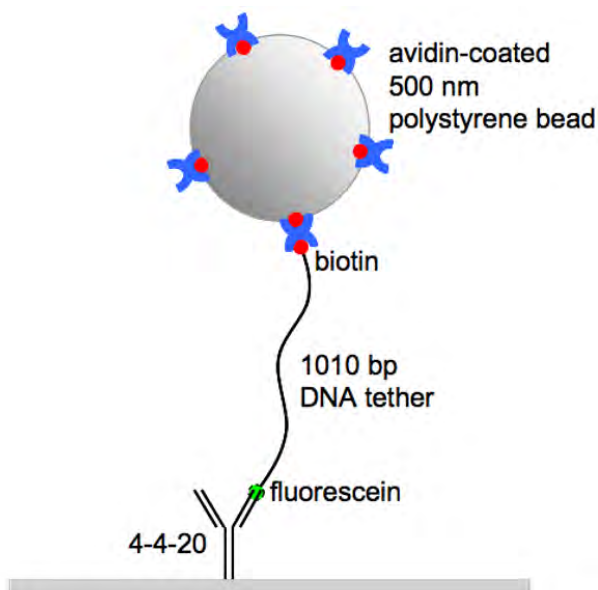


**Figure 7.2** Schematic optical layout of the instrument combining optical trapping and single molecule fluorescence [6].

(see Figure 7.2), manipulated with optical tweezers, as a probe [6]. The 4-4-20/fluorescein model system was also characterized in [15]. A correlation of the unbinding force measured with AFM to the off-rate was found for single-chain Fv fragments of three unrelated fluorescein-binding antibodies and their mutants. This indicates that the unbinding experiments on the molecular system are following a dissociation path not too dissimilar to the one at zero force [16, 17]. We measured the rupture force at a low, constant loading rate and extracted from the experimental rupture force probability distribution the thermal  $k_{off}$ . By measuring the rupture force for a set of loading rates, following [17] it will be possible to extract the natural  $k_{off}$  at zero force.

### 7.3.1.1 Assay preparation

Flow cells ( $\sim 30 \mu\text{l}$ ) were assembled from 1.5" glass coverslips attached to a microscope slide by two parallel strips of double-sticky tape, arranged to form a channel ( $\sim 0.5 \text{ cm}$  wide) running across the narrow axis of the slide. Prior to assembly, coverslips were sonicated in a saturated KOH-ethanol solution, rinsed with deionized water, and dried in an oven [18]. Flow cells were first incubated for 40 min with  $25 \mu\text{l}$  of  $15 \mu\text{g/ml}$  anti-fluorescein murine monoclonal 4-4-20 antibody (Molecular Probes), then washed with  $200 \mu\text{l}$  of  $1 \text{ mg/ml}$  casein in buffer solution ( $100 \text{ mM}$  phosphate buffer,  $\text{pH } 7.5$ ,  $0.1\%$  Tween). To reduce nonspecific binding of beads, the flow cells were incubated for 20 min with the casein solution. The flow cells were then perfused with  $40 \mu\text{l}$  DNA:bead complexes, and incubated for 15 min, followed by a final wash of  $400 \mu\text{l}$   $1 \text{ mg/ml}$  casein in buffer. All incubations took place in a humidity chamber at room temperature.

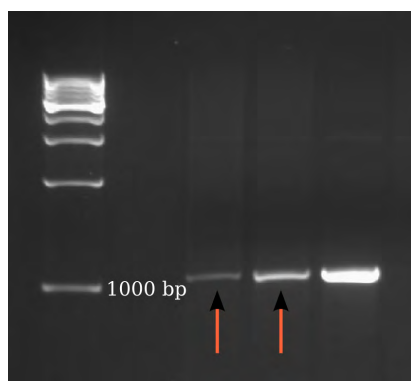


**Figure 7.3** The quality of the PCR products is checked by running them in an electrophoresis gel. 1010 bp DNA tethers are detected.

**Antibody concentration titration** The best antibody concentration to be immobilized on the glass coverslip surface was determined. Using an antibody concentration of 20  $\mu\text{g}/\text{ml}$ , re-binding events were observed. To reduce the number of free antibodies on the surface, concentration of anti-fluorescein was decreased to 15  $\mu\text{g}/\text{ml}$ . The number of re-bindings significantly decreased. Further decreasing antibody concentration (10  $\mu\text{g}/\text{ml}$ ), decreased the overall number of tethered beads. An antibody concentration of 15  $\mu\text{g}/\text{ml}$  was used in the experiments.

### 7.3.1.2 Tethered beads preparation

Beads were attached to the DNA tethers by incubating for 4 h at 4°C avidin-coated 500 nm beads (60 pM) with 20 pM DNA tethers, making sure that fewer than 10% of the beads had multiple complexes, assuming independent binding. DNA:bead complexes were then washed and resuspended 6 times in phosphate buffer before perfusion in the flow cells. The beads can be resuspended in casein to prevent sticking on the coverslip.

**DNA tethers amplification** 1010 bp DNA tethers were made using a PCR protocol from a M13mp18 plasmid (Bayou Biolabs, P-105). Biotin, for linkage to the avidin-coated bead, and fluorescein were incorporated via conjugation to the PCR primers (Operon Biotechnologies). The quality of the PCR products was checked by running them in an electrophoresis gel (see Figure 7.3).

**Beads:DNA concentration titration** A range of DNA concentrations for the DNA:beads mixture was tested, to determine the best ratio for the preparation of tethered beads. DNA was mixed 1:1 (volumes) to 60 pM beads, for a set of DNA concentrations (0.2 pM, 2 pM, 20 pM, 200 pM, 2 nM). For 200 pM and higher DNA concentrations, multiple tethers occur on the same bead: the majority of the beads appear to be stuck on the surface. For 2 pM and lower DNA

concentrations, few beads are tethered to the coverslip. A 20 pM concentration of DNA was used for the experiments.

### 7.3.2 Optical setup

The instrument (see Figure 7.4) combines optical trapping capabilities with single molecule fluorescence, and it is presented in full detail in [6]. The instrument is based on a Nikon TE2000 commercial inverted light microscope. Three lasers are coupled into the microscope objective: one for trapping (1064 nm); one for position detection (975 nm); and one for fluorescence excitation (532 nm and 488 nm). The light from all lasers overlaps at the specimen. The wavelengths used for trapping and position detection are well separated from those devoted to fluorescence excitation and emission, allowing the use of high-efficiency filters to reject the infrared trapping and detection light without compromising the fluorescence signal.

In order to position the PSD in a plane optically conjugate to the BFP of the condenser, the distance between the PSD and the relay lens has to be fixed (and equal to the focal length of the relay lens). The two elements are then moved together, until the condition of position-independent response of the PSD is realized: the laser beam is slightly moved and the response of the PSD is monitored; when the response is insensitive to displacements of the beam, the PSD is optically conjugate to the BFP.

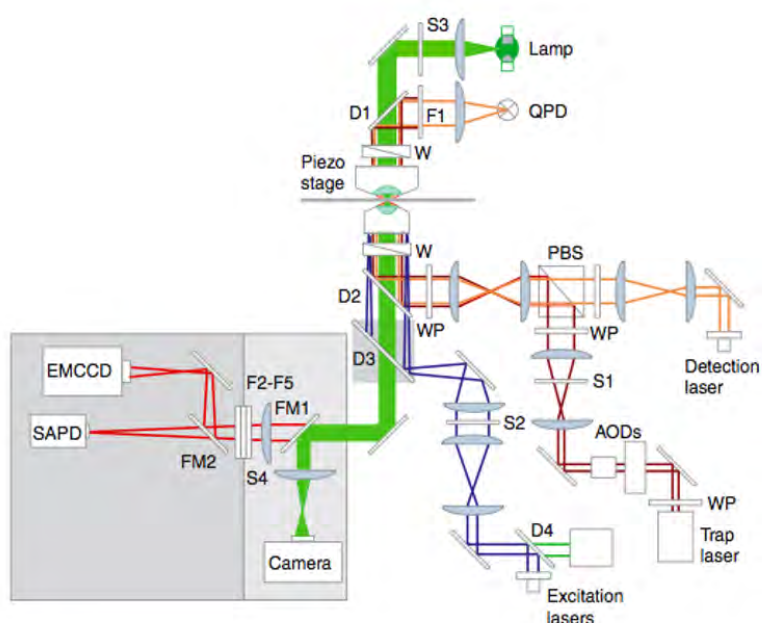


**Figure 7.4** Schematic optical layout of the instrument combining optical trapping and single molecule fluorescence. Light paths are shown for the transmission illumination (light green), trapping laser (dark red), position detection laser (orange), fluorescence excitation lasers (dark blue, green) and fluorescence emission (red). A QPD/PSD is used for BFP detection of the position, a video-rate analog camera for general imaging, a digital EMCCD camera for single-molecule fluorescence imaging. Acousto-optic deflectors (AODs) deflect the trapping beam. Electronic shutters (S1-S4) provide automatic control of the instrument. Optical filters isolate the diode laser emission (F1) and block the trap, detection and excitation laser wavelengths before fluorescence detection (F2-F5). Flipper mirrors (FM1-FM2) alternate between the photodetectors. Adapted from [6].

## 7.4 Results and data analysis

Measurement and calibration procedures are computer automated, using custom software. To begin each measurement, the detector beam is aligned with the center of the trap and the PSD. Next, the tethered bead is centered in  $(x, y)$  coordinates based on a measurement of the elastic extension of the DNA tether. Tethers producing abnormal stretching curves are discarded, eliminating beads with multiple tethers or non-specific attachments. To cause the rupture event, the stage pulls the bead out of the trap center, increasing the force on the complex until rupture. After rupture is detected, the bead is raster-scanned with the AODs over the detection region to calibrate the PSD sensitivity. Accurate calibration of the PSD over the full detector range for each individual bead is required, as it avoids errors caused by bead size variations and instrument drift. The PSD signal is then converted to a displacement value, see Figure 7.5. Bead displacement from the trap center at the point of rupture is converted to a force in the direction of pulling, based on the measured trap stiffness, determined separately. The true force component along the direction of the tether is slightly greater than the measured force, owing to the changing angle between the tether and the plane of the coverglass.

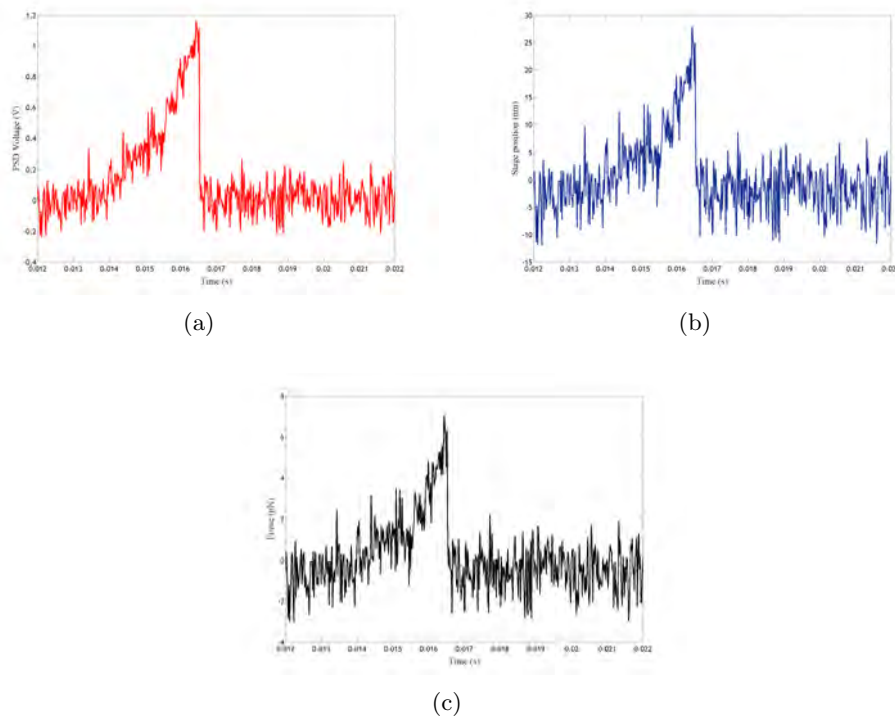


**Figure 7.5** Trace of the force exerted on the 4-4-20/fluorescein complex. The system is loaded at a constant pulling rate of 100 nm/s, until the mechanical break occurs at  $\sim 6$  pN. The event is detected by the PSD (a) which is calibrated to convert the PSD signal to position (b). Stiffness calibration allows converting position to applied force (c).

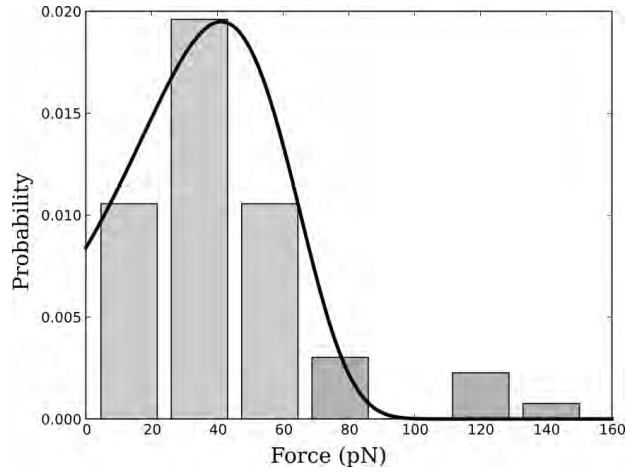


**Figure 7.6** Experimental rupture force probability distribution for the 4-4-20/fluorescein complex, measured with a loading rate of 43.00 pN/s ( $\pm 6.52$  pN/s). The rupture force for this pulling rate is 41.2 pN. The fit to Equation 7.1 leads  $k_{off} = 0.33$  s $^{-1}$  and  $x = 0.16$  nm.

From the force-time traces (Figure 7.5(c)) the rupture force is extracted. A set of 62 rupture events was recorded with a constant loading rate of 43.00 pN/s ( $\pm 6.52$  pN/s). The variability of the loading rate is due to the variable trap stiffness, as previously discussed. By plotting the histogram of the rupture force probability  $p(F)$  (Figure 7.6) and fitting to the distribution of Equation 7.1 the values of the thermal off-rate  $k_{off}$  in absence of load and the distance  $x$  to the transition state along the reaction coordinate are extracted. We find  $k_{off} = 0.33$  s $^{-1}$  and  $x = 0.16$  nm.

## 7.5 Conclusions

A model system was used for developing an optical tweezers-based antibody-antigen binding interaction assay. The binding interaction between the antigen fluorescein and its murine monoclonal antibody, clone 4-4-20, was probed using a tethered bead assay. Fluorescein-conjugated, 1010 bp DNA tethers were obtained with PCR. The tethers were attached to 500 nm polystyrene beads using a biotin-avidin linkage. The bond breakage force was then measured at a constant loading rate, to obtain a rupture force probability distribution. This was fitted to the theoretical distribution in the single energy-barrier formalism to give the thermal off-rate in absence of load. By performing the rupture force measurements for a set of loading rates, it will be possible to extract the natural thermal off-rate. To further develop the assay and achieve simultaneous single-molecule fluorescence measurement, a different dye should be considered, as fluorescein is not well suited for single-molecule detection.

## Bibliography

- [1] E.L. Florin, V.T. Moy, and H.E. Gaub. Adhesion forces between individual ligand-receptor pairs. *Science*, 264:415–417, 1994.
- [2] T. Nishizaka, H. Miyata, H. Yoshikawa, and K. Kinosita. Unbinding force of a single motor molecule of muscle measured using optical tweezers. *Nature*, 377:251–254, 1995.
- [3] C. Bustamante, J.C Macosko, and J.L. Wuite. Grabbing the cat by the tail: manipulating molecules one by one. *Nature Reviews*, 1:130–136, 2000.
- [4] E. Evans and K. Ritchie. Dynamic strength of molecular adhesion bonds. *Biophys. J.*, 72:1541–1555, 1997.
- [5] C. Friedsam, A.K. Wehle, F. Kuhner, and H.E. Gaub. Dynamic single-molecule force spectroscopy: bond rupture analysis with variable spacer length. *J. Phys.: Condens. Matter*, 15:S1709, 2003.
- [6] M.J. Lang, P.M. Fordyce, A.M. Engh, K.C., and S.M. Block. Simultaneous, coincident optical trapping and single molecule fluorescence. *Nature Methods*, 1:1–7, 2004.
- [7] J.W. Shaevitz, E.A. Abbondanzieri, R. Landick and S.M. Block. Backtracking by single RNA polymerase molecules observed at near-base-pair resolution. *Nature*, 426:684–687, 2003.
- [8] G.J. Wuite, S.B. Smith, M. Young, D. Keller and C. Bustamante. Single-molecule studies of the effect of template tension on T7 DNA polymerase activity. *Nature*, 404:103106, 2000.

- [9] J. Happel and H. Brenner. *Low Reynolds number hydrodynamics, 2nd ed.* Dordrecht, The Netherlands: Kluwer Academic, 1991.
- [10] K.C. Neuman and S.M. Block. Optical trapping. *Rev. Sci. Instr.*, 75:2787–2809, 2004.
- [11] C. Deufel and M.D. Wang . Detection of forces and displacements along the axial direction in an optical trap. *Biophys. J.*, 90:657–667, 2006.
- [12] S. Sato, M. Ohyumi, H. Shibata and H. Inaba. Optical trapping of small particles using a 1.3-micrometer compact In-GaAs diode laser. *Opt. Lett.*, 16:282–284, 1991.
- [13] A. Ashkin. Forces of a single-beam gradient laser trap on a dielectric sphere in the ray optics regime. *Biophys. J.*, 61:569–582, 1992.
- [14] D.M. Kranz, J.N. Herron, and E.W. Voss. Mechanism of ligand binding by monoclonal anti-fluorescyl antibodies. *J. Biol. Chem.*, 257:6987–6995, 1982.
- [15] E.T. Boder, K.S. Midelfort, and K.D. Wittrup. Directed evolution of antibody fragments with monovalent femtomolar antigen-binding affinity. *Proc. Nat. Acad. Sci.*, 97:10701–10705, 2000.
- [16] R. Ros, F. Schwesinger, D. Anselmetti, M. Kubon, R. Schafer, A. Plückthun and L. Tiefenauer. Antigen binding forces of individually addressed single-chain Fv antibody molecules. *Proc. Nat. Acad. Sci.*, 95:7402–7405, 1998.
- [17] F. Schwesinger, R. Ros, T. Strunz, D. Anselmetti, H.J. Gunterodt, A. Honegger, L. Jermutus, L. Tiefenauer and A. Plückthun. Unbinding forces of single antibody-antigen complexes correlate with their thermal dissociation rates. *Proc. Nat. Acad. Sci.*, 97:9972, 2000.
- [18] K. Neuman, E. Abbondanzieri, R. Landick, J. Gelles, S. Block. Ubiquitous transcriptional pausing is independent of RNA polymerase backtracking. *Cell*, 115:437–447, 2003.



## Chapter 8

# Conclusions

In this thesis, a setup was presented which combines optical tweezers, specifically designed to trap and micromanipulate individual microbubbles, with ultra-high speed imaging at nanoseconds timescale. The setup allowed to study for the first time the dynamics in ultrasound of the very same microbubble under well-controlled conditions, i.e. near or away from a neighboring wall or in the presence of a second trapped bubble. Microbubble phenomena are interesting from a fundamental physical standpoint, and a deeper understanding of their dynamics will also find direct applications in diagnostic imaging, as coated microbubbles are used in ultrasound medical imaging as contrast enhancer.

The first part of this work focused on the development of an optical tweezers setup for microbubbles manipulation. Since bubbles exhibit a lower refractive index than the medium, they are repelled by conventional optical traps. Laser beam shaping techniques were applied, where diffractive optical elements are used for converting a Gaussian laser beam to a Laguerre-Gaussian mode, as to obtain an optical trap with a dark core where microbubbles can be confined. Furthermore, full flexibility of the trapping configuration was obtained. Diffractive optical elements allow for the generation of multiple traps for microbubbles, and the implementation of the optical elements on a spatial light modulator enables to change the position, size and number of traps almost in real-time.

The second part of the work was aimed at combining the optical tweezers setup with a ultra-high speed camera, which enables time-resolved optical characterization of the microbubble dynamics in ultrasound, which occurs at MHz frequencies.

Finally, several experiments performed by controlling the position of microbubbles relative to interfaces or neighboring bubbles, proved the combined micromanipulation and imaging technique to be very powerful for unraveling the physical mechanisms underlying microbubble dynamics. The first experiments showed how the oscillations in ultrasound of one and the same bubble are influenced by the vicinity of a rigid wall or of a second bubble. Particularly, changes in the response of a bubble close to or away from a wall were studied, as changes in the acoustic signature may provide new diagnostic opportunities. A resonance frequency curve was recorded for the same bubble positioned at the wall and at

controlled distance from the wall. The experiments show a drop in the resonance frequency for the bubble close to the wall, as expected from a theoretical model based on a Rayleigh-Plesset-like equation and the so-called “method of images”. Nevertheless, a deeper insight is needed in the viscous boundary layer effects at the wall to fully describe the changes in bubble behavior.

We also quantified the bubble-to-bubble interaction, by comparing the change of the radial oscillations of one bubble with and without a neighboring bubble, and by resolving the change in distance between two bubbles during ultrasonic insonation. This results from an acoustical interaction force between the bubbles, termed secondary Bjerknes force. We compared the experimental results with the predictions of a model quantifying the mutual interaction of bubbles in their translation and oscillations, combined with a recent single-bubble model accounting for the shell properties. The agreement is very good but the model will be refined for a direct, quantitative comparison, to give an estimate of the secondary Bjerknes force and of the importance of small-Reynolds number effects.

Experiments where optical tweezers were used as a force sensor to measure ligand-receptor interactions at the single molecule level are also presented. A model system (fluorescein-anti fluorescein) was studied to develop a force spectroscopy assay on antigen-antibody complexes. Antibodies against different molecules can be produced and engineered, and used for specific targeting. The characterization of antigen-antibody interactions is therefore crucial for targeted molecular imaging applications.

## Outlook

A new class of contrast microbubbles is being developed, which are functionalized to adhere to specific markers of disease in the human body. If adherent microbubbles can be acoustically discriminated from freely flowing ones, new ultrasound imaging protocols can be developed to provide disease-specific contrast enhancement. Besides targeted molecular imaging applications, these microbubbles are also generally recognized to have a great potential for drug and gene delivery. Optical tweezers provide also in this case the necessary control of bubble position to perform precise characterization of bubble phenomena.

The perspective of combining optical micromanipulation with the force-sensing capabilities of optical tweezers presented in Chapter 7 is also particularly appealing. A position detection-based force measurement strategy, similar to the well-established ones for high-index particles, will give us detailed insight in the force balance acting on microbubbles in a shear flow within blood vessels, during insonation with ultrasound. A quantitative understanding of the balance between ultrasound radiation pressure and the viscous drag force, the latter one being dependent on the distance of the bubble from the vessel wall, together with a quantitative characterization of the binding interaction between targeted bubbles and target cells (see Figure 8.1), is crucial for optimizing ultrasound-assisted targeting strategies.

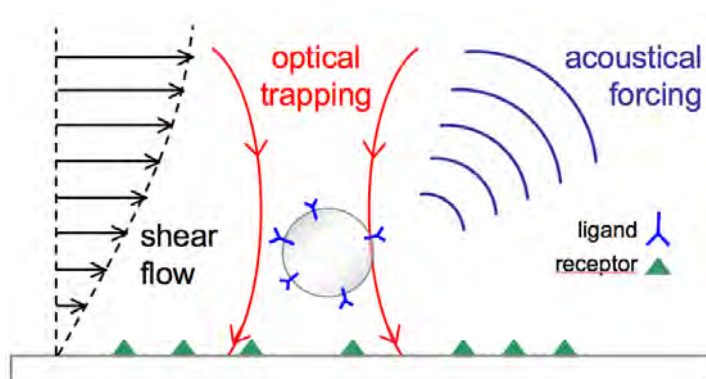


**Figure 8.1** A medical microbubble, functionalized with ligands for binding to specific cell receptors, experiences a drag force due to the viscous shear flow; the applied ultrasound wave causes an acoustic radiation force to push the bubble in the direction of propagation of the wave; optical tweezers can be used to elucidate the forces balance between fluid dynamical and acoustical forces, and how these affect the ligand-receptor interaction in bubble-cell adhesion. The efficiency of binding can be studied to a single-microbubble level by measuring the adhesion force with optical tweezers.



## Appendix A

# Interaction of the electromagnetic field with objects

The laws of conservation of energy and momentum for the electromagnetic field will be shortly recalled here, following the derivation given by Jackson [1].

The conservation of energy is stated in the Poynting's theorem. Consider a continuous distribution of charge and current. For a single charge  $q$  the rate of doing work by external electromagnetic fields  $\mathbf{E}$  and  $\mathbf{B}$  is  $q\mathbf{v} \cdot \mathbf{E}$  where  $\mathbf{v}$  is the velocity of the charge. The magnetic field does no work since the magnetic force is perpendicular to the velocity. The total rate of doing work by the fields in a arbitrary, finite volume  $V$  is

$$\int_V \mathbf{J} \cdot \mathbf{E} d^3x \quad (\text{A.1})$$

This power represents a conversion of electromagnetic energy into mechanical or thermal energy. It must be balanced by a corresponding decrease of energy in the electromagnetic field within the volume  $V$ . To exhibit this conservation law explicitly, Maxwell equations can be used to express A.1 in other terms. By substituting the Ampère-Maxwell law for  $\mathbf{J}$ :

$$\int_V \mathbf{J} \cdot \mathbf{E} d^3x = \int_V \left[ \mathbf{E} \cdot (\nabla \times \mathbf{H}) - \mathbf{E} \cdot \frac{\partial \mathbf{D}}{\partial t} \right] d^3x \quad (\text{A.2})$$

By rearranging using vector identities and Faraday's law:

$$\int_V \mathbf{J} \cdot \mathbf{E} d^3x = - \int_V \left[ \nabla \cdot (\mathbf{E} \times \mathbf{H}) + \mathbf{E} \cdot \frac{\partial \mathbf{D}}{\partial t} + \mathbf{H} \cdot \frac{\partial \mathbf{B}}{\partial t} \right] d^3x \quad (\text{A.3})$$

Assuming that the medium is linear in its magnetic and electric properties, with negligible dispersion or losses, and being the total electromagnetic energy density represented by

$$u = \frac{1}{2}(\mathbf{E} \cdot \mathbf{D} + \mathbf{B} \cdot \mathbf{H}) \quad (\text{A.4})$$

A.3 can be written

$$-\int_V \mathbf{J} \cdot \mathbf{E} d^3x = \int_V \left[ \frac{\partial u}{\partial t} + \nabla \cdot (\mathbf{E} \times \mathbf{H}) \right] d^3x \quad (\text{A.5})$$

Since the volume  $V$  is arbitrary, this can be cast into the form of a differential continuity equation or conservation law,

$$\frac{\partial u}{\partial t} + \nabla \cdot \mathbf{S} = -\mathbf{J} \cdot \mathbf{E} \quad (\text{A.6})$$

where  $\mathbf{S} = \mathbf{E} \times \mathbf{H}$  is the *Poynting vector*, representing the energy flow. The physical meaning of A.6 is that the time rate of change of electromagnetic energy within a certain volume, plus the energy flowing out through the boundary surfaces of the volume per unit time, is equal to the negative of the total work done by the fields on the sources within the volume. The work done per unit time per unit volume by the fields ( $\mathbf{J} \cdot \mathbf{E}$ ) is a conversion of electromagnetic energy into mechanical or heat energy. If we denote the total energy of the particles within the volume  $V$  as  $E_{mech}$  and assume that no particles move out of the volume, we have

$$\frac{dE_{mech}}{dt} = \int_V \mathbf{J} \cdot \mathbf{E} d^3x \quad (\text{A.7})$$

The Poynting's theorem expresses the conservation of energy for the combined system as

$$\frac{dE}{dt} = \frac{d}{dt}(E_{mech} + E_{field}) = -\oint_S \mathbf{n} \cdot \mathbf{S} da \quad (\text{A.8})$$

where the total field energy within  $V$  is

$$E_{field} = \int_V u d^3x = \frac{\epsilon_0}{2} \int_V (\mathbf{E}^2 + c^2 \mathbf{B}^2) d^3x \quad (\text{A.9})$$

The conservation of linear momentum can be similarly considered. The total electromagnetic force on a charged particle is

$$\mathbf{F} = q(\mathbf{E} + \mathbf{v} \times \mathbf{B}) \quad (\text{A.10})$$

If the sum of all the momenta of all the particles in the volume  $V$  is denoted by  $\mathbf{P}_{mech}$  we can write, from Newton's second law,

$$\frac{d\mathbf{P}_{mech}}{dt} = \int_V ((\rho \mathbf{E} + \mathbf{J} \times \mathbf{B})) \quad (\text{A.11})$$

where the sum over particle is converted into an integral over charge and current densities. We then can use again the Maxwell equations to eliminate  $\rho$  and  $\mathbf{J}$

from A.11 and get the rate of change of mechanical momentum

$$\begin{aligned} \frac{d\mathbf{P}_{\text{mech}}}{dt} + \frac{d}{dt} \int_V \epsilon_0 (\mathbf{E} \times \mathbf{B}) d^3x &= \\ &= \epsilon_0 \int_V \left[ \mathbf{E}(\nabla \cdot \mathbf{E}) - \mathbf{E} \times (\nabla \times \mathbf{E}) + c^2 \mathbf{B} \times (\nabla \times \mathbf{B}) \right] d^3x \end{aligned} \quad (\text{A.12})$$

By identifying the volume integral on the left as the total electromagnetic momentum  $\mathbf{P}_{\text{field}}$  in the volume  $V$ :

$$\mathbf{P}_{\text{field}} = \epsilon_0 \int_V \mathbf{E} \times \mathbf{B} d^3x = \mu_0 \epsilon_0 \int_V \mathbf{E} \times \mathbf{H} d^3x \quad (\text{A.13})$$

the integrand can be interpreted as a density of electromagnetic momentum. This momentum density is proportional to the energy-flux density  $\mathbf{S}$ , with proportionality constant  $c^{-2}$ . To complete the identification of the volume integral of

$$\mathbf{g} = \frac{1}{c^2} (\mathbf{E} \times \mathbf{H}) \quad (\text{A.14})$$

as electromagnetic momentum, and to establish A.12 as the conservation law for momentum, we must convert the volume integral on the right into a momentum flow. Let the Cartesian coordinates be denoted by  $x_\alpha$ ,  $\alpha = 1, 2, 3$ . With the definition of the *Maxwell stress tensor*  $T_{\alpha\beta}$  as

$$T_{\alpha\beta} = \epsilon_0 [E_\alpha E_\beta + c^2 B_\alpha B_\beta - \frac{1}{2} (\mathbf{E} \cdot \mathbf{E} + c^2 \mathbf{B} \cdot \mathbf{B}) \delta_{\alpha\beta}] \quad (\text{A.15})$$

we can therefore write A.12 in component form as

$$\frac{d}{dt} (\mathbf{P}_{\text{mech}} + \mathbf{P}_{\text{field}})_\alpha = \sum_\beta \int_V \frac{\partial}{\partial x_\beta} T_{\alpha\beta} d^3x \quad (\text{A.16})$$

Application of the divergence theorem to the volume integral gives

$$\frac{d}{dt} (\mathbf{P}_{\text{mech}} + \mathbf{P}_{\text{field}})_\alpha = \oint_S \sum_\beta T_{\alpha\beta} n_\beta da \quad (\text{A.17})$$

where  $\mathbf{n}$  is the outward normal to the closed surface  $S$ . If A.17 states the conservation of momentum,  $\sum_\beta T_{\alpha\beta} n_\beta$  is the  $\alpha$ th component of the flow per unit area of momentum across the surface  $S$  into the volume  $V$ , i.e. the force per unit area transmitted across the surface  $S$  and acting on the system of particles and fields inside  $V$ . Equation A.17 can therefore be used to calculate the forces acting on material objects in electromagnetic fields by enclosing the objects with a boundary surface  $S$  and adding up the total electromagnetic force according to the right-hand side of A.17.

## Bibliography

- [1] J.D. Jackson. *Classical Electrodynamics*, pages 258–264. 3rd ed., Wiley, 1999.



# List of Figures

1.1	Medical microbubble adherent to target cells . . . . .	2
2.1	First gradient force optical trap . . . . .	8
2.2	Working principle of Optical Tweezers . . . . .	10
2.3	Multiple optical tweezers . . . . .	11
2.4	Ray-optics model for optical trapping . . . . .	15
2.5	Optical trap potential well . . . . .	17
3.1	Encoding phase in thickness or refractive index modulation . . . . .	25
3.2	DOE calculated with PRIA . . . . .	28
3.3	DOEs calculated with the spherical waves propagation approach . . . . .	30
3.4	Phase of a helical beam . . . . .	31
3.5	Intensity profile of a Laguerre-Gaussian beam . . . . .	32
3.6	DOEs for generating LG beams . . . . .	33
3.7	Focused Laguerre-Gaussian beams. . . . .	33
3.8	Helical beam converter . . . . .	34
3.9	Singular beam obtained with a holographic optical element . . . . .	34
3.10	DOE for generating multiple LG beams . . . . .	35
3.11	Two LG traps with tunable distance . . . . .	35
3.12	Minimum number of pixels encoding for a phase singularity . . . . .	36
3.13	Generating an array of $3 \times 3$ donut traps . . . . .	36
3.14	3D position of a vortex trap: DOE . . . . .	37
3.15	3D position of a vortex trap: output pattern . . . . .	38
4.1	Optical setup for 3D manipulation of microbubbles . . . . .	44
4.2	3D trapping of an individual, $3 \mu\text{m}$ microbubble . . . . .	47
4.3	Sequence of DOEs for sorting microbubbles . . . . .	48
4.4	2D trapping of multiple microbubbles . . . . .	48
4.5	Two microbubbles trapping and manipulation: beam shaping . . . . .	49
4.6	Two microbubbles trapping and manipulation in 3D . . . . .	50
4.7	Bubble pairs trapped in 3D . . . . .	50
5.1	Optical setup for microbubble trapping and ultra-high speed imaging . . . . .	56
5.2	The “Brandaris 128” ultra-high speed camera . . . . .	57
5.3	Brandaris and optical tweezers . . . . .	58

5.4	Controlling the divergence of the trapping laser (schematic) . . . . .	59
5.5	Controlling the divergence of the trapping laser (plot) . . . . .	59
5.6	Image plane position . . . . .	60
5.7	Freely oscillating microbubble recorded at 15 Mfps . . . . .	62
5.8	$R - t$ curve of a freely oscillating microbubble recorded at 15 Mfps	63
5.9	Influence of the laser trap on bubble dynamics . . . . .	64
6.1	Ultrasound diagnostic imaging with UCA microbubbles . . . . .	68
6.2	Resonance frequency shift for a bubble close to a wall: theory . . . . .	73
6.3	Single bubble dynamics as a function of the distance from a wall . . . . .	78
6.4	Amplitude of oscillations for a bubble pair . . . . .	80
6.5	Resonance frequency shift of a single bubble near a wall . . . . .	82
6.6	Resonance frequency shift of a single bubble near a second bubble	83
6.7	Secondary Bjerknes force between two bubbles . . . . .	84
6.8	Numerical simulation for secondary Bjerknes force . . . . .	85
7.1	Back-focal plane detection. . . . .	94
7.2	Optical layout of the instrument combining optical trapping and single molecule fluorescence . . . . .	97
7.3	Gel electrophoresis for 1010 bp DNA . . . . .	98
7.4	Instrument combining optical trapping and single molecule fluo- rescence . . . . .	100
7.5	Rupture force trace . . . . .	101
7.6	Rupture force probability distribution . . . . .	102
8.1	Force measurements on microbubbles with optical tweezers . . . . .	107

# List of Tables

2.1	Overview of single molecule manipulation techniques. . . . .	13
3.1	Maximum theoretical efficiencies for different types of holograms. .	26
4.1	Buoyancy force and terminal rise velocity for UCA microbubbles in water . . . . .	46



# Abbreviations

DOE	diffractive optical element
SLM	spatial light modulator
LCD	liquid crystal display
LG	Laguerre-Gaussian
IR	infrared
CW	continuous wave
PRIA	phase retrieval iterative algorithm
NA	numerical aperture
UCA	ultrasound contrast agent
RP	Rayleigh-Plesset
MI	mechanical index
PNP	peak negative pressure
Mfps	million frames per second
FFT	fast Fourier transform
QPD	quadrant photodiode
PSD	position sensitive detector
BFP	back focal plane
PCR	polymerase chain reaction



# List of publications

## Journal papers

- V. Garbin, D. Cojoc, E. Ferrari, E. Di Fabrizio, M. Overvelde, S. van der Meer, N. de Jong, D. Lohse, M. Versluis, “Changes in microbubble dynamics near a boundary revealed by combined optical micromanipulation and high speed imaging”, accepted for publication in *Appl. Phys. Lett.*
- V. Garbin, D. Cojoc, E. Ferrari, R.Z. Proietti, S. Cabrini, E. Di Fabrizio, “Optical micro-manipulation using Laguerre-Gaussian beams”, *Japan. J. Appl. Phys.* **44**, 5773 (2005)
- V. Emiliani, D. Cojoc, E. Ferrari, V. Garbin, C. Durieux, M. Coppey-Moisan, E. Di Fabrizio, “Wave front engineering for microscopy of living cells”, *Opt. Exp.* **13**, 1395 (2005)
- D. Cojoc, V. Garbin, E. Ferrari, L. Businaro, F. Romanato, E. Di Fabrizio, “Laser trapping and micro-manipulation using optical vortices”, *Microel. Eng.* **78-79**, 575 (2005)
- E. Ferrari, V. Emiliani, D. Cojoc, V. Garbin, M. Zahid, C. Durieux, M. Coppey-Moisan, E. Di Fabrizio, “Biological samples micro-manipulation by means of optical tweezers”, *Microel. Eng.* **78-79**, 125 (2005)
- E. Di Fabrizio, D. Cojoc, V. Emiliani, S. Cabrini, M. Coppey-Moisan, E. Ferrari, V. Garbin, M. Altissimo, “Microscopy of Biological Samples Through Advanced Diffractive Optics From Visible to X-Ray Wavelength Regime”, *Micr. Res. Techn.* **65**, 252 (2004)
- L. Bruschi, G. Fois, and G. Mistura, M. Tormen, V. Garbin, E. Di Fabrizio, A. Gerardino, M. Natali, “Complete wetting of curved microscopic channels”, *J. Chem. Phys.* **125**, 144709 (2006)

## Awards

- Best Technical Poster Prize, 12<sup>th</sup> *European Symposium on Ultrasound Contrast Imaging*, Rotterdam, The Netherlands (2007)
- Best Student Prize, *NanoItaly - 3<sup>rd</sup> National Conference on Nanoscience and Nanotechnology*, Trieste, Italy (2006)

## Conference Proceedings

- V. Garbin, E. Ferrari, D. Cojoc, E. Di Fabrizio, M. Overvelde, M. Versluis, S.M. van der Meer, N. de Jong, D. Lohse, “Optical trapping of ultrasound contrast agent microbubbles. Study of the bubble-wall and bubble-bubble interaction in ultrasound”, 2006 IEEE International Ultrasonics Symposium (in press)
- V. Garbin, D. Cojoc, E. Ferrari, E. Di Fabrizio, M. Overvelde, M. Versluis, S. van der Meer, N. de Jong, D. Lohse, “Time-resolved nanoseconds dynamics of ultrasound contrast agent microbubbles manipulated and controlled by optical tweezers”, *Proceedings SPIE* **6326** (in press)
- D. Cojoc, H. Amenitsch, C. Riekkel, E. Ferrari, M. Rappolt, V. Garbin, B. Sartori, M. Burghammer, E. Di Fabrizio, “Combined laser trapping and small-angle x-ray scattering experiment for the study of liposome colloidal microparticles”, *Proceedings SPIE* **6326** (in press)
- A. Moradi, E. Ferrari, V. Garbin, E. Di Fabrizio, D. Cojoc, “Trapping force gradient using diffractive optical elements”, *Proceedings SPIE* **6326** (in press)
- V. Emiliani, D. Cojoc, E. Ferrari, V. Garbin, C. Durieux, E. Di Fabrizio, “Wavefront engineering microscopy to study 3D mechanotransduction in living cells”, *Proceedings SPIE* **6195**, 127 (2006)
- K.S. Mohanty, C. Liberale, S.K. Mohanty, V. Degiorgio, S. Cabrini, A. Carpentiero, V. Garbin, M. Prasciolu, D. Cojoc, E. Di Fabrizio, “Fiber optic trapping of low-refractive index particles”, *Proceedings SPIE* **6088**, 306 (2006)
- D. Cojoc, E. Ferrari, V. Garbin, S. Cabrini, A. Carpentiero, M. Prasciolu, L. Businaro, B. Kaulich, E. Di Fabrizio, “Wave front engineering by means of diffractive optical elements for applications in microscopy”, *Proceedings SPIE* **6254**, 320 (2006)
- V. Garbin, D. Cojoc, E. Ferrari, R. Kulkarni, E. Di Fabrizio, “Manipulation of single and multiple low-index particles by means of optical tweezers”, *Proceedings SPIE* **5930**, 492 (2005)



- V. Garbin, D. Cojoc, R. Kulkarni, R. Malureanu, E. Ferrari, M. Nadasan, E. Di Fabrizio, “Numerical analysis of forces in optical tweezers in the Rayleigh regime”, *Proceedings SPIE* **5972**, 30 (2005)
- D. Cojoc, E. Ferrari, V. Garbin, E. Di Fabrizio, “Multiple optical tweezers for micro Raman spectroscopy”, *Proceedings SPIE* **5930**, 64 (2005)

## Conference abstracts

- V. Garbin, M. Overvelde, B. Dollet, D. Cojoc, E. di Fabrizio, N. de Jong, M. Versluis, D. Lohse, “A study of bubble-bubble interactions controlled by optical micromanipulation”, *ESF Conference - Trends in Optical Micromanipulation*, Obergurgl, Austria (2007)
- M.L.J. Overvelde, V. Garbin, B. Dollet, S.M. van der Meer, M. Versluis, D. Cojoc, E. Ferrari, N. de Jong, E. Di Fabrizio, and D. Lohse, “3D optical micromanipulation of ultrasound contrast agents: bubble-wall interactions”, *ESF Conference - Trends in Optical Micromanipulation*, Obergurgl, Austria (2007)
- M.L.J. Overvelde, V. Garbin, B. Dollet, D. Cojoc, E. Ferrari, N. de Jong, E. Di Fabrizio, D. Lohse, and M. Versluis, “3D optical micromanipulation of ultrasound contrast agents: bubble-bubble and bubble-wall interactions”, *12<sup>th</sup> European Symposium on Ultrasound Contrast Imaging*, Rotterdam, The Netherlands (2007)
- B. Dollet, S. van der Meer, M. Overvelde, V. Garbin, N. de Jong, M. Versluis, D. Lohse, “Microbubble spectroscopy of ultrasound contrast agents: influence of the shell and of a confining wall”, *12<sup>th</sup> European Symposium on Ultrasound Contrast Imaging*, Rotterdam, The Netherlands (2007)
- V. Garbin, D. Cojoc, E. Ferrari, E. Di Fabrizio, M. Overvelde, S. van der Meer, N. de Jong, D. Lohse, M. Versluis, “Laser Tweezers for manipulation and control of ultrasound contrast agents”, *11<sup>th</sup> European Symposium on Ultrasound Contrast Imaging*, Rotterdam, The Netherlands (2006)
- V. Garbin, D. Cojoc, E. Ferrari, E. Di Fabrizio, M. Overvelde, M. Versluis, S. van der Meer, N. de Jong, D. Lohse, “Laser Tweezers for 3D control of ultrasound contrast agent microbubbles during high-speed optical observations”, *3<sup>rd</sup> National Conference on Nanoscience and Nanotechnology*, Trieste, Italy (2006)
- D. Cojoc, V. Garbin, E. Ferrari, E. Di Fabrizio, “Laser trapping of high- and low- index particles using optical vortices”, *OWLS VIII*, Melbourne, Australia (2004)
- E. Ferrari, V. Emiliani, D. Cojoc, V. Garbin, M. Zahid, C. Durieux, M. Coppey, E. Di Fabrizio, “2D and 3D multi-trap optical tweezers to mimic

the mechanical environment of living cells”, *OWLS VIII*, Melbourne, Australia (2004)

# Acknowledgments

I wish to express my sincere thanks to my thesis adviser Prof. Enzo Di Fabrizio for giving me unique opportunities throughout my PhD. Very many thanks to the persons I worked in closest contact with: Dr. Dan Cojoc, for his daily supervision and for the enthusiasm and efforts he put in this investigation, and my colleague Enrico Ferrari, with whom I shared the highs and lows of life as a PhD student. I would also like to thank all the group members at LILIT for their support and cooperation.

I thank Dr. Marcel Arditi and Dr. Peter Frinking of Bracco Research S.A. for initiating this work and for their valuable comments, and Dr. Marco Mattiuzzi of Bracco Imaging.

I would like to thank Prof. Detlef Lohse at the University of Twente, and his entire group, particularly Dr. Michel Versluis, Dr. Benjamin Dollet, Marlies Overvelde, Sander van der Meer and Jeroen Sijl, for the very fruitful collaboration. I also thank Prof. Nico de Jong from the Erasmus Medical Center for helpful discussions.

Many thanks to Prof. Matthew J. Lang at MIT for having me as a visiting student in his group, and to the lab members, who helped me getting so many things done in such a short time. I would like to thank Dr. Lorella Pascolo from the University of Trieste for her exciting ideas and for her guidance into the fascinating world of Biochemistry.

Finally, I would like to thank my parents for having always helped me doing what I really want to do.



# Curriculum vitae

Valeria Garbin was born on May 2, 1979, in Venezia, Italy. In 1998 she started her study at the University of Padova (Italy), faculty of Mathematical, Physical and Natural Sciences. She obtained her *Laurea* degree in Physics in 2003. The subject of her thesis was ‘Wetting of curved microscopic channels’, developed under the supervision of Prof. Giampaolo Mistura at the University of Padova and Dr. Massimo Tormen at the TASC National Laboratory of CNR-INFN in Trieste (Italy).

In 2004 she started a PhD in ‘Nanotechnology for biomedical applications’ at the University of Trieste under the supervision of Prof. Enzo Di Fabrizio. Her research focused on the use of optical tweezers for studying microbubble dynamics in ultrasound, with applications to targeted molecular imaging. The project was carried out at the TASC National Laboratory in collaboration with the group of Physics of Fluids at the University of Twente (The Netherlands).

In 2005 Valeria Garbin visited the group of Prof. Matthew J. Lang at MIT for a 4-month research stay on force spectroscopy using optical tweezers.

She can be contacted at [valeria.garbin@gmail.com](mailto:valeria.garbin@gmail.com).

